



HAL
open science

Formation of graphene on liquid copper: In situ synchrotron X-ray study

Francesco La Porta

► **To cite this version:**

Francesco La Porta. Formation of graphene on liquid copper: In situ synchrotron X-ray study. Materials Science [cond-mat.mtrl-sci]. Université Grenoble Alpes [2020-..], 2021. English. NNT: 2021GRALY011 . tel-03428986

HAL Id: tel-03428986

<https://theses.hal.science/tel-03428986>

Submitted on 15 Nov 2021

HAL is a multi-disciplinary open access archive for the deposit and dissemination of scientific research documents, whether they are published or not. The documents may come from teaching and research institutions in France or abroad, or from public or private research centers.

L'archive ouverte pluridisciplinaire **HAL**, est destinée au dépôt et à la diffusion de documents scientifiques de niveau recherche, publiés ou non, émanant des établissements d'enseignement et de recherche français ou étrangers, des laboratoires publics ou privés.

THÈSE

Pour obtenir le grade de

DOCTEUR DE L'UNIVERSITÉ GRENOBLE ALPES

Spécialité : **Physique de la Matière Condensée et du Rayonnement**

Arrêté ministériel : 25 mai 2016

Présentée par

Francesco LA PORTA

Thèse dirigée par **Gilles RENAUD**, Université Grenoble Alpes
et codirigée par **Oleg KONOVALOV**

préparée au sein du **Laboratoire European Synchrotron
Radiation Facility**
dans l'**École Doctorale Physique**

**Croissance de graphène sur cuivre liquide :
études in situ par rayons X synchrotron**

**Formation of graphene on liquid copper: In
situ synchrotron X-ray study**

Thèse soutenue publiquement le **18 mars 2021**,

Monsieur Jean-Yves VEUILLEN

DIRECTEUR DE RECHERCHE, Institut Néel, Président

Monsieur Roberto FELICI

DIRECTEUR DE RECHERCHE, Consiglio Nazionale delle Ricerche,
Rapporteur

Monsieur Alain GIBAUD

PROFESSEUR, Université du Mans, Rapporteur

Madame Bridget MURPHY

PROFESSEUR ASSOCIE, University of Kiel, Examinatrice

Monsieur Johann CORAUX

CHARGE DE RECHERCHE, Institut Néel, Examineur

Monsieur Michel GOLDMANN

PROFESSEUR, Université de Paris, Examineur



Acknowledgements

My deepest gratitude goes to my thesis directors Oleg Konovalov, Gilles Renaud, and Maciej Jankowski, for guiding me during this experience. All three have incredible knowledge that they share with generosity and enthusiasm. They taught me an incredible amount of things that go beyond the scientific subjects. I also want to thank the members of the jury for the scientific discussion during the PhD defense.

I want to express my gratitude to all members of the LMCat consortium. In particular, I would like to thank Irene Grooth for dealing with the organization of the project and for the nice scientific discussions during the weekly meetings. I want to thank my colleague and friend Amirmehdi Saedi for the nice time and the smart and pleasant talks we had during these years. Furthermore, I would like to thank Costas Galiotis, Anastasios Manikas, and Christos Tsakonas for their availability to help with the Raman set-up or during the beamtimes, and for the nice time spent after work. Furthermore, I am grateful for the help of Gertjan van Baarle and Marc de Voogd for solving the issues related to the reactor. I would also thank Karsten Reuter, Mie Andersen, and Santiago Cingolani for the theoretical support and for the debates on the nature of the flakes interaction. A particular thanks also to Valentina Belova, for the useful advice and corrections to this manuscript. I also would like to express my gratitude to Kamil Filipczak and Sebastian Fava for their work in the laboratory and for the nice time spent together. Special thanks to the members of ID03 beamline in ESRF, P08 beamline at DESY, I07 beamline in DIAMOND, and SIRIUS and SIXS beamline in SOLEIL for their constant help and precious advice during the experiments. I would like to thank all my friends in Savigliano and Torino for making me feel welcome every time I came back, and for the nice experiences we had. I am also grateful for all the people and friends I met in these three years in Grenoble; this work would have been impossible for me without the nice times, the useful tips, and the great experiences I had with them. In particular, I want to thank Andrea Vera Loor for always being with me and for supporting me.

I owe my deepest gratitude to my father Diego La Porta, and my mother Marilena Curti, for their sacrifices for making me studying and for always believing in me. Furthermore, I would like to thank my sister Cristina, my grandparents, and all my family for the love they freely give to me.

Abstract

Graphene was isolated in 2004, and in a few years astonished the scientific community. Its peculiar physical properties of electric conductivity, mechanical strength and flexibility, and transparency are extremely interesting for many applications.

One of the main issues that hinder the entry of this material into the market is the large scale production route. A cheap method that guarantees a high-quality product is still missing. The graphene properties can be easily altered by defects, grain boundaries, and non uniformity number of layers. One of the most promising methods of synthesis is chemical vapor deposition (CVD), which consists of the dissociation of a gaseous precursor on a transition metal catalyst. The carbon adatoms then diffuse on the metal, and they aggregate to the graphene crystal structure. Once all the surface is covered by the graphene, the gas cannot reach the catalytic site anymore, and the reaction stops. The drawback of CVD is that the morphology of the metal surface influences the quality of the graphene produced. The graphene, as a matter of fact, nucleates on grain boundaries and defects of the surface of the metal. Many nucleation points result in a polycrystal material that has many grain boundaries. The ideal flat uniform defect-free surface morphology is very hard to achieve on solid metal.

The use of a liquid substrate instead of a solid one can overcome these issues. The liquid naturally has a uniform and atomically flat surface. The first papers on graphene on a liquid metal show great quality and high reproducibility of the reaction. Another interesting phenomenon that occurs on the surface of liquid metals is that the flakes can move and rotate, and they tend to aggregate and auto-align. The state of the art of CVD growth of graphene on liquid copper will be discussed in Chapter 1.

The experiments CVD growth of graphene on liquid metals in literature follow a similar approach: the metal is melted, the graphene is grown, and lastly, the sample was resolidified in order to do the characterization. This approach, however, alters the surface significantly. Furthermore, in this way, information on the dynamic of the growth was lost entirely. The work described in this thesis is situated in this scenario and has the main objective to fill this gap. A reactor, hence, was projected for the in-situ characterization with the simultaneous combination of x-ray scattering techniques and optical microscopy. The principle of the techniques is described in Chapter 2, while the reactor and the instrumentation are described in Chapter 3. The metal

chosen for the catalyst is liquid copper.

The optical microscope revealed to be an essential tool to understand the dynamics of the flake movement on the surface of the liquid and to have feedback on the status of the growth. This is described in Chapter 4. A graphene flake larger than 2 mm was produced. It was observed that the flakes of graphene could auto-align, and, with the help of the collaborators of the project, a mechanism was proposed.

The x-ray reflectivity (XRR) and the grazing incident x-ray diffraction (GIXD) were the two techniques applied at the synchrotron. The analysis of the data for the XRR was hampered by the convex shape of the surface. With a convex surface, in fact, the reflected beam spreads, and the incident angle depends partially on the curvature of the sample. In chapter 5, the effects of a bent surface are described, and a method for analyzing the data is presented.

In Chapter 6, the results of x-ray scattering measurements are exposed. Using GIXD, the lattice parameter of the graphene was measured for the first time on liquid copper. The XRR measurements proved that the distance between the graphene and the liquid copper atom was 1.40 Å and that the roughness of the graphene and the liquid were similar, at 1.24 Å.

Résumé

Le graphène a été synthétisé en 2004, le graphène en quelques années a étonné la communauté scientifique. Ses propriétés physiques particulières de transfert de charge électrique, sa résistance mécanique, sa flexibilité et sa transparence sont les ingrédients clés d'une révolution de la technologie moderne.

L'un des principaux problèmes qui entravent l'entrée de ce matériau sur le marché est la voie de production à grande échelle. Il manque encore une méthode bon marché garantissant un produit de haute qualité. Les propriétés du graphène peuvent être facilement modifiées par des défauts, des joints de grains et l'absence d'uniformité du nombre de couches. L'une des méthodes de synthèse les plus prometteuses est le chemical vapour deposition (CVD), qui consiste en la dissociation d'un précurseur gazeux sur un catalyseur de métal de transition. Les adatoms de carbone se diffusent alors sur le métal et s'agrègent à la structure cristalline du graphène. Une fois que toute la surface est recouverte par le graphène, le gaz ne peut plus atteindre le site catalytique et la réaction s'arrête. L'inconvénient du CVD est que la morphologie de la surface métallique influence la qualité du graphène produit. Le graphène, en effet, se nucléé sur les joints de grains et les défauts de la surface du métal. De nombreux points de nucléation donnent un matériau polycristal qui possède de nombreuses limites de grains. La morphologie de surface plane et uniforme idéale sans défaut est très difficile à obtenir sur du métal solide.

L'utilisation d'un substrat liquide au lieu d'un substrat solide peut surmonter ces problèmes. Le liquide a naturellement une surface uniforme et atomiquement plate. Les premiers papiers sur graphène sur métal liquide montrent une grande qualité et une grande reproductibilité de la réaction. Un autre phénomène intéressant qui se produit à la surface du métal liquide est que les flocons peuvent se déplacer et tourner, et ils ont tendance à s'agréger et à s'auto-aligner. L'état de l'art de la croissance CVD du graphène sur du cuivre liquide sera discuté au chapitre 1.

Les expériences de croissance CVD du graphène sur métal liquide dans la littérature suivent une approche similaire: le métal est fondu, le graphène est cultivé, et enfin, l'échantillon a été resolidifié afin de faire la caractérisation. Cette approche, cependant, modifie considérablement la surface. De plus, de cette manière, les informations sur la dynamique de la croissance ont été entièrement perdues. Le travail décrit dans cette thèse se situe dans ce

scénario et a pour principal objectif de combler cette lacune. Un réacteur a donc été projeté pour la caractérisation in-situ avec la combinaison simultanée de techniques de diffusion des rayons X et de microscopie optique. Le principe des techniques est décrit au chapitre 2, tandis que le réacteur et l'instrumentation sont décrits au chapitre 3. Le métal choisi pour le catalyseur est le cuivre liquide. Le microscope optique s'est révélé être un outil essentiel pour comprendre la dynamique du mouvement des flocons à la surface du liquide et pour avoir un retour sur l'état de la croissance. Ceci est décrit au chapitre 4. Un flocon de graphène de plus de 2 mm a été produit. Il a été observé que les paillettes de graphène pouvaient s'auto-aligner et, avec l'aide des collaborateurs du projet, un mécanisme a été proposé. Les mesures effectuées au synchrotron étaient la réflectivité des rayons X (XRR) et la diffraction des rayons X incidente rasante (GIXD). L'analyse des données pour le XRR a été entravée par la forme convexe de la surface. Avec une surface convexe, en effet, le faisceau réfléchi se propage, et l'angle incident dépend en partie de la courbure de l'échantillon. Au chapitre 5, les effets d'une surface pliée sont décrits et une méthode d'analyse des données est présentée. Au chapitre 6, les résultats des techniques de diffusion des rayons X sont exposés. Avec le GIXD, le paramètre de réseau du graphène a été mesuré pour la première fois sur du cuivre liquide. Les mesures XRR ont prouvé que la distance entre le graphène et l'atome de cuivre liquide était de 1,40 Å et que la rugosité du graphène et du liquide était similaire, à 1,24 Å.

Contents

Acknowledgements	i
Abstracts	ii
Résumé	iv
1 Introduction	1
1.1 Graphene	1
1.1.1 Atomic structure	1
1.1.2 Band structure	2
1.2 CVD methods for the graphene growth	3
1.2.1 Principles of the techniques	3
1.2.2 CVD on liquid metals	11
1.2.2.1 Introduction	11
1.2.2.2 Nucleation and growth on liquid copper	13
1.2.2.3 Etching behaviour	15
1.2.2.4 Self assembling	16
1.3 Liquid surface	17
1.3.1 Liquid roughness	17
1.3.2 Capillary interactions	18
2 Characterization techniques	22
2.1 X-ray diffraction	22
2.1.1 Interaction between matter and x-ray	22
2.1.2 Scattering from a 3D crystal	25
2.1.3 Surface x-ray diffraction	27
2.1.4 Scattering from a liquid	28
2.2 X-ray reflectivity	29

2.2.1	Snell's law and Fresnel reflectivity	31
2.2.2	Derivation of the density profile	32
2.3	The synchrotron radiation	34
2.3.1	The synchrotron	34
2.3.2	The beam production	36
2.4	Raman spectroscopy	37
2.4.1	The Raman effect	37
2.4.2	Raman on graphene	39
2.5	Radiation mode optical microscopy	41
3	Experimental setup	43
3.1	The LMCat project	43
3.2	LMCat equipments	44
3.2.1	The reactor & gas system	44
3.2.2	Sample & sample holder	47
3.2.3	Raman & Optical microscope	48
3.2.3.1	The Raman spectrometer	48
3.2.3.2	The optical microscope	50
3.3	Liquid surface diffractometer	51
3.3.1	General geometry of the liquid surface diffractometers .	51
3.3.2	ID10B beamline	52
3.3.3	Other surface diffraction beamlines	53
4	Growth of graphene on liquid copper	55
4.1	Introduction	55
4.2	Growth scenarios	58
4.2.1	Low nucleation density	58
4.2.2	Medium nucleation density & auto-alignment	62
4.2.3	High nucleation density	67
4.2.4	Real time control of the growth	67
4.3	Particles impurity	68
4.4	Assessing the quality of the graphene layer grown	73
4.5	Conclusion	75
5	Analysing XRR data from a bent surface with a 2D detector	76
5.1	Introduction	76
5.2	ROI integration	79
5.3	Principles of the signal reconstruction method	80

5.3.1	Associating a value of q_z to every pixel	81
5.3.2	Obtaining the reflectivity values in each pixel	84
5.3.3	Obtaining the radius of the sample from the reflection profile	86
5.3.4	Averaging the intensities of pixels in the same range of q_z and reconstructing the diffraction signal	88
5.3.5	Analyzing the reconstructed signal and obtaining the XRR curve	90
5.4	Simulating the experiment	90
5.5	Results and discussion	93
5.6	Conclusions	98
6	<i>In situ</i> X-ray study on LMCat	99
6.1	Introduction	99
6.2	Alignment of the x-ray beam on a convex surface	100
6.3	Grazing incident x-ray diffraction	101
6.4	X-ray reflectivity	105
6.5	Conclusion	111
7	Conclusions	112

Chapter 1

Introduction

1.1 Graphene

1.1.1 Atomic structure

Graphene is a 2D material formed by carbon atoms that are sp^2 hybridized[1, 2]. In this configuration (Figure 1.1.a) the C atoms have three sp^2 orbitals at 120° in the same plane. The remaining p orbital is not affected by hybridization, and it is perpendicular to the plane of the sp^2 bonds. The sp^2 structure has a trigonal shape with the nucleus in the center. The superimposition of the sp^2 orbitals of two different C atoms forms the σ type covalent bonds, while the p ones form π bonds. The resulting bond is a conjugated double bond with delocalized electrons on the entire crystal. This phenomenon is responsible for the peculiar electrical properties of graphene. The geometry of the bonds is the reason for the classic honeycomb shape of the organisation of C atoms in graphene.

The honeycomb lattice is not a Bravais lattice. The Bravais lattice is an infinite arrangement of discrete points whose structure is invariant under a certain group of translations[3]. As a matter of fact, it is not possible to obtain the nodes of the lattice with a linear combination of two vectors. The graphene lattice must be considered as a superposition of two triangular lattices A and B. With respect to an orthogonal base (X,Y in Fig. 1), the vectors of the unit cell are (Figure 1.1.b):

$$\vec{a}_1 = \frac{a}{2} \left(\frac{3}{\sqrt{3}}, 1 \right) ; \vec{a}_2 = \frac{a}{2} (0, 2) \quad (1.1)$$

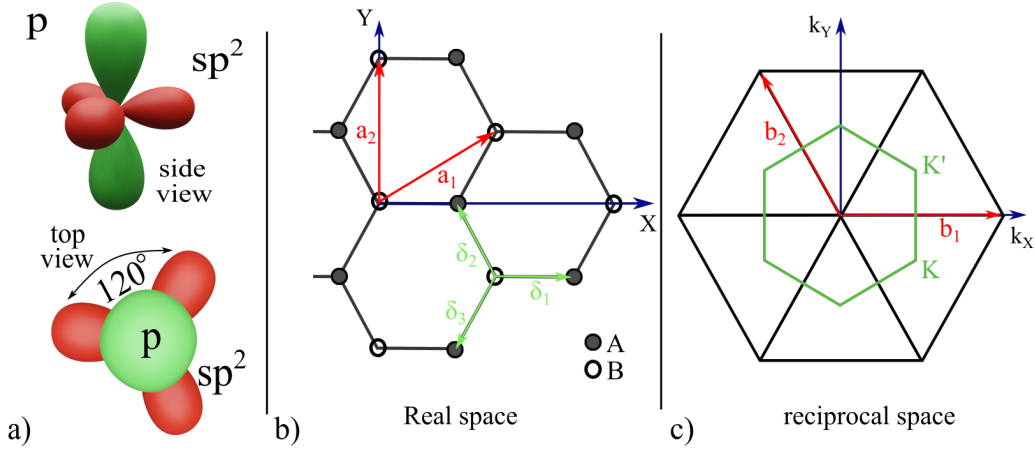


Figure 1.1: a) C atom in sp^2 configuration, b) real lattice, c) reciprocal lattice of graphene

where a of the order of 2.46 \AA is the lattice parameter of graphene. The three vectors that connect one sublattice with the other are:

$$\delta_1 = \frac{a}{2} (2\sqrt{3}, 0) ; \delta_2 = \frac{a}{2} \left(-1, \frac{1}{\sqrt{3}} \right) ; \delta_3 = \frac{a}{2} \left(-1, -\frac{1}{\sqrt{3}} \right) \quad (1.2)$$

The area of the unit cell is $\frac{3\sqrt{3}a^2}{2} = 0.051 \text{ nm}^2$.

The reciprocal lattice also has a hexagonal structure, whose vectors base are given by (Figure 1.1.c):

$$\vec{b}_1 = \frac{2\pi\sqrt{3}}{3a} \left(-1, \frac{3}{\sqrt{3}} \right) ; \vec{b}_2 = \frac{2\pi\sqrt{3}}{3a} (2, 0) \quad (1.3)$$

In the Brillouin zone, the points of symmetry Γ , M , K and K' can be recognized. Particularly important are the last two points, called Dirac points, at positions:

$$K = \frac{2\pi\sqrt{3}}{3a} \left(1, \frac{1}{\sqrt{3}} \right) ; K' = \frac{2\pi\sqrt{3}}{3a} \left(1, -\frac{1}{\sqrt{3}} \right) \quad (1.4)$$

1.1.2 Band structure

In graphene, the π orbitals are responsible for the conduction properties. The energy levels of the π -band in the reciprocal space can be derived using

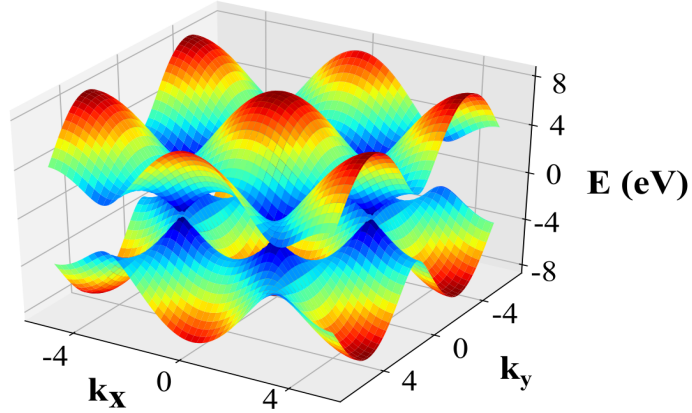


Figure 1.2: 3D representation of the band structure, derived from equation 1.5.

a tight-binding model[4]. The result in the first Brillouin zone is:

$$E(k_x, k_y) = \pm \gamma_0 \sqrt{1 + 4 \cos\left(\frac{\sqrt{3} a k_y}{2}\right) \cos\left(\frac{a k_x}{2}\right) + 4 \cos^2\left(\frac{a k_x}{2}\right)} \quad (1.5)$$

where $\gamma_0 \approx 2.8$ eV. The positive values are related to the conduction band, while the negative values are related to the valence band. As shown in Figure 1.2, the valence band and the conduction band coincide in 6 points called Dirac points (K and K'). The Dirac points, therefore, are situated at the Fermi level. For this reason (zero-gap), the graphene is considered a semi-metal. The vicinity of K and K' points the bands form two cones, called Dirac cones.

The mobility of the charge is very high ($200000 \text{ cm}^2/\text{V}\cdot\text{s}$, calculated for free-standing graphene[5]), making graphene an excellent electrical (and thermal) conductor.

1.2 CVD methods for the graphene growth

1.2.1 Principles of the techniques

Chemical vapour deposition (CVD) is a technique that takes advantage of the decomposition of one or more gases on the surface of a catalyzer to

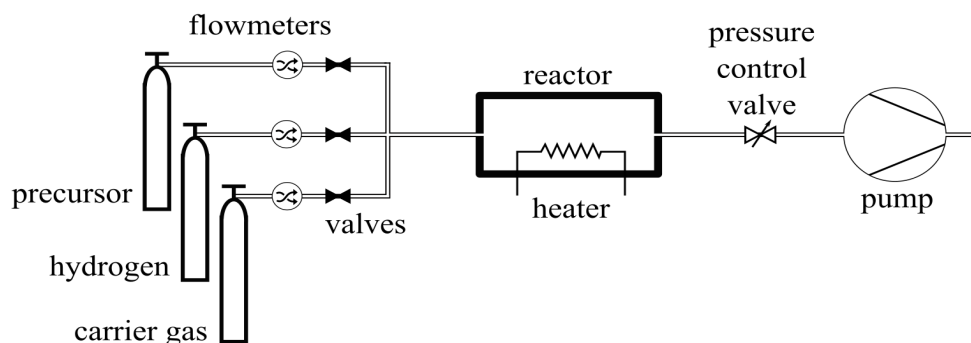


Figure 1.3: Functional diagram of a typical CVD device. Chemical deposition takes place in the reactor where the sample is heated by an external heater[9]

produce a crystal. It is a bottom-up process, and it is extremely effective for the synthesis of graphene[6, 7, 8]. A standard CVD set-up is shown in figure 1.3. The gases of the reaction are mixed in a gas-mixing unit and then are delivered to the reactor. In this unit, a gas flow controller can be set to control the partial pressure and the flow of the gases. The reactor is a chamber with controlled pressure and isolated from the atmosphere. The catalyzer is situated inside the reactor and on top of a heater. The pressure of the chamber is regulated by a proportional–integral–derivative (PID) controller connected with the exhaust line[9]. The gases used for the synthesis of graphene are usually three: a carbon precursor, a carrier gas, and hydrogen. The carbon precursor has molecules that contain carbon; its dissociation delivers the feedstock for the production of graphene. The carrier gas is an inert gas, while hydrogen is needed for controlling the equilibrium of the reaction or etch the material. The carbon precursor used in this thesis was CH_4 , and the carrier gas was argon.

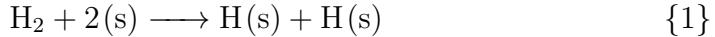
Transition metal surfaces are often used as catalyzers for the dissociation of C atoms from the precursor molecules. The catalytic activity and the carbon solubility are the two main properties of the catalyzers[10, 11]. The catalytic activity is the increase of the rate of a chemical reaction caused by a catalyst. In this case it is the ability of the metal to remove an atom of H from the gaseous precursor. The solubility is the quantity that measures the percentage of carbon inside the crystal matrix.

The dissociation occurs when the hydrocarbon donates an electron from the $C - H$ bond to the $3d$ orbital of the metal[11]. Now, the element with not

filled $3d$ orbital can easily accept this electron and dissociate the bond. The more electrons the metal has in the d orbital, the harder this process[11]. For example, Ni has electronic configuration $[\text{Ar}] 3d^8 4s^2$; it has two unpaired electrons; its activity and its solubility are higher than for the Cu $[\text{Ar}] 3d^{10} 4s^1$ that has filled d orbital and only one not filled s orbital. The mechanisms of the growth of graphene are different in one case respect to the other, and both are described below. The process of the growth of graphene consists of four steps:

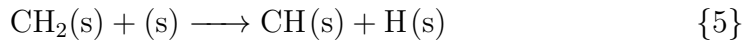
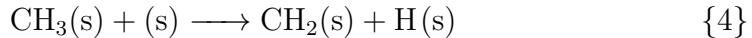
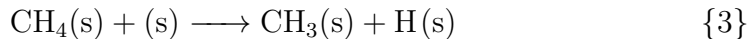
1. absorption and desorption of the precursor molecules at the surface of the catalyzer
2. de-hydrogenation reaction
3. diffusion of the C atoms on the surface or in the bulk of the metal
4. formation of graphene

In the first step, the H_2 is dissociatively chemisorbed, and the CH_4 physisorbed on the surface of the metal. The reactions on the surface site (s) are:



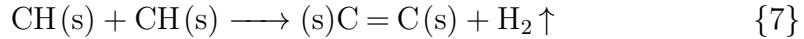
It is important to underline that the sticking coefficient depends on the metal. Coming back to the previous example, the sticking coefficient of H_2 is higher on Cu than on Ni, but the sticking coefficient of CH_4 is four times lower[11]. Furthermore, it is not possible to exclude the fact that a low amount of C atoms can react with the metal vapour before touching the surface.

The second step is the dehydrogenation of methane, which proceeds in the following four steps[12, 13, 14]:





All these reactions have different activation energies depending on the activity of the transition metal used. The reactions 1 and 3 are in competition; in Cu, for example, 1 is favored with respect to 3; this means that the H_2 molecules has an inhibitor role to the dissociation reaction. On copper, in particular, the energy of C atoms on the surface is higher with respect to the one of the CH_4 molecules; consequently, C-C dimers are more stable [11, 12]. For this reason, the reaction 6 is substituted with:



For the Ni case, *vice versa*, the hydrogen reacts less on the surface, and it easily recombines to form $\text{H}_2(g)$. Thus, the reactive sites for the dehydrogenation reaction are not occupied by H_2 , and they are more available[11].

As a third step of the graphene growth process, the carbon ad-atoms diffuse on the surface and in the bulk of the catalyzer. In some metals, the surface diffusion is favored with respect to the bulk diffusion or *vice versa*, leading to two different processes of formation of graphene that are presented below[6]. In all metals, however, both processes are always present. In metals with low carbon solubility, like Cu, for example, the C atoms tend to migrate only at the surface. During the growth, the graphene layer covers the reactive sites for the dehydrogenation. In this way, the reaction stops when a single layer is formed; for this reason, it is called a self-limiting reaction[15, 16]. For metals with higher solubility, like Ni, for example, the C atoms are adsorbed in the bulk of the material. When the temperature is decreased, the solubility decreases and the C atoms segregate at the surface of the metal. The precipitation process is not self-limiting because the C atoms segregate continuously until the equilibrium value is achieved[17, 18]. For such metals, tuning the thickness of the metal film, the cooling rate, and the exposure time to carbon precursors are essential parameters to be optimized.

The last step is the formation of graphene. In order to form a crystal, two processes must occur: the nucleation and the growth. In the classical theory of homogeneous nucleation, the probability of the formation of a cluster P for a number of atoms N is given by the formula[8]:

$$P(N) = N_s e^{\frac{-\Delta G(N)}{k_b T}} \quad (1.6)$$

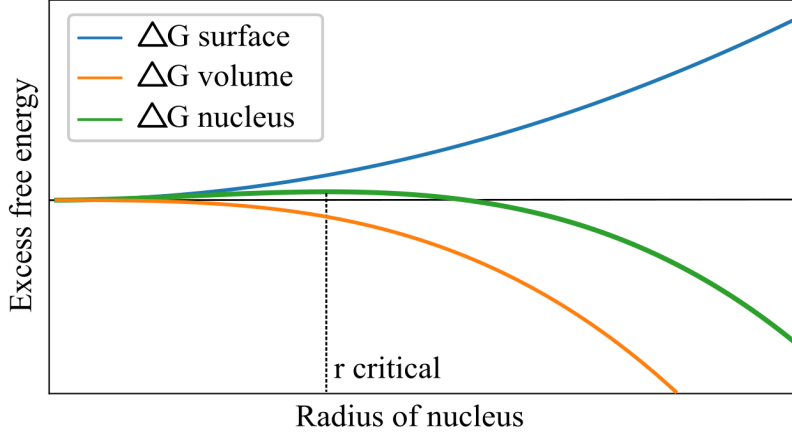


Figure 1.4: Free energy vs cluster size[19]. The blue line shows the negative energy contribution for the formation of a new bulk. In red, the positive contribution of the formation of a new surface. In green, the sum of the two terms.

where N_s is the probability of generating a cluster with a single monomer, T is the temperature, k_b is the Boltzmann constant, and $\Delta G(N)$ is the free energy of a system of N atoms. The last variable can be calculated as:

$$\Delta G(N) = \gamma A(N) - N\Delta\mu = \theta N^\alpha - N\Delta\mu \quad (1.7)$$

where γ is the surface tension of the bulk, $A(N)$ is the area of the cluster with N atoms, $\Delta\mu$ is the difference between the chemical potential of the ad-atoms and the graphene island, θ is a constant related to the bulk density of the new phase and $\alpha = 1/2$ for 2D materials[8]. The free energy, therefore, is the result of the competition between the negative energy formed by the creation of the bulk and the positive one related to the creation of a surface. Figure 1.4 shows the free energy trend with respect to the number of atoms. Even though the classical nucleation theory is not the most precise model to describe the nucleation, it exposes the concept of the energy barrier. The cluster, as a matter of fact, is unstable when it is composed of few atoms, and stable when it is bigger. Many papers use computational models to test the stability of the cluster during the first stages of the nucleation process, but the trend of the free energy is the same as described above. Many studies, however, reported that, in a real experiment, the nucleation density is strongly influenced by the morphology of the metal substrate. For example, steps and

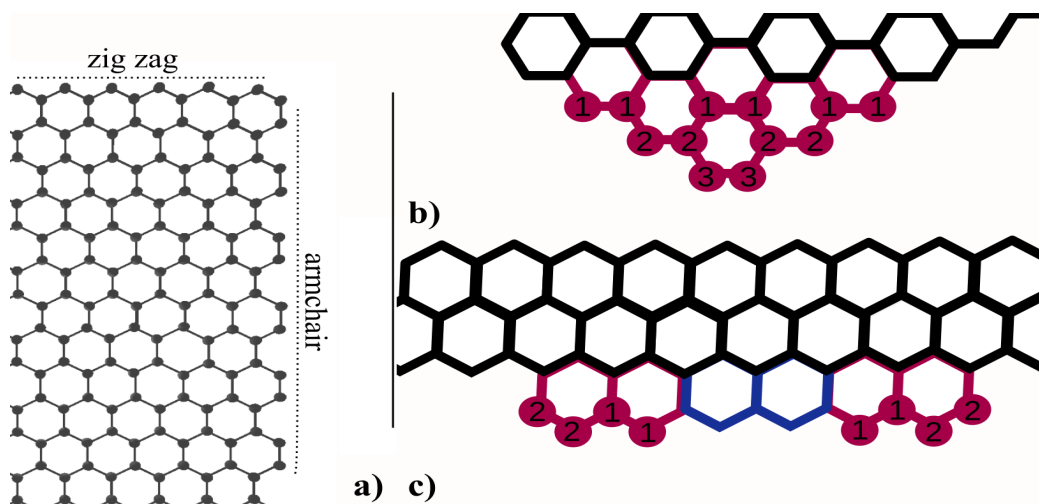


Figure 1.5: a) graphical representation of the zig zag and armchair edges of graphene. b) growth from the armchair edge,[25] c) growth on the zigzag edge[26]. The numbers on the image b) and c) represent the order of attachment of the atoms

kinks are preferential nucleation sites for graphene, as proven experimentally [20] and theoretically[21], in different materials. Grain boundaries[22, 23] and punctual defects [22] can also promote the nucleation of graphene. Even further, the grain boundaries of the substrate can promote the formation of multi-layers[24]. The presence of many nucleation points leads to the formation of a polycrystalline material with many defects and grain boundaries. Thus, the choice of the catalyst is of paramount importance; it should ideally be flat, and it should not promote the formation of many nucleation points. As will be described in Section 1.2.2, the liquid metals have both of these characteristics.

The growth is the process in which the graphene island increases its size. The path of the carbon atoms, from the surface of the metal to the final location in the crystal, can be divided into two steps. In the first place, C atoms diffuse on the surface of the metal until they reach the graphene nuclei or flake. Then, they diffuse on the edge of the flake to reach the most energetically favorable site[27, 28]. The edges of the graphene flake can be armchair or zigzag or a combination of the two, as shown in Figure 1.5.a[28, 29, 25, 26]. The angles between two edges of similar nature (only armchair or only zigzag) are $2n \cdot 30^\circ$, while the angles of two edges of different nature

are $(2n - 1) \cdot 30^\circ$ with n is a real number.

Even if the formation energies at the two edges are comparable, the energy of the carbon monomer attachment is different. The carbon monomer attachment on the armchair edge is, in fact, lower than on the zigzag edge[28]. Thus, the C atoms on the catalyst surface preferably stick to the armchair edges, "consuming" them until they disappear (see Figure 1.5.b). The flake, therefore, tends to assume a hexagonal shape with zigzag edges. Then, the cluster attachment on the side of the graphene creates a stable binding side for monomers, and the growth proceeds row after row (see Figure 1.5.c). The presence of zigzag edges on the flake grown with CVD is also proven with experimental data[26].

There are two kinds of growth, depending on the kinetics[28, 30]. If the carbon concentration is constant on the substrate of the catalyzer and the C atoms have enough time to diffuse on the edge of a flake, the growth is called *attachment limited*. The usual shape of a flake is a polygon (usually hexagon). On the other hand, if the rate of attachment of the carbon on the flake is too high, the C atoms attached to the graphene do not have the time to diffuse on the corner to reach more energetic favorable points. Even further, if the consumption of C atoms is too high, there is a depletion region of carbon atoms around the flake. This depletion region is more pronounced on the convex edges of the flake leading to an anisotropic distribution of carbon feedstock[31, 32]. The shape of the flake is then dendritic.

However, if the amount of feedstock on the surface of the catalyst is significant, the carbon atoms attached to the flake are not monomers or dimers anymore, but clusters. The shape of the flake is then irregular[33, 34]. In some cases, even with an attachment limited growth, the shape of the flake can be different from a hexagon. W.Guo *et al.* studied the effect of the growth of closed nucleation points[35]. As shown in Figure 1.6.a, the flakes merge in a single irregular one. The grain boundary of the flake can be directly determined by the geometry of the flake.

Another usual shape that can be observed is the star-like shape. In this case, the graphene flake may not contain grain boundaries; the shape is obtained because of the anisotropic concentration of the carbon feedstock around the flake. I.Vlassiouk *et al.* calculated the diffusion equation of the carbon[36]. As shown in Figure 1.6.b, the concentration gradient is higher around the corner with respect to the edge. For this reason, the corners of the flake receive more carbon atoms, and so they grow faster, the result is this particular shape.

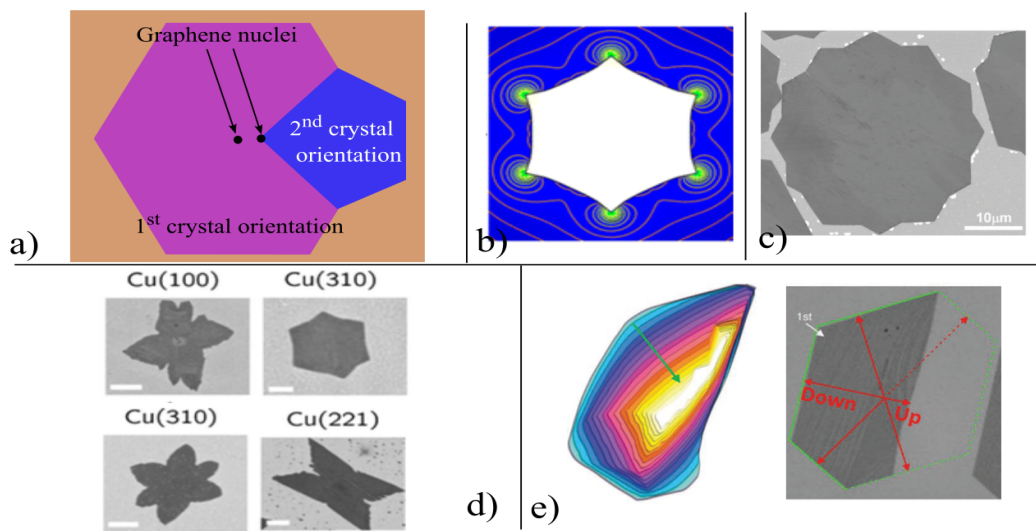


Figure 1.6: a) Shape of a multi-crystal flake. Figure inspired by Ref.[35], b) Flake star-like shaped (convex dodecagon), the lines are the equal concentration gradient calculated. Reproduced from Ref.[36], c) Twelve-fold symmetry shape. Reproduced from Ref.[37], d) Influence of the crystallographic orientation of the substrate on the shape of the flake. Reproduced from Ref.[38], e) Influence of the steps of the substrate, on the left the 3D morphology of the flake, on the right the SEM image. Reproduced from Ref.[24].

Another shape that can be found is the twelve-fold symmetric shape as shown in Figure 1.6.c[37]. This is explained considering that, to maintain the hexagonal shape of the flake, the carbon atoms attached to the flake need to migrate to a kink site. If the diffusion is fast enough, all atoms will reach these points. If the flake is too big, however, the atoms do not have time to find those points and so triangular tips nucleate. The edge of the nucleated tips have armchair shape, and, as explained before, they grow faster. Lastly, the shapes of the flakes are influenced by the solid substrate[38, 39]. Figure 1.6.d shows flakes grown on the same substrate with different crystallographic orientation. As can be seen, the graphene grows faster in some direction, with respect to others. Steps on the surface of the metal can also induce the growth of multi-layer islands with irregular shape as shown in Figure 1.6.d[24]. The influence of the substrate is evident for solid crystal catalyst and completely absent in the liquid ones[40].

1.2.2 CVD on liquid metals

1.2.2.1 Introduction

Liquid catalysts have a perfect morphology for the CVD growth of graphene because of their homogeneous and smooth surface (Subsection 1.2.2.2). Furthermore, graphene islands on the liquid surface have the possibility to rotate and self-align, leading to oriented flakes (Subsection 1.2.2.4). The quality of the graphene layer grown can be qualitatively characterized by etching the layer with H_2 (Subsection 1.2.2.3).

The first attempts with the liquid metals were made using alternative processes to the CVD. In 2009, for example, J.Fujita *et al* discovered the catalytic properties of Ga for the production of graphene[41, 42]. In this works, a film of amorphous carbon was in contact with liquid Ga, and then the sample was annealed at $1000^\circ C$. The process led to the formation of multi-layer graphene with a constant thickness.

One year later, S.Amini *et al.* tested liquid Cu and liquid Ni for the production of graphene. The metals were in contact with a graphite crucible that acted as a carbon source. After heating the sample, they realized that graphene was grown on the surface of the melted metal. The authors claim that the number of the layers can be tuned by tuning the parameters of the growth. Mono-layer with low defect density was as well achieved[43].

In 2011, Ga was used to assist the growth of graphene by SiC decompo-

sition. In the classical SiC decomposition, in fact, the Si evaporates from the material and the remaining carbon atoms on the surface form graphene. However, high evaporation of Si can damage the formed 2D material. The use of Ga can help because it has low solubility of carbon, together with the high solubility of Si. A drop of Ga, therefore, was poured on the SiC, and the sample was heated up to 1000°C; the graphene produced in this way has higher quality respect to the classic SiC ones[44].

The first article on the CVD growth of graphene on liquid metals is from 2012. D.Geng *et al.* grew graphene flakes on a liquid copper drop; they noticed the self-alignment of the flakes and a good conductivity[45]. A few months later, G. Ding *et al.* proved the feasibility of the growth of graphene on liquid gallium[46]. In the last article, in particular, other liquid metals and alloys (like In, Sn, In–Cu, Sn–Ni, and Sn–Ag–Cu) were tried with success. The latter is the most extensive study on the synthesis of graphene using liquid metals of different nature as catalysts. Most of the effort, in fact, is done on molten copper and in less amount on liquid gallium[46, 47, 48, 49]. The industrial application of LMCat process for graphene production are promising, and already one company is applying this technology. The polish company *Advanced Graphene Product*[®] patented their industrial process to grow graphene on liquid copper, and they claimed to have produced a graphene sheet of 1 meter. An alternative to the classical CVD method was proposed by Fujita *et al.*[50]. They discovered that there is a temperature below which the C atoms dissociated by the CVD start to diffuse in the bulk of gallium. In this paper, they poured a drop of Ga on a surface of a semiconductor, and they realized that the graphene was growing at the interface between gallium and the semiconductor. This process allows producing graphene directly on any substrate and at low temperature.

One of the standard features of the characterization of the graphene growth on liquid metals is that they are done *ex situ*. The graphene is grown on the liquid, then the liquid is solidified, and the sample is cooled down at room temperature; this, however, can lead to some uncontrollable effects[40, 51]. Mechanical stress, for example, can occur due to the different expansion coefficients of the metal and graphene. This stress can potentially create breaks and defects on the 2D material. Furthermore, during cooling, the growth process can still be present, even if the flow of the carbon precursor is stopped. The carbon can be present in the bulk of the material, and with the re-solidification, the solubility of the metal is changed. If it is lower, the carbon atoms in the bulk start to migrate to the surface and form graphene.

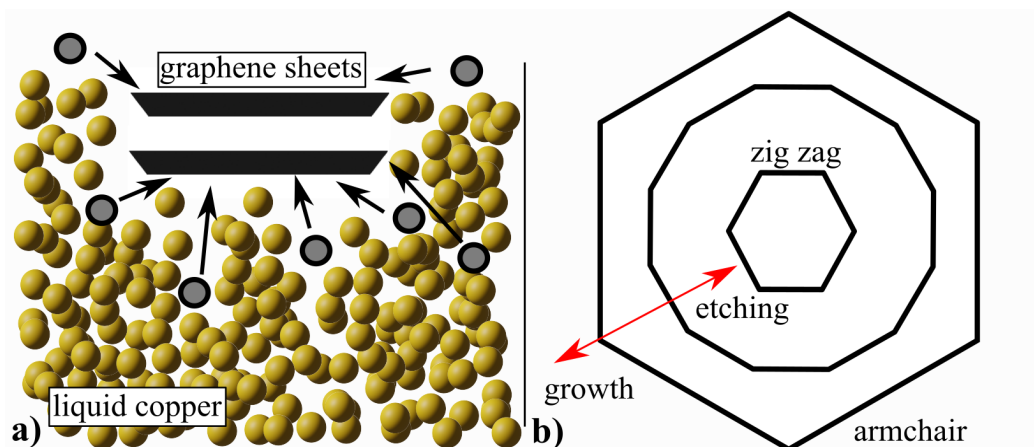


Figure 1.7: a) Graphical representation of the growth of multi-layer carbon domains on a liquid. The flake sinks in the liquid and the carbon atoms diffused under the metal surface. In this way, the flake grow uniformly. Figure inspired by Ref.[52]. b) Etching/growth behavior of the graphene on the left, shape of the flake at a different stage of the etching/growth. Figure inspired by Ref.[29].

In this way, on the surface, both the graphene formed previously on the liquid and later on the solid, are present. Lastly, an *ex situ* study can hardly give information on the dynamics of the motion of the flakes on the surface of the liquid, and usually, the conclusions are coming from speculation. In the LMCat project, for the first time, the graphene growth on liquid metal catalysts was studied *in situ*, bridging this gap and revealing new scenarios.

1.2.2.2 Nucleation and growth on liquid copper

On liquid copper, the graphene nucleation density is strongly reduced with respect to the solid counterpart.

As discussed in Section 1.2.1, the morphology of solid metal catalysts strongly influences the nucleation and the growth of graphene. In particular, defects on the surface can saturate the hydrocarbon bonds and so, trigger the nucleation. This effect, however, is not present on liquids, because of the smoother and uniform surface, and for this reason, the nucleation is rarer. The carbon atoms absorbed on the surface on the liquid metal tend to aggregate to one of the few nuclei grown to form a new one[53].

The growth on liquid copper has some differences with the solid. First of all, the potential barrier for the migration of C is lower on liquids than on solids. The carbon atoms can diffuse faster on the surface on the liquid and so can migrate faster to the graphene flake[27, 54]. The fastest growth rate achieved on liquid copper was $79 \mu\text{m}/\text{s}$ [53].

Another important difference is the anisotropy of the atom position on the metal. As discussed in Section 1.2.1, the lattice underneath the graphene increases the speed in some crystallographic direction with respect to others. This effect is absent on the liquid. In this way, researchers can better understand the growth mechanisms, as there is one less factor to consider.

Furthermore, it was proven with both Time-of-Flight Secondary Ion Mass Spectrometry (TOF-SIMS)[53] and *in-depth* X-ray photoelectron spectroscopy (XPS)[55] that the carbon solubility on the surface of the liquid copper is higher than the solid. This means that the C atoms can aggregate on the surface, as well as in the first atomic layers, into the liquid. This was proven flowing $^{13}\text{CH}_4$ and $^{12}\text{CH}_4$ alternately[53]. The graphene flake produced contained both isotopes uniformly. The main conclusion is that the growth is not self-limited, and it can lead to the formation of bi-layer or multi-layers (see Figure 1.7.a)[37, 52, 56, 57]. C. Zhang *et al.* in particular explained the mechanism of the growth of a multi-layer carbon domain through carbon diffusion of the first layers of the Cu atoms [52]. They also stated that, with the control of the partial pressure of the gases, it was possible to obtain a mono-, or a bi- or a multi-layer.

Another significant difference with the solid is the higher evaporation rate on liquids. The evaporation, from one side, leads to higher desorption of C clusters (limiting the nucleation)[36], and on the other hand, it promotes the de-hydrogenation of the carbon precursor. The evaporated copper atoms can, in fact, react with the hydrocarbon atoms and promote the decomposition[53].

Furthermore, from the computational simulation, it was proven that defect healing is promoted on the surface of the liquid copper with both thermodynamic[58], and kinetics considerations[59].

The advantage of liquid metals, therefore, is that the low nucleation is naturally accompanied by fast growth[52]. The crystal morphology is not affected by the substrate, and the defects are almost immediately removed. With the tuning of the partial pressure of the gas, it is possible to control the size of the flake as well as the number of layers. The quality of the graphene produced was tested with electrical measurements and with Raman spectroscopy, and

it shows better behaviour with respect to the one created on solid[54, 60]. One of the drawbacks of using liquid copper is that the energy needed to melt the metal is high. The use of an alloy, however, can significantly decrease the temperature, maintaining the advantages of the liquid surface. It was proven that on Cu-Ga, high-quality graphene could be produced at 800°[61].

1.2.2.3 Etching behaviour

The etching is the reverse process of growth. It happens when the chemical potential of the carbon precursor is lower than the one of the crystal. In this case, the number of atoms that stick to the flake is less than the number of detached ones, and the sample begins to shrink.

The etching starts from the corners or the defects of the flake[62, 63, 64]. The etching is a cheap and fast way to characterize the quality of the graphene synthesized and, even if it is a destructive method, it allows to reveal the defects (vacancies, grain boundaries), which may be visualised, with limited resolution, by electron or optical microscopy.

As shown in Figure 1.7.b, the etching consumes faster the zigzag edges and slower the armchair ones[29]. At the beginning of the etching, the corners of the flake are consumed faster than the border. In the intermediate state, the zigzag and armchair edges are both present, and the flake has a dodecagon shape. As time passes, the zigzag edges are completely consumed, and the flake has a hexagonal shape rotated by 45° respect to the starting one.

There are two types of etching, anisotropic and isotropic. The anisotropic etching leads to the formation of a fractal shape. It is a diffusion-limited process, and it is due to the fast rate of detachment of the C atoms from the flake. The hydrogen radicals, once they reach the flake, need to diffuse along the border to find the most energetically favourable sites. If the etching is too fast, the hydrogen cannot find these sites and this leads to a branched structure[65].

D. Geng *at al.*, however, showed that on liquid copper, the etching could also be isotropic[66]. They showed that a micrometer size flake was etched in small and uniform flakes with common orientation. The authors claim that it is possible to pass from isotropic to anisotropic etching, changing the flow of hydrogen. In particular, they noticed a transition from the array etching with a H₂ flux between 10-40 sccm to an anisotropic with 40 sccm (with 1500 sccm Ar).

1.2.2.4 Self assembling

One of the most exciting properties of liquid metal catalysts is that the flakes can slide and rotate. Already from the first experiments, it turned out that the flakes self-align in a common direction[67]. Some studies were done to understand the nature of the self-alignment; however, the mechanism is not fully understood. The most significant advantage of the self-alignment is that, in theory, the different flakes can grow and attach without lattice mismatch, thus, reducing the grain boundaries[68].

In 2012 Geng *et al.* showed the results of CVD growth on liquid copper. The SEM images acquired after the growth showed that the graphene islands do not present order at low coverage of the Cu surface. When the density of graphene crystals increased, the order appeared. They stated that the origin of this alignment was due to the sample constrains[45].

A few years later, D. Geng *et al.* explained the self-alignment as a result of the attraction due to the capillary interactions[57]. This theory, however, does not explain the repulsion of the flake at a short distance.

In 2016 a different theory was proposed [69]. In this case, the authors calculated the electrostatic potential of the flake of graphene, and they found an anisotropic electrostatic potential distribution that increases with the size of the flake. Furthermore, they realized that the flakes can also be rotated, increasing the flux of the gases; in this way, it was possible to tune the direction of the alignment.

A uniform distribution of the graphene was obtained by the self-alignment of alumina seeds. The Al_2O_3 particles are negatively charged in the liquid metals, and they repel each other. In this way, they are uniformly distributed on the surface of the metal. When the carbon precursor is flown, they act as nucleation points for the graphene[70].

In a recent paper, the authors proved that the flow of the gases is an essential factor for the alignment of the flakes[71]. The graphene islands, in fact, are aligned with the shear flow on the surface. They also measured a critical temperature above which the flakes were arranged in a random orientation. From the MD calculations, they assert that the different temperature behavior is due to different viscosity on the surface, which favours or limit the drift of the graphene.

Finally, S.Cingolani *et al.* questioned the reliability of the above papers, and they propose that the self-assembling is due to a compromise between the long-distance attraction due to capillary wave and a short repulsion due to

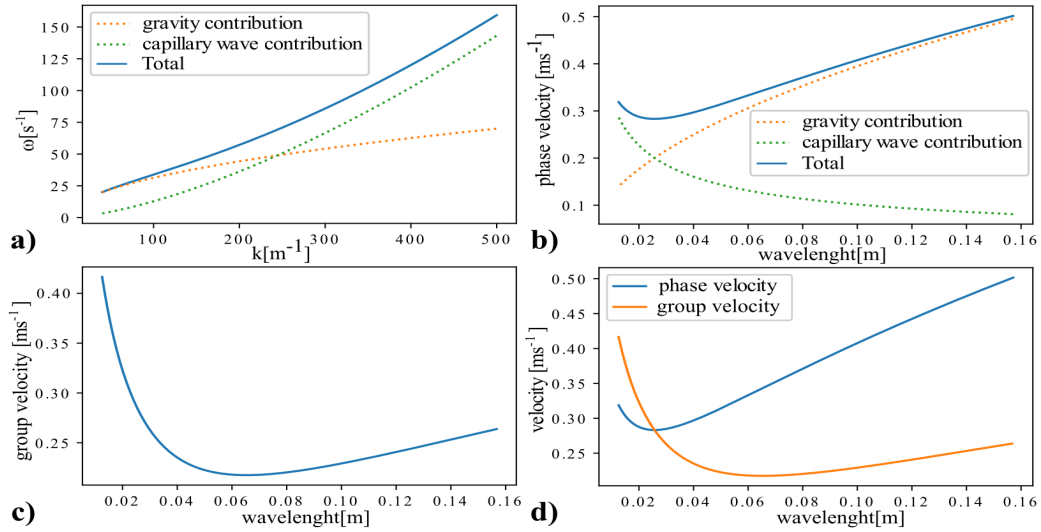


Figure 1.8: Dispersion relation of the capillary wave on liquid copper calculated with the Equation 1.8. a) plot ω vs k . b) Phase velocity vs wavelength. c) group velocity vs wavelength. d) comparison of the phase velocity and the group velocity at different wavelength.

electrical repulsion[72]. Those hypotheses were also made thanks to the observations obtained with the optical microscope described in Chapter 4. Even if the nature of the alignment is not fully understood, the process is useful, and it can significantly increase the speed of the coverage of the substrate with a high-quality material. When two flakes merge, as a matter of fact, they can create a boundary defect. The defects created between aligned flaked are low angle type, and they do not form overlapping zones [73]. Furthermore, it was proven that the defects can be significantly decreased with the increase of the partial pressure of the carbon precursor at the end of the growth[74].

1.3 Liquid surface

1.3.1 Liquid roughness

The common experience suggests that the surface of a liquid is not completely flat, but waves oscillate. Those waves depend on the density of the liquid

ρ as well as the surface tension γ . For each wavevector, k , it is possible to associate a single frequency ω . The dispersion relation for the capillary wave is then given by the formula[75]:

$$\omega^2 = \frac{\gamma k^3}{\rho} + gk \quad (1.8)$$

where g is the gravitational acceleration. ω^2 is composed of two terms; the first one is related to the capillary wave, and it is higher at higher k . The second one is due to the gravitational contribution, and it is higher at low k . In Figure 1.8, the dispersion relation of the capillary wave for the liquid copper is shown; it is possible to notice that the minimum of the phase velocity is at 2.6 cm/s, the cut-off of the capillary wave. This happens at the critical wavelength λ_m , so called cut-off length; its value can be calculated as $\lambda_m = 2\pi \sqrt{\frac{\gamma}{\Delta\rho g}}$.

Thermally excited capillary waves smear out the gas-liquid interface. The effective width of the liquid interface is directly proportional to the temperature, and it can be obtained with the formula[76]:

$$\sigma_{cap}^2 = \frac{k_b T}{4\pi\gamma} \ln \left(\frac{q_{max}}{q_{min}} \right) \quad (1.9)$$

Where k_b is the Boltzmann constant, T is the temperature in Kelvin, q_{max} is the short wavelength cut-off, and q_{min} is the long-wavelength cut-off. q_{max} corresponds to the shortest wavelength that can be produced, and it can be calculated approximately as $2/r_a$ with r_a is the radius of the molecule composing the liquid[75]. q_{min} is the minimum of the dispersion relation, where the contribution of the gravitational wavelength starts to be important. For the liquid copper at the melting point (1373.15 K) $\sigma = 2.53 \text{ \AA}$.

1.3.2 Capillary interactions

When a particle interacts with the surface of a liquid, it modifies its shape. Figure 1.9.a shows the forces acting on a spherical particle. The buoyancy force has the opposite direction to the gravity force. The capillary forces acting on the side prevent the object from sinking (if it is denser than the liquid) or detaching (if it is less dense). The forces that the particles on the surface of the liquid experience can be gravitational dominant or capillary

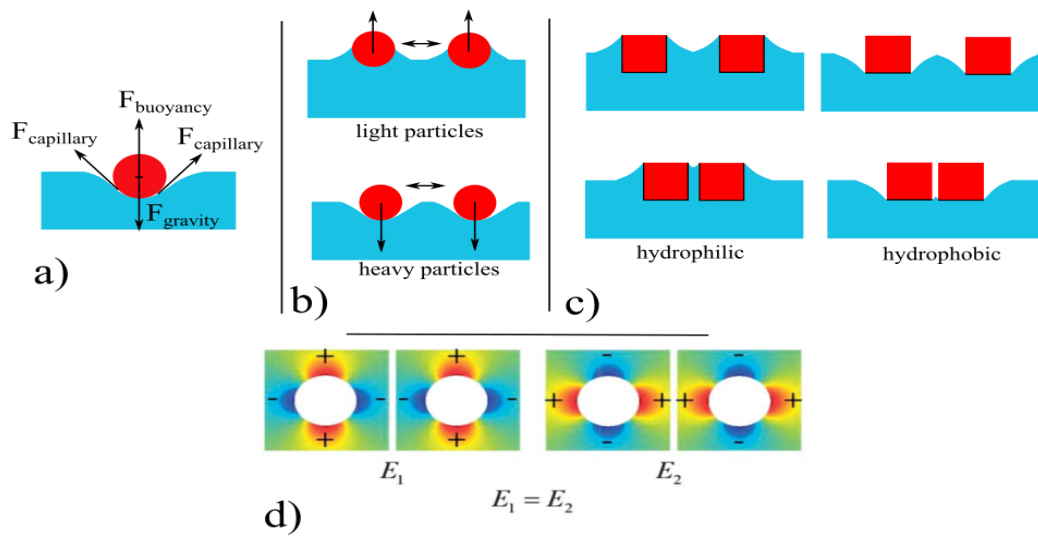


Figure 1.9: a) forces acting on the particle on the surface of the liquid. b) different behaviour for light and heavy particles. c) attraction of two hydrophilic and 2 hydrophobic particles. In the closer particles configuration, the surface of the liquid is less exposed. d) quadrupole interaction. Reproduced from Ref.[77].

dominant. The Bond number measures this effect, and it is given by the formula[78]:

$$Bo = \frac{\vec{F}_{gravity} - \vec{F}_{buoyancy}}{\vec{F}_{capillary}} = \frac{\Delta\rho L^2}{\gamma} \quad (1.10)$$

where $\vec{F}_{gravity}$ is the gravity force, $\vec{F}_{buoyancy}$ is the force due to buoyancy, $\vec{F}_{capillary}$ is the capillary force, L is the radius of the particle, $\Delta\rho$ is the density difference between the particle and the liquid, and γ is the surface tension. If $Bo > 1$, the gravitational forces are dominant, *vice versa* is $Bo < 1$, the capillary ones are dominant.

In the gravitational regime, the light particles (respect to the liquid density) have a $|\vec{F}_{buoyancy}| > |\vec{F}_{gravity}|$ and, therefore, are “pulled upwards” respect to the liquid plane. In contrary, for the heavier ones, the force of gravity push them downwards; both of this behaviour are shown if Figure 1.9.b. The light particles tend to go to the highest regions of the surface of the liquid, on the contrary, the heavy ones the lowest. Once the light particle interacts with the surface of the liquid, this latter modifies its shape pulling the meniscus upwards. For this reason, it attracts other light particles that are “looking for” higher meniscus and repel the heavy ones. For the same reason, massive particles attract heavy ones and repel light ones. It is possible to associate an imaginary sign to this behavior: the lower density ones have a positive “charge”, while the heavy ones, a negative charge. Two particles with the same sign attract, while two of different nature repel.

With a $Bo < 1$, the particles are in the capillary dominant regime. The meniscus of the liquid is mainly affected by the hydrophilicity/hydrophobicity of the surface, as shown in Figure 1.9.c. The liquid tends to minimize the surface tension approaching the particles. As the Figure shows, the surface with two closer particles is lower than the one with two particles far apart. The two menisci, as a matter of fact, overlap when the two particles are closer and the liquid surface exposed is lower. As in the gravity regime, also here, it is possible to assign a sign: the hydrophobic particles have a positive sign while hydrophilic ones have a negative one. Particles with the same sign tend to aggregate while particle with the different signs repel. The behavior of particles in the gravity regime is the same as the one in the capillary wave regime, even though the physics behind is slightly different. The Bond number for graphene (with $L = 0.5$ mm) on the liquid copper is 0.001, in the capillary dominant regime.

In the description above, the particle is considered to be isotropic. However,

the same particle can have an undulated, or irregular contact line due to chemical or physical inhomogeneity. In this case, the object can be modeled as a multi-pole charged particle. The particles in this situation attract and orient each other in order to have the same charge closer (Figure 1.9.d)[79, 80, 77].

Chapter 2

Characterization techniques

2.1 X-ray diffraction

2.1.1 Interaction between matter and x-ray

The x-ray scattering technique uses x-ray photons to probe the surface of a material. X-ray photons induce vibrations of the electrons of the atoms, which in turn produce a secondary electromagnetic wave (Thompson scattering). The waves created by the electrons of the material interact with each other, and they create constructive and destructive interference depending on the position of the atoms in the unit cell. The angular distribution of the intensity of the scattered wave gives information on the spatial electron density distribution.

The LMCat project aims of studying the 2D materials on the surface of molten metals. In this chapter, the scattering from surfaces and liquids are described.

Below, I present a set of formulas that describe the scattering of x-rays from a liquid-2D layer interface, starting from the scattering of a photon on an electron, and then more complex scattering with an electronic cloud. Later in the chapter, different scenarios are presented: first, the the diffraction by a 3D crystal is derived, then by a 2D crystal, and a surface of a crystal; finally, by a liquid. In these models, multiple scattering events of the photon are neglected (kinematical approximation).

When a photon interacts with an electron, the latter generates another electromagnetic wave. The relation between the incoming amplitude and the

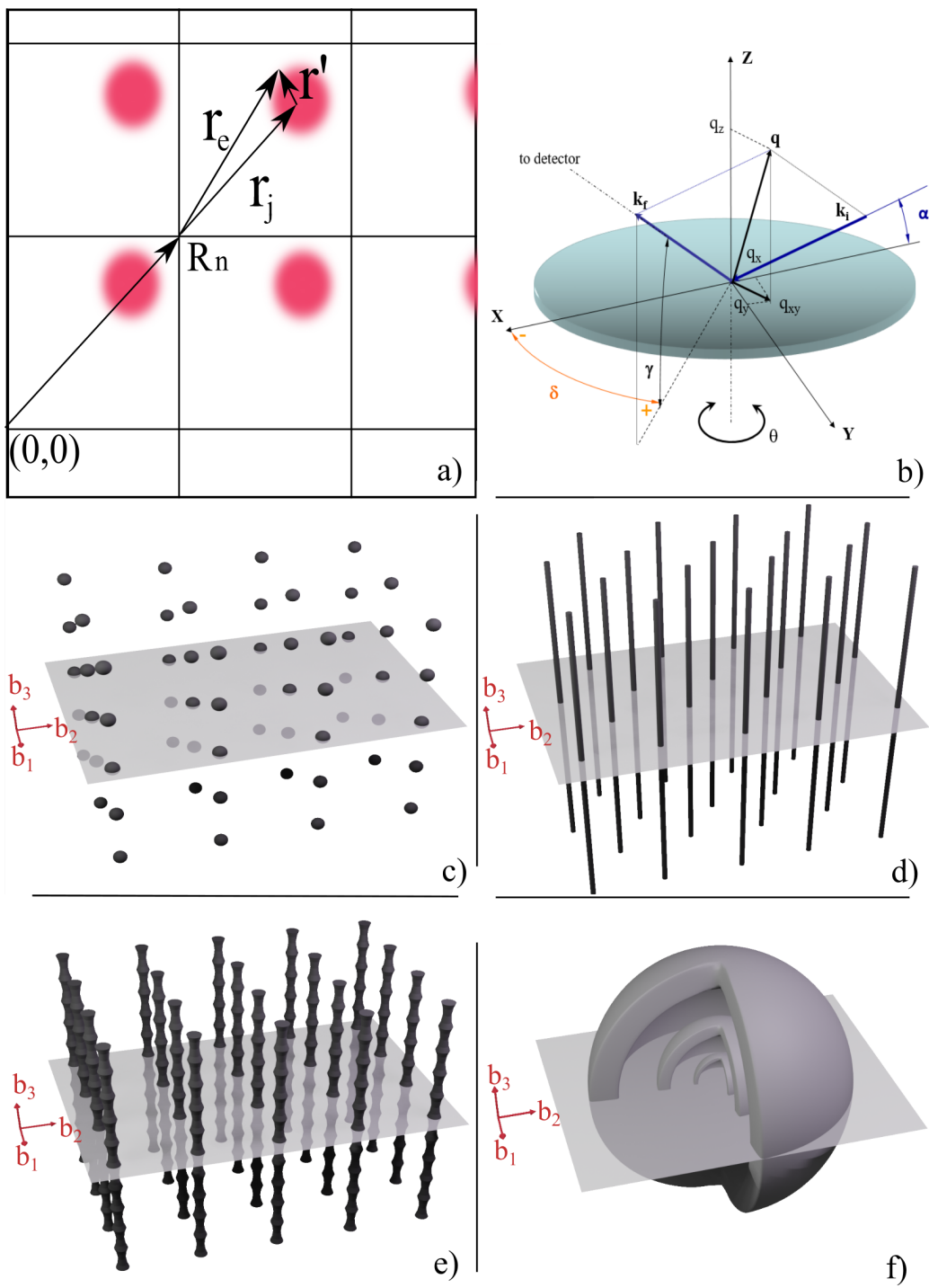


Figure 2.1: (Caption in the next page.)

Figure 2.1: a) The vectors describing the “position” of an electron for any atom in the crystal: \vec{R}_n is the vector between the origin of the lattice and the unit cell, \vec{r}_j the distance of the j^{th} atom in the unit cell from the origin of the unit cell, \vec{r}' is the vector connecting the center of the atom to the electron and \vec{r}_e is between the electron and the origin of the unit cell. b) Geometry of a surface diffraction experiment. The incident beam with wavevector \vec{k}_i is impinging on the surface of the crystal (green disk) with an angle α . The diffracted beam has $|\vec{k}_f| = |\vec{k}_i|$. The difference between \vec{k}_f and \vec{k}_i gives the scattering vector \vec{q} . The sample can be rotated by an angle θ with respect to the z axis perpendicular to the surface. δ defines the horizontal angle of the detector. c) Graphical representation of the reciprocal space of a 3D crystal, the dots represent the Bragg’s peaks. d) Graphical representation of the reciprocal space of a 2D crystal, e) Graphical representation of the reciprocal space of the surface of a 3D crystal, f) Graphical representation of the scattering by a liquid.

generated one is given by the Thomson formula:

$$A_1 e^{-i\vec{k}_f \cdot \vec{r}_e} = A_0 \frac{e^2}{mc^2} \frac{1}{R_0} e^{-i\vec{k}_i \cdot \vec{r}_e} \quad (2.1)$$

where A_1 is the amplitude of the scattering wave, A_0 is the incoming amplitude wave, e is the electron charge, m is the mass of the electron and R_0 is the distance to the observer. If we define a vector \vec{q} as

$$\vec{q} = \vec{k}_f - \vec{k}_i \quad (2.2)$$

as shown in Figure 2.1.b, the Formula 2.1 can be rewritten as:

$$A_1 = A_0 \frac{e^2}{mc^2} \frac{1}{R_0} e^{i\vec{q} \cdot \vec{r}_e} \quad (2.3)$$

The vector \vec{q} is called scattering vector.

Now let us increase the complexity by considering that the scattering is not coming from an electron but from an atom. In this case, the electronic density distribution must be taken into consideration. If we define R_n as the distance between the origin of the lattice and the j^{th} unit cell, r_j the distance of the atom in the unit cell with respect to its origin and r' the position of the

electron with respect to the atom (see Figure 2.1.a), the scattering amplitude is:

$$A_2 = A_0 \frac{e^2}{mc^2} \frac{1}{R_0} \int_{-\infty}^{+\infty} \rho(\vec{r}') e^{i\vec{q} \cdot (\vec{R}_n + \vec{r}_j + \vec{r}')} d^3r' = A_0 \frac{e^2}{mc^2} \frac{1}{R_0} f(\vec{q}) e^{i\vec{q} \cdot (\vec{R}_n + \vec{r}_j)} \quad (2.4)$$

where

$$f(\vec{q}) = \int_{-\infty}^{+\infty} \rho(\vec{r}') e^{i\vec{q} \cdot \vec{r}'} d^3r' \quad (2.5)$$

is defined to be the atomic form factor. The atomic form factor is the Fourier transform of the electron density of the atom. The Equation 2.4 is the starting point to understand x-ray scattering by materials as is described below. The derivation of the models of Section 2.1 are taken from the main books[81, 82] and articles[83, 84, 85] about x-ray diffraction.

2.1.2 Scattering from a 3D crystal

In a crystal, atoms are placed in a repetitive pattern following the translational symmetry. The structure of the crystal can be associated with one of the Bravais lattices. The smaller repeating unit is called the unit cell. Equation 2.4 gives the amplitude of the scattering by a single atom. In order to deduce the scattering from a unit cell, we add linearly the scattering coming from all the atoms in the unit cell:

$$A_3 = A_0 \frac{e^2}{mc^2} \frac{1}{R_0} \sum_{j=1}^{N_c} f_j(\vec{q}) e^{i\vec{q} \cdot (\vec{R}_n + \vec{r}_j)} = A_0 \frac{e^2}{mc^2} \frac{1}{R_0} F(\vec{q}) e^{i\vec{q} \cdot \vec{R}_n} \quad (2.6)$$

where

$$F(\vec{q}) = \sum_{j=1}^{N_c} f_j(\vec{q}) e^{i\vec{q} \cdot \vec{r}_j} \quad (2.7)$$

is the structure factor of the unit cell. As mentioned before, all atoms in the unit cell emit spherical waves; those waves interact one with the other and diffract. The distribution of electronic density in the unit cell, which we can obtain by analyzing diffraction patterns, is contained in the structure

factor. Now the waves scattered by all the unit cells will be added to obtain the final result:

$$A_4 = A_0 \frac{e^2}{mc^2} \frac{1}{R_0} F(q) \sum_{n_1=0}^{N_1-1} \sum_{n_2=0}^{N_2-1} \sum_{n_3=0}^{N_3-1} e^{i\vec{q} \cdot (n_1\vec{a}_1 + n_2\vec{a}_2 + n_3\vec{a}_3)} \quad (2.8)$$

The sum in the equation 2.8 can be solved as:

$$S_n(x) = \sum_{n=0}^{N-1} e^{inx} = \frac{1 - e^{ixN}}{1 - e^{ix}} \quad (2.9)$$

With $x = q \cdot a$. The function $|S_n(x)|^2$ has a peak in $q \cdot a$ that is low and broad if N is low, and it gets sharper if N increases. For μm size crystals, N is normally very high.

The diffraction occurs when:

$$\begin{aligned} \vec{q} \cdot \vec{a}_1 &= 2\pi h \\ \vec{q} \cdot \vec{a}_2 &= 2\pi k \\ \vec{q} \cdot \vec{a}_3 &= 2\pi l \end{aligned} \quad (2.10)$$

The relations 2.10 are called Laue's conditions. h, k, l are integer numbers and they are called Miller indexes. The Miller indexes indicate the planes that produce diffraction; those planes intercept the base vector in $(a_1/h, a_2/k, a_3/l)$. A simple and effective way to predict the diffraction positions is using the Braggs' formula:

$$n\lambda = 2d_{hkl} \sin\theta \quad (2.11)$$

where d_{hkl} is the distance between the miller planes, n is a real number, and θ is half the angle between k_i and k_f . This formula, however, does not help to calculate the intensity of the scattered wave but only the radial position. In the Laue formulation, the diffraction is described with the help of the reciprocal space concept. The diffraction is verified only if:

$$\vec{q} = h\vec{b}_1 + k\vec{b}_2 + l\vec{b}_3 \quad (2.12)$$

which expresses that \vec{q} is a vector in the reciprocal space, and it defines the angular distribution of the diffraction. b_1, b_2, b_3 are the basis vectors of the

reciprocal space, given by:

$$\vec{b}_1 = 2\pi \frac{\vec{a}_2 \times \vec{a}_3}{\vec{a}_1 \cdot \vec{a}_2 \times \vec{a}_3}, \quad \vec{b}_2 = 2\pi \frac{\vec{a}_3 \times \vec{a}_1}{\vec{a}_2 \cdot \vec{a}_3 \times \vec{a}_1}, \quad \vec{b}_3 = 2\pi \frac{\vec{a}_1 \times \vec{a}_2}{\vec{a}_3 \cdot \vec{a}_1 \times \vec{a}_2} \quad (2.13)$$

Figure 2.1.c is a graphical representation of the reciprocal space of a 3D crystal. Substituting 2.14 in 2.8, the resulting intensity of the scattered waves can be derived as:

$$I_{hkl} = \left| A_0 \frac{e^2}{mc^2} \frac{1}{R_0} F(h\vec{b}_1 + k\vec{b}_2 + l\vec{b}_3) N_1 N_2 N_3 \right|^2 \quad (2.14)$$

As we discuss, the diffraction occurs if the vector \vec{q} is intersecting a point of the reciprocal space. If the diffraction process is elastic, the incident wave vector and the scattered one have the same length: $|\vec{k}_f| = |\vec{k}_i| = \frac{2\pi}{\lambda}$. Formula 2.2 shows that \vec{q} is the difference between \vec{k}_f and \vec{k}_i . Therefore, it is possible to imagine that all the allowed \vec{q} lie in a sphere of radius $\frac{2\pi}{\lambda}$ passing through the origin of the reciprocal space. This sphere is called Ewald sphere and the diffraction can be detected in the points in which the sphere intersects the reciprocal space of the material.

2.1.3 Surface x-ray diffraction

The scattering amplitude coming from a 2D material is straightforward to calculate, starting from Equation 2.14. We can limit, as a matter of fact, the problem in two dimensions, removing the factor containing a_3 . In the reciprocal space, along the h, k plane, the periodicity of the lattice remains unchanged. Along l , however, the interference signal has a finite length; the reciprocal space is shown in Figure 2.1.d, and it is a series of parallel vertical lines called 2D rods. The intensity is:

$$I_{2DROD}(\vec{q}) = \left| A_0 \frac{e^2}{mc^2} \frac{1}{R_0} F(\vec{q}) N_1 N_2 \right|^2 \quad (2.15)$$

Particularly interesting is the case of diffraction from the surface of a bulk single crystal. The effect of a truncated crystal on the diffraction pattern can be easily understood in this way: in order to have a finite lattice with a sharp interface, the lattice of the crystal must be multiplied by the step function. The convolution theorem states that the Fourier transform of the

product of two functions is the convolution of the Fourier transforms of each function. The Fourier transform of the real lattice is the reciprocal one, while the Fourier transform of the step function is a hyperbole. That means that there is a modulation of intensity between Bragg peaks perpendicular to the surface, forming the so-called crystal truncation rods (CTR) perpendicular to the surface. The intensity of the scattered wave coming from a truncated crystal is shown in Figure 2.1.e, and it differs from the Equation 2.15 by an oscillatory function in a_3 (for a square unit cell):

$$I_{CTR}(\vec{q}) = \left| A_0 \frac{e^2}{mc^2} \frac{1}{R_0} F(\vec{q}) N_1 N_2 \right|^2 \frac{1}{2 \sin^2(\vec{q} \cdot \vec{a}_3 / 2)} \quad (2.16)$$

For the case of graphene on liquid copper, the Grazing Incident X-ray Diffraction (GIXD) can already discriminate if the carbon material grown is graphene or multi-dimensional structure. The modulation of intensity with \vec{q}_z is symptomatic of a periodicity in the vertical plane. This technique can be complementary to X-Ray Reflectivity (XRR) (described in Section 2.2) in this sense.

2.1.4 Scattering from a liquid

The structure of a material in the liquid phase is characterized by the lack of long-range order. For this reason, the position of the atoms can be provided only by a statistical distribution. The Radial Distribution Function (RDF) is the function that is classically adopted to describe the atoms of a liquid. The RDF can be made by choosing the center of one atom as an origin of a sphere of radius r and thickness dr . Then the radial density is defined as the average of electron density cloud $N(r)$ that the annulus, of radius r and thickness dr , intersects, and it is calculated as $\rho(r) = \frac{N(r)}{4\pi r^2 dr}$. The normalized RDF is the ratio between the radial density and the electron density of the single atom:

$$g(r) = \rho(r) / \rho_{at} \quad (2.17)$$

The RDF is 0 if r is smaller than the liquid atom radius; then, when the radius of the sphere is comparable to the distance of the first neighbour atoms, there is a peak. The other peaks, corresponding to the second, third etc. neighbours are less intense and broader. At high r , $g(r)$ is equal to 1.

Starting from the Equation 2.5, it is possible to demonstrate that the structure factor of a liquid ($S(\vec{q})$) is:

$$S(q) = 1 + \frac{4\pi}{q} \int_0^\infty r[\rho(r) - \rho_{at}] \sin(qr) dr \quad (2.18)$$

A graphical representation of the reciprocal space of the liquid is shown in Figure 2.1.f. The Equation 2.18 can be re-written as:

$$q[S(q) - 1] = \int_0^\infty H(r) \sin(qr) dr \quad (2.19)$$

with $H(r) = 4\pi r[\rho(r) - \rho_{at}] = 4\pi\rho_{at}[g(r) - 1]$. $H(r)$ represent the deviation of the atomic density from its average. The inverse Fourier transform of Equation 2.19 gives:

$$H(r) = \frac{2}{\pi} \int_0^\infty q[S(q) - 1] \sin(qr) dq \quad (2.20)$$

rearranging Equation 2.20, the RDF can be derived directly from $S(q)$:

$$g(r) = 1 + \frac{1}{2\pi^2 r \rho_{at}} \int_0^\infty q[S(q) - 1] \sin(qr) dq \quad (2.21)$$

The last equation is interesting because it underlines that it is possible to derive the RDF directly from the structure factor of the liquid.

2.2 X-ray reflectivity

X-ray reflectivity (XRR) is a technique used to determine the out-of-plane density profile of a surface. It measures the reflected specular beam intensity as the function of the incidence angle (or q_z). The reflectivity is defined as:

$$R(q_z) = \frac{I(q_z)}{I_0} \quad (2.22)$$

where I is the intensity at a given q_z , and I_0 is the incident beam intensity. In order to follow the reflected beam, the detector and the incident beam are rotated from the same angle on the plane perpendicular to the sample plane. The XRR combines an extremely high spatial resolution (order of Å), high element specificity, and the possibility of doing measurements *in situ*

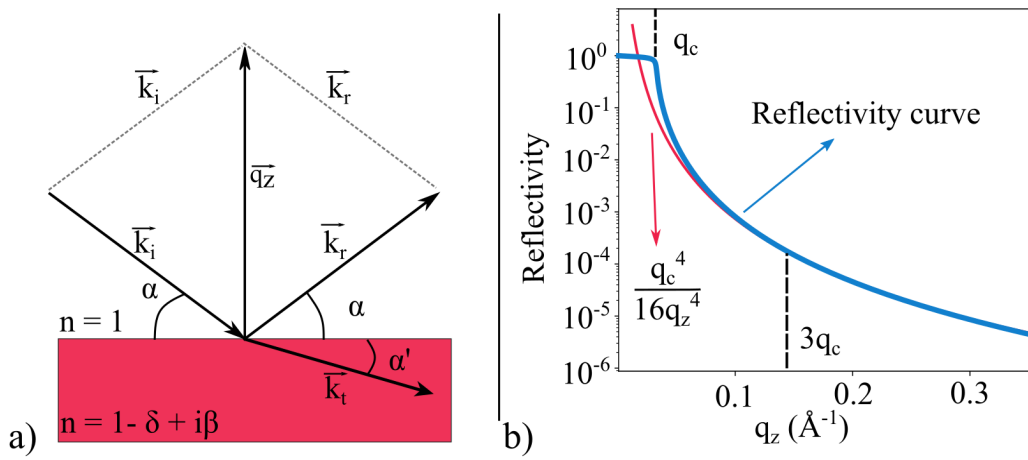


Figure 2.2: a) In a XRR experiment, the incident vector \vec{k}_i intercepts the surface of the sample (red rectangle) with an angle α . The electromagnetic wave is partially reflected and partially absorbed. The reflected wave with \vec{k}_R makes an angle α with the surface of the sample, while the transmitted wave \vec{k}_T an angle α' . If the experiment is performed in vacuum, the refractive index outside the sample is 1, while inside the material is $n = 1 - \delta - i\beta$. b) The trend of the reflectivity curve, the reflectivity is 1 for $q_z < q_c$, then it has a fast decrease until $q_z \sim 3q_c$, where the curve decreases $\propto q_z^{-4}$.

in controlled atmosphere reactors. It is a perfect technique in this project because it allows to measure the graphene on liquid metal at 1373 K without particular problems. The theory described below can be found in classic books of XRR[81, 86, 75].

2.2.1 Snell's law and Fresnel reflectivity

When a ray (with function $\Psi_i = a_i e^{i\vec{k}_i \cdot \vec{r}}$) impinges on a surface of a material, a part of it will be reflected ($\Psi_r = a_r e^{i\vec{k}_r \cdot \vec{r}}$) and a part of it will be transmitted ($\Psi_t = a_t e^{i\vec{k}_t \cdot \vec{r}}$), as can be seen in Figure 2.2.a. At the interface, the waves and their derivatives are continuous; therefore:

$$\begin{aligned} a_i + a_r &= a_t \\ a_i \vec{k}_i + a_r \vec{k}_r &= a_t \vec{k}_t \end{aligned} \quad (2.23)$$

Then, considering $k = \|\vec{k}_i\| = \|\vec{k}_r\|$ and $nk = \|\vec{k}_t\|$ and taking in consideration the parallel component of the vector k , one can derive:

$$\cos(\alpha) = n \cdot \cos(\alpha') \quad (2.24)$$

where n is the refractive index and α and α' are the reflected and refracted angles counted from the sample surface plane. This relation is called Snell's law, and it bounds the incident and refractive angles. For the x-ray, the refractive index has the form:

$$n = 1 - \delta - i\beta \quad (2.25)$$

where:

$$\delta = \frac{r_e \rho_e \lambda^2}{2\pi}, \quad \beta = \frac{\mu \lambda}{4\pi} \quad (2.26)$$

r_e is the classical electron radius, ρ_e is the bulk electron density and μ is the absorption coefficient. This formula shows that the refractive index is lower in a material than in vacuum ($n = 1$). This means that there is an angle below which all the light is totally reflected. This angle can be derived as:

$$\alpha_c = \sqrt{2\delta} \quad (2.27)$$

so it is possible, knowing the critical angle α_c , to derive the bulk density of the material.

In order to derive an easy description of the reflected and transmitted beam intensity, it must be defined the amplitude of the transmitted and reflected wave as:

$$r = \frac{a_r}{a_i}, t = \frac{a_t}{a_i} \quad (2.28)$$

And using the equations 2.23 together with the Snell's law, it is possible to associate the incident angle and n with the reflectivity:

$$R(\alpha) = \left| \frac{\sin(\alpha) - \sqrt{n^2 - \cos^2(\alpha)}}{\sin(\alpha) + \sqrt{n^2 - \cos^2(\alpha)}} \right|^2 \quad (2.29)$$

and the transmissivity:

$$T(\alpha) = \left| \frac{2 \sin(\alpha)}{\sin(\alpha) + \sqrt{n^2 - \cos^2 \alpha}} \right|^2 \quad (2.30)$$

Those formulas are called Fresnel reflectivity and Fresnel transmissivity, respectively. Already from this simple description, it is possible to understand the main trend of the reflectivity (see Figure 2.2.b): until the critical angle, the reflectivity is 1, then there is a fast decrease until the $3q_c$; above that point, it follows an asymptotic behavior as q^{-4} . The transmitted intensity, instead, has a maximum at the α_c , then decreases with the increase of the angle until it reaches the value 1.

2.2.2 Derivation of the density profile

The vertical density profile is usually not a sharp interface, but (starting from a position above the layer and going down), it gradually increases to reach the bulk density. If the sample is made by layers, it can be represented by the slabs model. In the slabs model, each layer is characterized by a thickness, a density and the roughness of the top interface. The most common function to describe slabs is the error function. For each layer of number N_l , the sample is described with:

$$\rho(z) = \sum_{i=0}^{N_l} \left(\frac{\rho_{i+1} - \rho_i}{2} \right) \left(\operatorname{erf} \left(\frac{z - Z_i}{\sigma_i/\sqrt{2}} \right) + 1 \right) \quad (2.31)$$

where ρ_i is the electron density referred to layer i , and Z_i is the position of the layer. The value of σ_i is proportional to the "transition region" thickness. This presence of the transition region is caused by layer roughness, usually approximated by Gaussian distribution of electronic density in the out-of-plane direction. In the extreme case of $\sigma = 0$, the formula gives the step function describing the layer without roughness. The reflectivity can be calculated with different methods; some approaches are approximations; some others provide the analytical solution. For example, the kinematical approach, which does not take into account the multiple scattering, gives a solution that can be easily interpreted. This method is called Born approximation:

$$R(\vec{q}_z) = C \left| \frac{1}{q_z^4} \int_{-\infty}^{+\infty} \frac{d\rho(z)}{dz} e^{iq_z z} dz \right|^2 \quad (2.32)$$

where C is the scaling factor. This formula shows that the reflectivity is the Fourier transform of the derivative of the density profile as a function of z . Also, here it can be noticed that the reflectivity decreases with q^4 . E.g. if $C = 1$, the solution for a double interface would be:

$$R(\vec{q}_z) \propto \frac{1}{q^4} [\Delta\rho_1^2 e^{-q_z^2 \sigma_1^2} + \Delta\rho_2^2 e^{-q_z^2 \sigma_2^2} + 2\Delta\rho_1 \Delta\rho_2 e^{-q_z^2 \frac{\sigma_1^2 + \sigma_2^2}{2}} \cos(q_z [Z_1 - Z_2])] \quad (2.33)$$

ρ_n, σ_n and Z_n are the electron density, the standard deviation and the position of the slab respectively. In the first two addends of the equation, the effect of the roughness is to reduce the reflectivity to lower values. The third addend, however, takes into account the effect of the interference of the reflected waves between the two layers; this function is oscillatory. The resulting XRR curve has maxima and minima; these extremes are called Kiessig fringes. Already from the position of extremes, it is possible to estimate the thickness of the layers. Another method that will be presented here is the Parratt's formalism that gives an exact solution to the XRR trend. The main logic behind this method is that the electron density profile of the sample is divided into many different slabs. Every slab has a different electron density. The amplitude of the reflection coming from each slab is calculated in this way:

$$r_{j,j+1} = \frac{k_{z,j} - k_{z,j+1}}{k_{z,j} + k_{z,j+1}} \quad (2.34)$$

where

$$k_{z,j} = k_0 \sqrt{n_j^2 - \cos^2 \alpha_i} \quad (2.35)$$

once the $r_{j,j+1}$ is obtained, the amplitude of the total reflectivity curve can be recursively obtained as:

$$X_j = e^{-2ik_{z,j}z_j} \frac{r_{j,j+1} + X_{j+1}e^{2ik_{z,j+1}z_j}}{1 + r_{j,j+1}X_{j+1}e^{2ik_{z,j+1}z_j}} \quad (2.36)$$

at the end of the cycle, the reflectivity will be: $R(q_z) = |\sum X_j|^2$.

2.3 The synchrotron radiation

The synchrotron radiation quality can be described by the brilliance. The brilliance takes into account the flux, the divergence and the spectrum width of the photons as well as the dimension of the source. The brilliance is defined:

$$brilliance = \frac{n_photons}{second \cdot mrad^2 \cdot mm^2 \cdot 0.1\%BW} \quad (2.37)$$

where the $mrad^2$ measures the angular divergence, mm^2 the source area and $0.1\%BW$ is 0.1% of the spectrum width at the energy selected.

The characterization of the LMCat samples need a high brilliance, and a high energy x-ray source; the synchrotron provides both. High flux is needed because of the low scattering intensity of the graphene, which has a small atomic number and a small number of scattering atoms (layer of 1 atom thickness). The high energy is needed for two technical reasons; the first is that the reactor is filled with argon that absorbs the low energy photons. The second reason is that the angle accessible in the vertical direction for the x-ray is limited. At higher energy, the useful information for the XRR (like the minima and the layering peaks) is present at smaller angles. For a deeper knowledge of the synchrotron principles, the main books about the subject that were used to write this section are suggested[81, 87, 88].

2.3.1 The synchrotron

The synchrotron is a ring in which bunches of charged particles (usually electrons) circulate at constant energy and constant speed in a synchronized

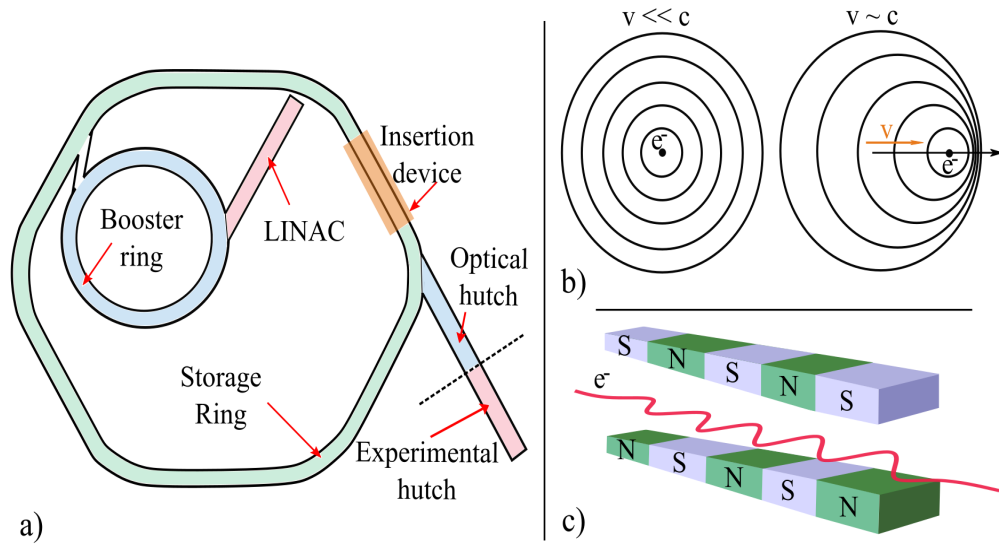


Figure 2.3: a) Sketch of the main segment of the synchrotron. The electrons are generated in the LINAC where they are initially accelerated. Then, in the booster, they reach the final speed. In the storage ring, the electrons are not further accelerated, here the insertion devices and bending magnets (not shown) are present to create x-ray photons. The beamline is formed by the optical hutch and by one or more experimental hutches. b) On the left, electromagnetic waves produced by a not relativistic electron. On the right, electromagnetic waves produced by an electron moving at $v \sim c$, the direction of the movement is shown by the orange arrows. On the direction of the movement, the wave has a lower wavelength due to the Doppler effect. c) Path of the electrons inside an undulator.

way. The electrons are produced with an electron gun and then are accelerated with a linear accelerator (the LINAC) at ~ 100 MeV. Afterwards, they are injected in the booster ring where the electrons increase speed to the final energy (6 GeV for ESRF) with a radiofrequency voltage source. In the last step, the particles are introduced in the storage ring, where they do not further increase their energy. The shape of the storage ring can be roughly imagined as an polygon more than a circle; the beam is produced in the corners by the bending magnets and in the straight parts by the wigglers or the undulators. A beamline is located at every x-ray source, and it usually contains an optical hutch and one or more experimental hutches. The first one is to modulate the intensity, the size, and the wavelength of the beam; the second one is where the experiment is performed. A sketch of the synchrotron design is showed in Figure 2.3.a. One of the significant advantages of the synchrotron is to guarantee high flux photons with tunable energy. The lifetime of electrons in the storage ring is limited due to the collisions with residual gas molecules and radiation losses. Radiofrequency cavities are then placed in specific points of the rings to narrow the energy difference among the electrons.

2.3.2 The beam production

As shown in Figure 2.3.b, an electron moving at a non-relativistic speed produces a uniform isotropic dipolar radiation. When the electron approaches the speed of light, its speed is comparable to the one of the radiation produced. In the laboratory frame of references, the radiation is strongly focused in the direction of the movement due to the Doppler effect. The electron energy, in units of the rest mass energy, is: $\gamma = \frac{\varepsilon_e}{mc^2}$, where ε_e is the energy of the electron and depend on the synchrotron.

The x-ray photons used in this work were coming from undulators. The undulators (shown in Figure 2.3.c) are composed of two series of arrays of magnets N-S and S-N. The generated magnetic field makes the electron beam oscillate. Every oscillation produces radiation; the magnetic array periodicity λ_u is designed in such a way that every oscillation is in phase with the next one, significantly increasing the intensity. With respect to other synchrotron sources, like bending magnets or wigglers, the undulator guarantees a lower divergence, higher brilliance, and a narrow radiation wavelength dispersion. The wavelength of the beam depends on the intensity of the magnetic field B_0 that the electrons experience. B_0 can be tuned moving the gap between

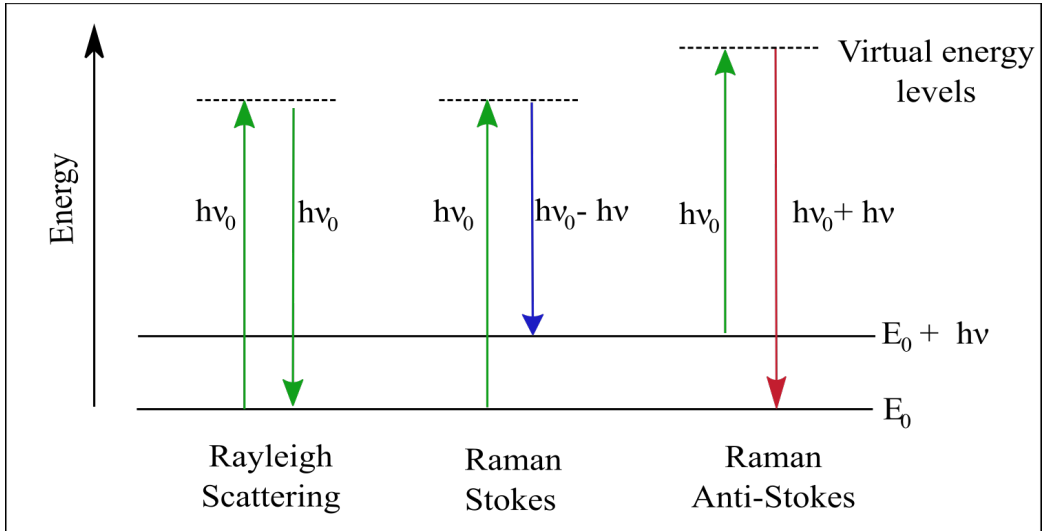


Figure 2.4: Sketch of the energetic levels of the phenomena occurring in a Raman experiment. In the Rayleigh scattering, the electron absorbs the energy of the photon, and it reaches a virtual energetic level. Then it relaxes and emits a photon with the same energy of the absorbed one. The Raman Stokes, the electron reaches an energetic vibrational level after the relaxation from the virtual one. In the anti-Stokes, the electron is starting from a higher energetic level, and after the excitation on a virtual level, it relaxes on the ground state. The Stokes signal has a lower energy respect to the incident photon, the anti-Stokes one has a higher one.

the two arrays of magnets.

2.4 Raman spectroscopy

2.4.1 The Raman effect

Raman spectroscopy is a standard technique in many fields. It is based on the Raman scattering effect, i.e., on the inelastic scattering of light (usually visible) by matter. It is beneficial to characterize graphene because it is fast, relatively cheap, and not destructive. With the Raman spectroscopy, the number of defects, number of layers, and strain can be easily determined. The Raman effect can be described with the classical or with the quantum

approach. In the classical theory, the Raman effect is explained using the concept of polarizability. When light interacts with atoms, their electrons start to oscillate. These oscillations create dipoles that produce light at different frequencies. The dipole induced by the molecule can be calculated as:

$$\vec{p} = \alpha \cdot \vec{E} \quad (2.38)$$

where E is the electric fields of the electromagnetic wave, and α is the polarizability. α is a value that indicates the tendency of a molecule to be polarized, and it is a function of the nuclear coordinates as well as the molecular and vibrational frequencies. Applying some calculations, with the hypothesis that α components do a small shift on the position of the equilibrium and that the oscillations are harmonic, it is possible to write the dipole as:

$$\vec{p} = \vec{p}(\omega) + \vec{p}(\omega - \omega_k) + \vec{p}(\omega + \omega_k) \quad (2.39)$$

where ω is the frequency of the ray and ω_k is the molecular frequency. This formula is important because it shows the nature of the radiations that can be seen in the Raman spectroscopy. The dipole present three components with different frequencies:

- $\vec{p}(\omega)$ the dipoles create an electromagnetic wave with the same frequency. This is called Rayleigh radiation
- $\vec{p}(\omega - \omega_k)$ in this case, the frequency $(\omega - \omega_k)$ is lower respect to the incident radiation. This radiation is called Raman Stokes.
- $\vec{p}(\omega + \omega_k)$ in this case, the frequency $(\omega + \omega_k)$ is higher respect to the incident radiation. This radiation is called Raman anti-Stokes.

Another consideration is that the Raman scattering can be observed exclusively if the α_k frequency associated with ω_k is different from 0. This is verified only if at least one component of the polarizability has a derivative on the coordinate of oscillation different from 0. The Raman active modes are not exclusively the domain of molecules but also for crystals; the Raman active mode in graphene will be shown in Section 2.4.2.

In the '30s, a new approach for understanding the Raman effect took advantage of the quantum mechanics theory that was growing in those years. In quantum mechanics, atoms and molecules have discrete energetic levels.

Absorption can only be done between these discrete levels. For this reason, also the energy emitted is quantized. The process consists of two steps: in the first one, the incident photon with a frequency of ν_0 is absorbed by the vibrational states. Then the molecules relax to lower energetic levels. If the final vibrational level is higher than the starting one, the radiation emitted is called Stokes scattering and the energy would be $h(\nu_0 - \nu)$, conversely, if the energy is lower, it is called anti-Stokes and the photon energy associated is $h(\nu_0 + \nu)$. If the energy is the same, it is the case of Rayleigh scattering. The graphical representation of this is shown in Figure 2.4

The final consideration is that the Raman signal is extremely weak with respect to the Rayleigh one and it is not always easy to detect. Furthermore, the molecules at room temperature usually have more electrons in the lower state with respect to the excited one, thus, the Stokes transition is statistically more frequent respect to anti-Stokes and so it is more intense. The information about the Raman scattering written below were taken from the John R. Ferraro's book[89].

2.4.2 Raman on graphene

As discussed before, the crystals do not have quantized vibrational levels, but the lattice vibrations are almost continuous. Figure 2.5 shows the phonon dispersion relations of graphene. The graphene has six phonon dispersion bands, three acoustic (A), and three optics (O). The vibration of two acoustic and two optic branches are in-plane (i), the others are out-of-plane (o). Furthermore, the phonon modes are classified as longitudinal (L) or transverse (T) according to vibrations parallel with or perpendicular to the A-B carbon-carbon directions. The active phonons in the graphene are coming from the iLO and iT0.

The main peaks for the Raman spectra are shown in Figure 2.5.a,b,c and described below:

- **G peak:** This peak is observable at $\sim 1580 \text{ cm}^{-1}$, and it is specific of the material with hybridized sp^2 carbon. The phonon involved in this process is the one in the degeneracy of iT0 and iLO at the Γ point. In this process, the photon of the laser promotes an electron from the valence band to the conduction band, and it creates an electron-hole pair. The promoted electron is inelastically scattered by the phonon, and it recombines with the hole in the valence band. In the relaxation

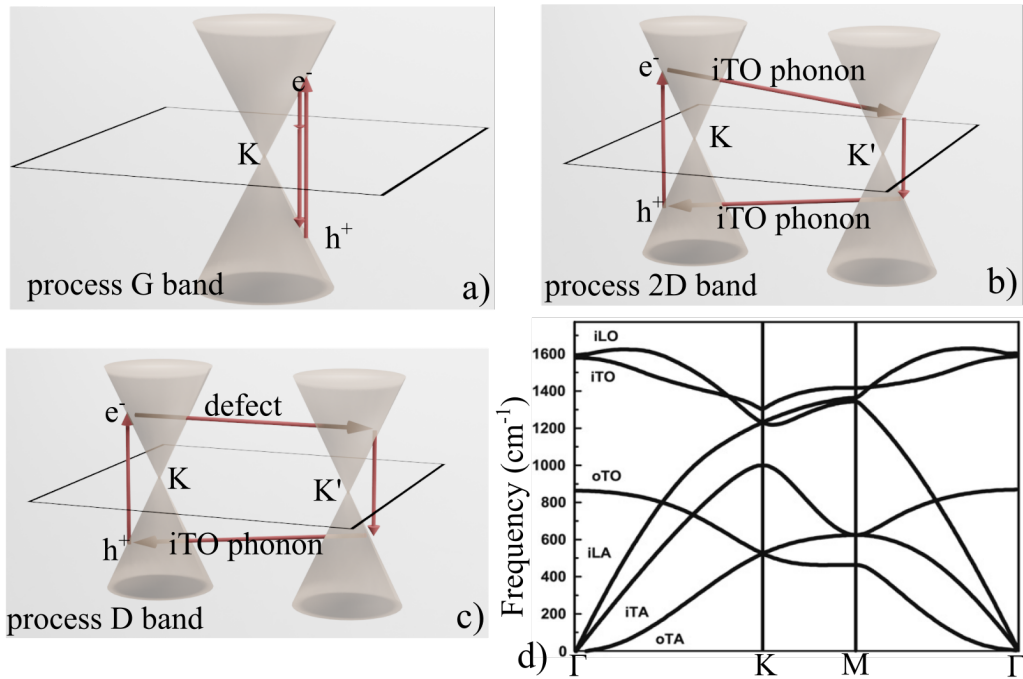


Figure 2.5: a) The G band process: the electron e^- is promoted by the photon of the laser, and it produces a hole h^+ . The electron then scatters with a G band phonon, and it partially loses energy. During the last relaxation process, it creates a Raman photon. b) The 2D band process: the electron is promoted by the photon of the laser of the Raman instrument, then it scatters with an iTO phonon, and it reaches the neighbor Dirac cone K' . Then it relaxes in the valence band of K' . In the last step, it scatters again with a phonon iTO, and it comes back to the same energetic level. c) The D band process: the process is similar to the 2D one, however, one scattering with the phonon is substituted with a scattering with the defect. d) Dispersion bands of the graphene. The image was taken from Malard *et al.*[90].

process, the Raman photon is generated.

- **2D peak:** This peak is observable at $\sim 2700 \text{ cm}^{-1}$. In this process, a photon promotes an electron to a conduction band, and it generates an electron-hole pair around the K point. Then, an iTO phonon inelastically scatters it around the K' point. The law of conservation of the momentum imposes that the electron must come back to the K point before it recombines with the hole. So the electron is back-scattered by an iTO phonon to K , and it relaxes to the conduction band. The difference between incoming and outgoing photons is twice the phonon energy. This peak is very sensitive to the number of layers of the material.
- **D peak:** This peak is observable at $\sim 1350 \text{ cm}^{-1}$. The scattering process is similar to the one of the 2D; however, one inelastic scattering with iTO phonon is replaced with an elastic scattering with a defect. For this reason, the peak is situated at half the 2D peak energy. This peak is important because it gives information on the presence of defects in the crystal; if the defects are numerous, this process is more favorable, and the Raman peak associated will be more intense. *Vice versa*, for defect-free graphene, the D peak is absent.

The ratio between the intensity of these peaks is used to characterize the graphene. For example, the monolayer graphene probed on copper at room temperature with a $\lambda = 405 \text{ nm}$ laser has $I_{2D}/I_G > 1$, and a defect free graphene has $I_D/I_G \ll 1$. The theory of the Raman scattering on graphene can be found in articles [90, 91, 92] as well in books[93, 94].

2.5 Radiation mode optical microscopy

Optical microscopy is the most classical and known technique to study objects of sub-millimeter size. The purpose of the optical microscope is to deliver magnified images of the sample and to show details that cannot be seen with naked eyes. The classical microscope is composed of an objective, a set of lenses, and a detector. The light coming from the sample has a different origin; it can be:

- reflected from a light source. In this case, it is called reflection mode optical microscopy

- generated from the sample. In this case, it is called radiation mode optical microscopy

It turns out that the radiation mode is more suitable for detecting graphene at high temperature[95]. The light emitted by the matter, in fact, depends on the temperature. The black body radiation follows the Plank's law; most of the objects, however, emit less than the theoretical value. The variable that measures the ability of an object to emit light is the emissivity, and it is defined as:

$$\epsilon = \frac{\textit{radiant_energy_emitted}}{\textit{radiant_energy_of_blackbody}} \quad (2.40)$$

In the LMCat project, the graphene is floating on liquid copper. The temperature of the copper was just above the melting point (1400 K). At this temperature, the emissivity of copper is 0.143[96]. The graphene absorbs a small portion of the light ($\sim 2.5\%$ [97]) coming from the Cu below, but radiate light itself due to the temperature, with an emissivity of 0.016[98]. The total emissivity of graphene on liquid copper is: $0.143 \cdot (1 - 0.025) + 0.016 = 0.155$. The contrast between the liquid background and the single layer of carbon atoms is $\sim 8\%$, and it scales linearly with the number of layers.

Chapter 3

Experimental setup

3.1 The LMCat project

The graphene is a promising material in many technological fields; however, it still has problems entering the market, and the industries producing it are very often selling to the research centers. One of the main issues is related to the production and to the separation processes[99]. Until now, there are no efficient ways to produce high-quality defect-free graphene at a competitive price.

One method of production is the CVD method described in Chapter 1. This technique allows a self-limiting process and a maximum material size that depends exclusively on the extension of the catalytic surface. Once the graphene is produced, it must be separated from the catalyst; this is usually done dissolving the metal in acids. This process, however, is costly inefficient, not eco-friendly, and it represents a significant bottleneck for the entrance in the market.

The advantages of the liquid metal catalyst on the solid one were described in Chapter 1, here summarized in:

- Atomic smoothness of the surface
- Anisotropy of the surface
- Auto-alignment of the flakes

In addition, the adhesion force of the graphene on solid catalysts is usually higher respect to liquid, and therefore it may be possible to extract the

graphene directly from the surface. For example, adhesion force for solid Cu is 0.72 J/m^2 [100] while for liquid Cu is 0.3 J/m^2 [101]. The force per unit length to separate the graphene from the liquid would be then 0.72 N/m and 0.3 N/m respectively. The strength of the polycrystalline graphene is $30\text{-}33 \text{ N/m}$ [102]. On the liquid metals, less force must be applied, therefore less stress on the 2D material.

The use of a liquid metal catalyst for the formation of the graphene is not new, and many groups have studied it. In the experiments reported however, the samples were cooled down after the growth, and the metal was re-solidified, changing the surface significantly. A clear knowledge of the dynamic of the growth on the liquid is not revealed yet, and it requires a characterization on the sample during the formation of the 2D layer.

In this scenario, the LMCat project aims to fill this gap, applying techniques that allow to measure *in situ* the growth. The techniques that can be used inside a controlled environment of a reactor and that were chosen for this project are: the optical microscope, the x-ray scattering techniques, and the Raman spectroscopy. The optical microscope gives an insight into the formation of the graphene at the macroscopic level; it is possible to know the number of flakes, the number of impurities particles on the surface, and the interaction between flakes. The x-ray and the Raman techniques give information at the atomic level, like the quality of the graphene formed, as well as the number of layers, lattice parameter, etc.

The reactor that allows these measurements were projected and created in the LPM laboratory with the collaboration of Leiden University and all partners of the LMCat project, and it is described in Section 3.2.1.

3.2 LMCat equipments

3.2.1 The reactor & gas system

The reactor has a cylindrical shape with a 150 mm inner diameter and 46 mm height; the sizes were chosen to be compatible with all existing liquid diffractometers. The lateral section of the reactor is shown in Figure 3.1.a: in the center of the reactor, there is the sample and the heater. The heater is made of pyrolytic graphite covered by boron-nitride (BN), and the sample holder is placed directly on it. The resistance of the BN heater is around 12

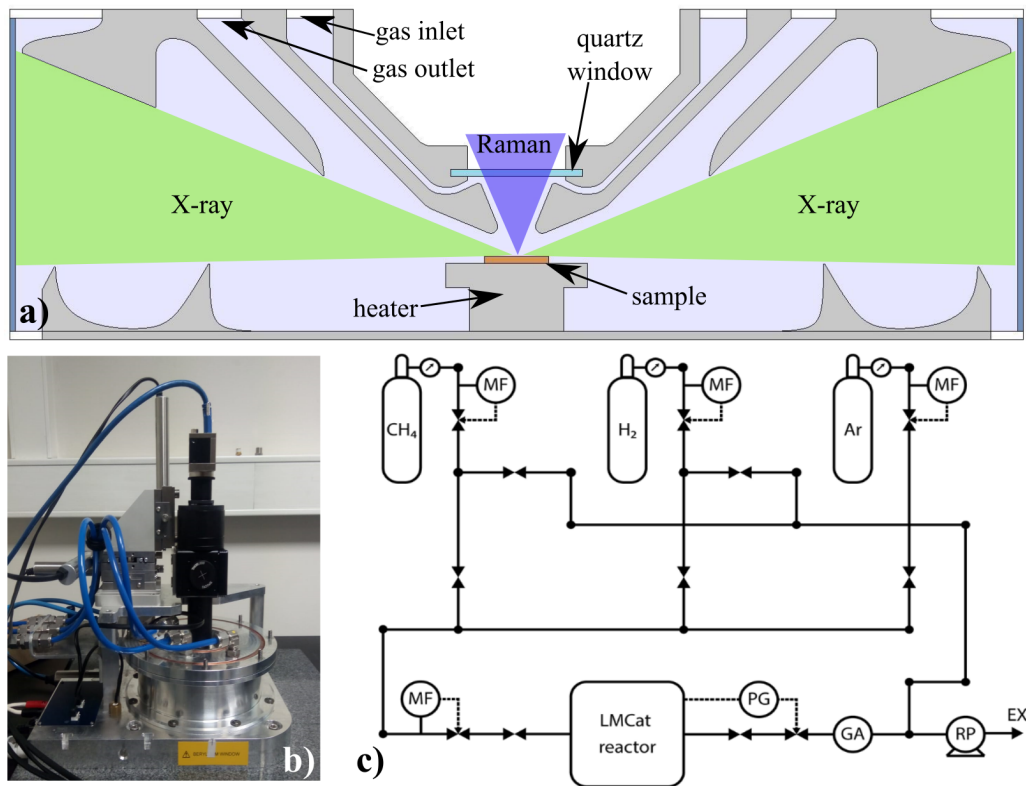


Figure 3.1: a) lateral section of the reactor; the heater is in the center of the reactor, and the sample holder is laid on it. The external walls are made of Be, transparent to x-ray, while the quartz window is set at 12.7 mm on the top of the sample. The green cones represent the angular space allowed for the x-ray (from -1° to 22°); while the purple one is the one for the Raman spectroscopy or for the optical microscope. The gases are passing through the inlet (in Figure), and it is conveyed on the quartz window. The flow is then forced to go on the surface of the sample; the copper vapor in this way are deviated towards the lateral side of the reactor. A system of flanges, however, (gray in Figure) break the vortex and favor the deposition of the Cu before the Be window. b) The picture of the reactor with the optical microscope in the laboratory of the ESRF. c) Scheme of the gas system.

Ω ; the power is delivered by a power supplier controlled by a computer. The lateral wall of the cylinder is made of beryllium to allow the passage of the x-ray, while the bottom plate and the lid are made of aluminum. Just above the sample surface, there is a quartz window. In order to change the sample, the upper part of the reactor can be unscrewed and removed. Two columns allow the fixing of the microscope as shown in Figure 3.1.b. As mentioned in the previous chapter, the reactor allows the characterization with the Raman/optical microscope and the x-rays; as can be noticed in Figure 3.1.a, there are two sets of cones representing the angular space that the techniques can use. The green cones, for example, represent the angle in which the x-ray scattering techniques are allowed, and it goes from -1° to $+22^\circ$. The azimuthal access (not illustrated in the Figure) is limited by the two columns that support the Raman probe. The two open azimuthal angles are 203° and 84° . The blue cone is for the Raman or the optical microscope. Those techniques need vertical access to the sample; for this reason, a quartz window is placed at 12.7 mm from the surface of the molten metal. The focal length of the objective needs to be higher than this value, which is relatively high for normal Raman (usually ~ 1 mm). This fact leads to a lower numerical aperture and a lower collected signal; however, this distance is necessary to reduce the heating of the window. The heating of the chamber, together with the high evaporation rate of the liquid copper (0.4 mm/hr in vacuum) were serious issues that were faced while the reactor was designed. Both the suppression of the evaporation and the cooling of the window were achieved with a controlled gas flow. The gases are coming from the inlet, as shown in Figure 3.1.a, and they are conveyed to the Raman window. Then, they flow to the bottom towards the sample. In this way, the evaporated atoms of copper from the sample collide with the atoms of the gases, and they are deflected. The minimal flux that guarantees protection of the window was calculated as 90 sccm. The flux of vapor is then altered by the series of flanges on the upper and lower part of the reactor. The result is that the copper is deposited mostly on the flanges, and the beryllium window is protected. Another inlet is set for safety, and it flows gases parallel to the beryllium window; this system, however, has never been used. A system of cooling is needed to maintain the reactor operational for a long time. The temperature of the chamber during an experiment was simulated with the COMSOL program; the calculation shows that the temperature of the quartz windows is $\sim 60^\circ\text{C}$ above the RT, while the one of the Be walls is

just 10°C higher[103]. The chamber is always monitored with two thermocouples (on the top and on the bottom plate), in order to check overheating problems.

The scheme of the gas system is shown in Figure 3.1.c. The gases used in this work were:

- **Argon** : it was chosen as a carrier gas because it is inert, and it has a high atomic mass. The high atomic mass (and therefore the high momentum) is ideal to efficiently deflect the Cu vapor atoms.
- **Hydrogen** : it is needed to control the equilibrium of the reaction of dissociation of methane and the formation of the graphene. It is also essential to etch the graphene if new growth is needed.
- **Methane** : it is the carbon precursor for the formation of the graphene.

The gases are conveyed from the bottles to the gas flow controller in a mobile rack. In the rack, the gases are mixed and delivered to the reactor. A PID controller connected to a valve regulates the pressure in the chamber. The parameter of the flow (sccm of gases flown, the total pressure in the chamber, opening, and closure of the valves) can be set by a computer. The flow of the gas can be stopped by an electromagnetic valve; there are three valves just after the connection from the bottle to the gas flow controller. The valve of the methane gas is particularly important because it was used to control the initial partial pressure of the carbon precursor, and its role is described in more detail in Chapter 4.

3.2.2 Sample & sample holder

The liquid copper needs a proper support that must:

- be chemically inert
- have a small wetting angle with the liquid

The sample holder must be chemically inert, because every impurity on the surface of the liquid can act as a nucleation center for the formation of graphene, altering the catalytic properties of the bare liquid copper with unknown factors. The small wetting angle is needed for the diffraction experiments because a curved surface leads to a spreading of the beam. The

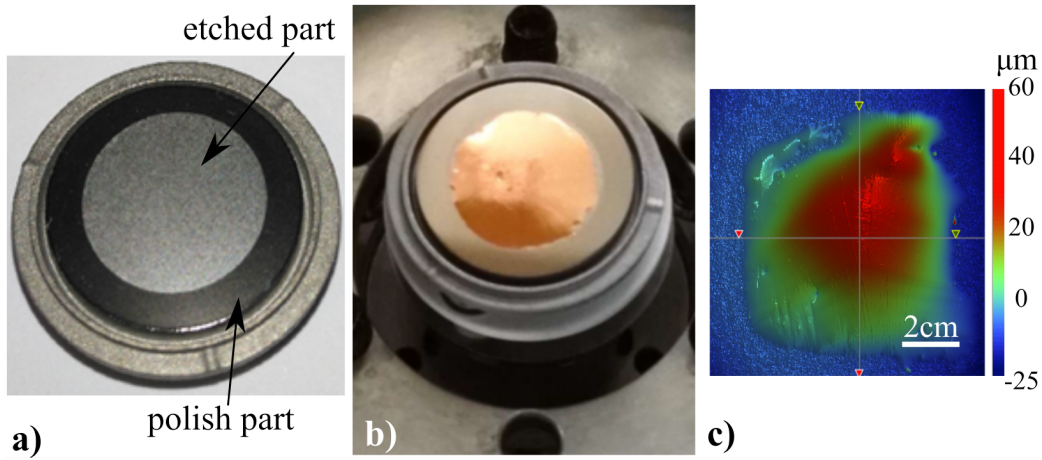


Figure 3.2: a) Sample holder before the melting of the Cu. It is possible to appreciate the rough etched center and the polish side. b) Picture of the sample holder with a layer of re-solidified Cu. c) Profilometry image of the sample holder with the re-solidified Cu.

tungsten is the best refractory material among the ones tested; however, the wetting angle between liquid Cu and W is too high for the diffraction experiments ($\sim 26^\circ$). In order to reduce the curvature of the liquid and to confine it (to avoid leaks), the surface of the W was modified. Following the Wenzel model, the increase of the the substrate roughness decreases the contact angle of the wetting liquid[104]. For this reason, the external part of the surface of the W was polished in the polishing lab, while the center was etched with a solution 1:3 of $\text{H}_2\text{O}_2:\text{NH}_3$. Figure 3.2.a and 3.2.b show the sample holder before and after the melting of the copper foils respectively. The *ex situ* profilometry image (Figure 3.2.c) shows a wetting angle of 1° , while from the spreading of the x-ray beam, the wetting angle of copper was calculated around $\sim 1.2^\circ$.

3.2.3 Raman & Optical microscope

3.2.3.1 The Raman spectrometer

The Raman spectrometer is a custom made instrument purchased from the Renishaw company. It works with a solid-state laser source with a $\lambda = 405$ nm and 30 mW output power. The choice of this particular wavelength

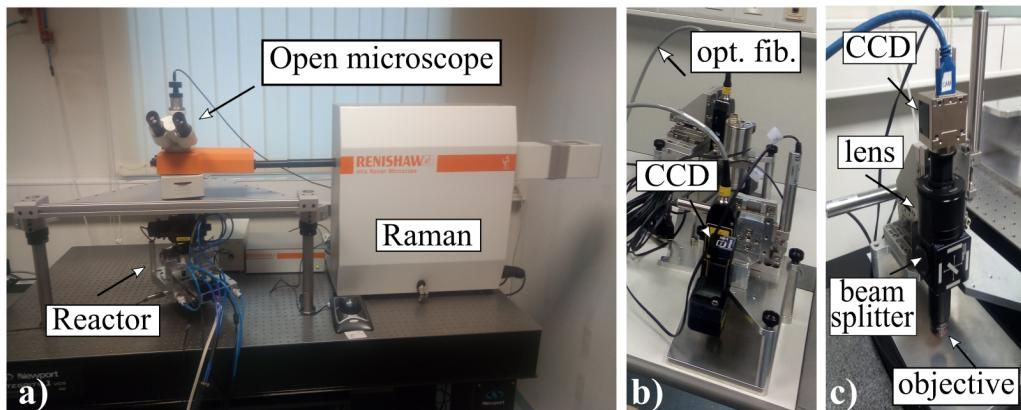


Figure 3.3: a) Picture of the Raman with the open microscope geometry b) Picture of the Raman probe c) Picture of the optical microscope.

(instead of the more common $\lambda = 514 \text{ nm}$) was made to measure as far as possible from the peak of emissivity of the black body radiation of the Cu. The Raman spectrometer can work in two modes:

- **Open microscope geometry:** the Figure 3.3.a shows the open microscope configuration. The laser (inside the white box) passes through the empty black tube towards the microscope. Then it deviates downwards on the sample in the reactor. This configuration can be used only in the laboratory and cannot be applied to the experiments in the beamline. The most significant advantage concerning the other design is that the signal of the Raman shift is 300 times more intense.
- **Movable probe geometry:** the laser is conveyed to the fiber optic to reach the Raman probe. The probe is attached to a frame as shown in Figure 3.3.b. The upper part can be dismantled and fixed to the reactor. The three actuators, monitored by a computer, control the position of the probe. The probe is the perfect tool to acquire measurements during the beamtimes due to its handling and high flexibility. The main drawback is that the signal is weaker with respect to the previous configuration. A portion of the photons, in fact, is lost both in the junctions of the fiber optic and in the fiber optic itself. The photons loss, due to the fiber optic, decreases the efficiency of the Raman for two reasons: first of all, the laser power is lower because

it is partially absorbed before reaching the sample; secondly, the Raman shift produced by the sample is partially lost before reaching the detector.

The computer controls both the probes and the open microscope. The CCD camera records the images of the surface of the sample. The optical microscope was not thought to be a characterization technique for this project. From the first movie recorded by the camera of the Raman spectrometer, however, it was suddenly evident the importance of this technique. For this reason, a microscope was built to optimize this measurement, and it is described in the next Section.

3.2.3.2 The optical microscope

The optical microscope is an infinity optical system; the picture of the set-up is shown in Figure 3.3.c. The set-up can be divided into four elements:

1. The objective lens
2. The tube lens
3. C-MOS camera
4. The microscope holder

The objective lenses *LMPLFLN* were bought from Olympus, and they are the same as the Raman. The magnifications available in the lab are x5, x10, x20, or x50. The 5x magnification allows to see a more significant portion of the sample surface, and it was mostly used in this thesis work. This lens has a focal length of 22.5 mm and a numerical aperture of 0.13.

The lens is fixed on a tube and on a box. This box allows connecting a beam splitter and eventually attaching a light to use reflection mode optical microscopy.

At the opposite side of the cube, respect to the lens, the tube lens is fixed. The tube lens *TTL180-A* was purchased from Thorlabs, and it has a focal length of 180 mm. The collected photons are then conveyed to the C-MOS camera *acA4112-30um* Basler of 12.3 Mpix. The dimension of the CCD is 14.1 x 10.3 mm with a pixel size of 3.45x3.45 μm .

The microscope holder is the one of the Raman probe re-adapted for this instrument. It is made of a translation plate, connected by three motors



Figure 3.4: The picture of the ID10 beamline with the rotation angles displayed. The horizontal angle called δ and the vertical is called γ . ω is the rotation angle around the \hat{z} axis.

(x,y,z) and controlled by a computer. This stage is fixed on a metallic plate that can be assembled to the reactor.

3.3 Liquid surface diffractometer

3.3.1 General geometry of the liquid surface diffractometers

The liquid surface diffractometer, like a surface diffractometer for solid, allows to easily measuring a significant portion of the reciprocal space. The only difference with respect to the solid counterpart is that the sample cannot be tilted; for this reason, the beam itself must deviate downward with a double crystal deflector (DCD). The DCD is a set of two crystals; the first one deviates the ray towards a second one and the latter towards the sample. This two-crystal assembly can rotate rigidly around the axis defined by the incoming beam direction. Changing the rotation angle allows selecting the angle between the sample plane and the beam.

As shown in Figure 2.1.b, the origin of the axis $\hat{x}, \hat{y}, \hat{z}$ is set in the center of the sample surface; the wavevector of the beam coming from the optical hutch is usually parallel to \hat{x} . Then it is deflected by the DCD towards the

surface of the sample. The wavevector associated with the incident beam would be: $\vec{k}_i = k_0[\hat{x}\cos\alpha - \hat{z}\sin\alpha]$ where $k_0 = \frac{2\pi}{\lambda}$. The diffractometer allows to move the sample in all the directions $(\hat{x}, \hat{y}, \hat{z})$ and to rotate it around the \hat{z} axis of and angle ω . This last movement is not particularly necessary to study the liquid surface, but it was used for the alignment of the graphene grown on the surface. Many diffractometers also allow the rotations around \hat{x} and \hat{y} for the alignment. After interacting with the matter, the beam is then diffracted; if the spherical coordinates are used, δ is the longitudinal angle, and γ is the latitudinal one. The scattering wave vector is:

$$\vec{k}_r = k_0[\hat{x}\cos\gamma\cos\delta + \hat{y}\cos\gamma\sin\delta + \hat{z}\sin\gamma] \quad (3.1)$$

with a total scattering vector transfer of:

$$\vec{q} = \vec{k}_r - \vec{k}_i = k_0[\hat{x}(\cos\gamma\cos\delta - \cos\alpha) + \hat{y}\cos\gamma\sin\delta + \hat{z}(\sin\gamma - \sin\alpha)] \quad (3.2)$$

The detector is fixed on a movable arm that can rotate around δ and γ . Figure 3.4 shows the angles on the diffractometer of the ID10 beamline at ESRF. The choice of the angles depends on the kind of experiment:

- for a GIXD experiment $\alpha < \alpha_c$, $\delta \geq 0$ and $\gamma \geq 0$,
- for an XRR experiment $\alpha = \gamma$, $\delta = 0$.

In the special case of XRR, Formula 3.2 can be simplified to:

$$\vec{q} = 2k_0\sin(\alpha)\hat{z} \quad (3.3)$$

The software controlling the movements of the motors have different syntax depending on the synchrotron. The scans, however, work with the same basic idea. Four parameters must be defined: the motor to be moved, the angular range, the number of points, and the acquisition time. The output is (if a 2D detector is used) a series of images.

3.3.2 ID10B beamline

The ID10B beamline is designed to do surface diffraction on solid and on liquid. The beam is generated by three undulator segments in series, giving an energy range between 7 keV to 30 keV. The beam is passing through the optical hutch in which a series of monochromators and mirrors are necessary

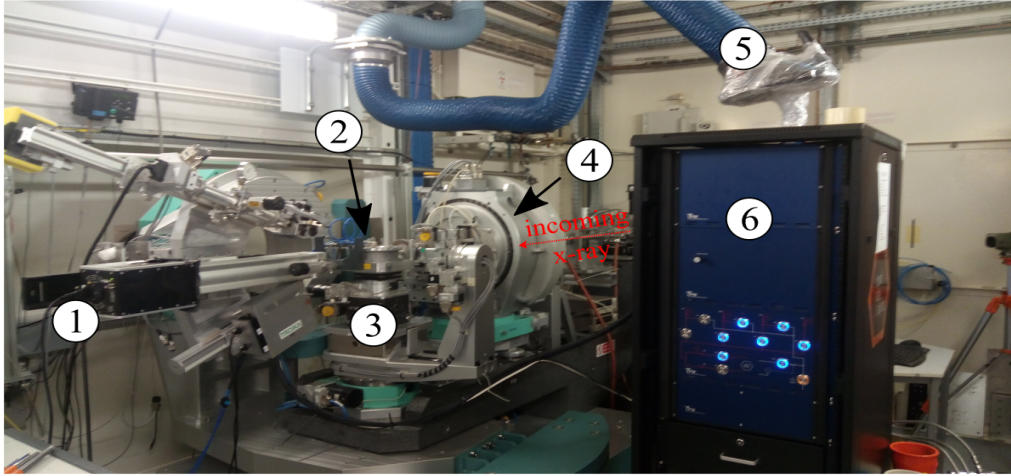


Figure 3.5: The Id10 beamline with the LMCat set-up. (1) The *MAXIPIX* detector, (2) The reactor (3) the $\hat{x}, \hat{y}, \hat{z}$ stage (4) the double crystal deflector (5) the extraction of the gases (6) The rack of the gases.

to select the right wavelength and to remove harmonics.

In the experimental hutch (Figure 3.5), a DCD is located before the diffractometer. The beam is deviated downwards using the reflection coming from Si(111) and Si(220) crystals. The wide distance between the deflector and the sample (~ 1 m) allows to fit the LMCat reactor easily on the diffractometer. The sample is located on a vertical stage; this stage allows movement and rotation around \hat{x}, \hat{y} and \hat{z} , and it is essential for the alignment of the sample inside the reactor. In the arm of the diffractometer, a 2D detector *MAXIPIX* is fixed.

The beam produced has a flux of the order of 10^{12} on the detector, a beam size that can be tuned to $< 0.03 \times 0.1$ mm (HxV) with focusing and an energy resolution of 10^{-4} .

3.3.3 Other surface diffraction beamlines

The results that are shown in this thesis work were also obtained in other beamlines in different synchrotrons in Europe. The principal characteristics and differences of the beamlines used in this work are shown in Table 3.1. All the x-ray sources were coming from undulators. The beamsizes and the energy of the electrons are important parameters. A synchrotron with high

Beamline	Synchrotron - e ⁻ energy	DCD	$\Delta E/E$	Beamsize (HxV)	Detector
ID10	ESRF - 6 GeV	YES	10^4	30x100 μm	MAXIPIX
ID03	ESRF - 6 GeV	NO	10^4	35 x 30 μm	MAXIPIX
P08	PETRA III - 6 GeV	YES	10^5	200x40 μm	EIGER
I07	DIAMOND - 3 GeV	YES	10^4	300 x 100 μm	Pilatus
Sirius	SOLEIL - 2.75 GeV	NO	10^4	2000x150 μm	Pilatus

Table 3.1: The parameters of the beamlines where the experiments were done are exposed.

energy produces a pink beam with a wider portion of high energy photon respect to a low energy synchrotron (using the same insertion device). The ideal photon energy for this experiment is relatively high (~ 20 keV). So higher electrons energy means a higher flux of energetic photons. It is also favorable a lower beamsizes because the flux per unit area becomes higher, and the intensity of the scattered signal increases. For these reasons, in some beamlines, it was easy to detect until the third order of 2DROD of the graphene, while in others, it was difficult to see the first one. If the beamline did not present a DCD, the reactor was tilted to reach the desired incidence angle. The adhesion force acting on the thin film of liquid, in fact, prevents the modification of the surface shape due to gravity.

Chapter 4

Growth of graphene on liquid copper

4.1 Introduction

In this chapter, the results of the growth of graphene on liquid copper are presented. The role of the radiation mode optical microscope (RMOM) had paramount importance because it allowed us to observe the surface of the sample in real-time. In this way, it was possible to study the kinetics of the growth and to have information on the morphology of the flake. Furthermore, the real-time monitoring was extremely useful because it helped to tune the growth, changing the partial pressure, and the flow of the gases.

As described in Section 3.2.1, the gases fluxed in the reactor are Ar, H₂, and CH₄. After many attempts to grow the monolayer graphene, the gas parameters were optimized for flux around 207 sccm of Ar, 10 sccm H₂, 0.14 sccm of CH₄, with a total pressure of 200 mbar. The partial pressure of Ar, H₂, and CH₄ are respectively 182.28 mbar, 17.6 mbar, and 0.12 mbar, with a $p[\text{H}_2]/p[\text{CH}_4]=146.7$.

All the growths described below were done at a few degrees above the melting point (~ 1400 K). The melting of Cu, which was possible to observe with the RMOM, allowed a precise calibration of the temperature.

The metal used was ultra-pure copper foils purchased from *Advent Research Materials* company (99.9976 % purity). The foils were cut and placed above the W sample holder. The copper foils were annealed in 100 sccm Ar and 10 sccm H₂ for 30 min at 1.05 bar in order to remove the oxide layer that

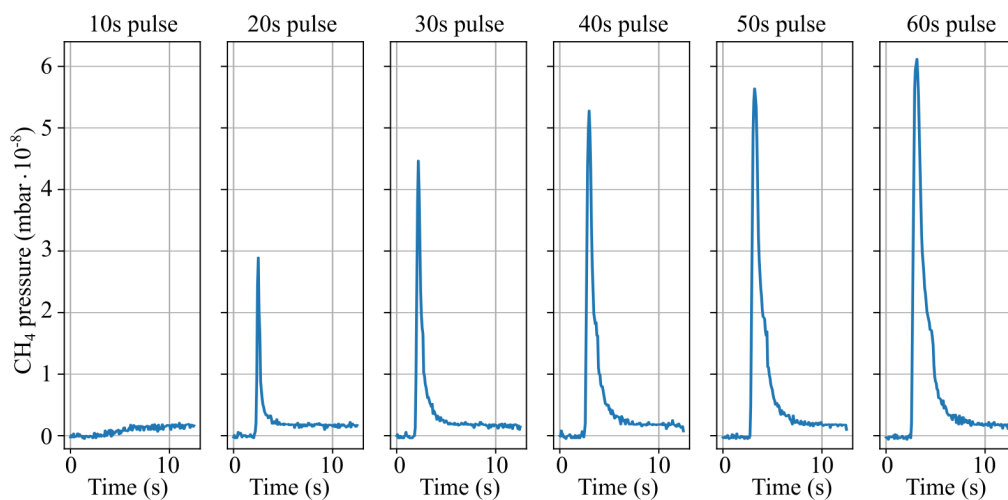


Figure 4.1: Plot of CH_4 partial pressure vs. time with a different waiting time of the pulse. The mass spectrometer was connected to the exhaust line of the gas of the reactor. The value shown are the CH_4 pressure in the reactor. The gas flow was: Ar 207 sccm, H_2 7 sccm and CH_4 0.14 sccm. The total pressure in the reactor was 200 mbar.

covers the surface, and then they were melted. Usually, on the molten copper surface, some carbon impurity particles are floating; in order to remove them, the molten film was exposed to 100 sccm Ar and 10 sccm H_2 for 1 or 2 hours at 200 mbar. This process significantly reduces the number of particles. Their role is essential for the growth of graphene because they trigger the nucleation, and it is described in detail in Section 4.3. The nucleation density could be controlled by regulating the concentration of CH_4 at the beginning of the growth. As described in Section 3.2.1, an electromagnetic valve could close or open the CH_4 line. When all gas valves were open, there was a steady-state flow of gas mixture with a constant concentration of constituents. However, if the flow of methane was set before the opening of the valve, an over-pressure was created in the CH_4 line. Once the valve was open, the gas was released, and the sample was exposed to the temporally higher concentration of the precursor gas, which initiates the nucleation of graphene flakes. Subsequently, to sustain their steady growth rate, the CH_4 pressure was swiftly decreased to the predetermined set-point value, and the constant flow of gas mixture is maintained.

In this work, the growth just described is referred to as "pulsed growth". The

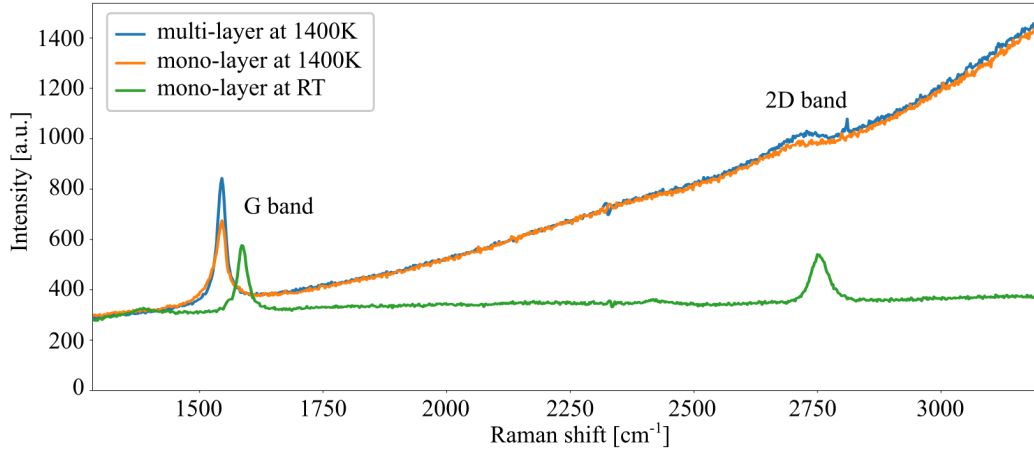


Figure 4.2: Raman spectra of multi-layer graphene on liquid copper (blue line), mono-layer graphene on liquid copper (orange line), and monolayer graphene at room temperature (green line). The *in situ* characterization with the Raman shows a visible G band, the 2D band is almost completely covered by the background of the black body radiation.

time between the flux of the gas in the tube and the opening of the valve is called accumulation time. The partial pressure of the flux of methane during the pulse was measured with a mass spectrometer, and the results are shown in Figure 4.1. The burst-pulse height was controlled by the accumulation time of CH_4 in the pipe. It is worth to notice that, above 10s pulse, a peak of the partial pressure was appreciable. The duration of the peak was around ~ 1 s, and it slightly increased with the increase of the accumulation time. Three growths with different nucleation densities are described in Section 4.2. In Section 4.3, the effect of the particle impurity for the heterogeneous nucleation is outlined.

The *in situ* Raman measurements were done on the mono-layer graphene and on a multi-layer graphite structure; the spectra are shown in Figure 4.2. In both cases, the G band is visible; the 2D band, however, is almost entirely covered by the background of the black body radiation. At room temperature, the G band of the graphene shows a redshift towards a higher wave number, and the 2D band is clearly visible. The $\text{Int}(2\text{D})/\text{Int}(\text{G})$ ratio is ~ 1 , confirming the mono-dimensionality of the material. The negligible intensity of the D band is a proof of a low number of defects in the crys-

tal. Even if some bands can be detected at 1400K, the background is still an issue. The measurements should be done at higher excitation energy in order to have a higher signal to noise ratio. One of the possible solutions to overcome this problem could be to update the instrument in such a way as to detect the anti-stoke signal. The main technical problem however is that the optical components commonly available on the market are optimized for visible light, and the anti-stoke signal have even lower wavelength than the stoke. The collaborators of the University of Patras (Greece) are working to overcome this issue. The *ex situ* Raman characterization of the graphene growth on liquid copper is presented in Section 4.4.

4.2 Growth scenarios

4.2.1 Low nucleation density

Low-density nucleation will occur if the accumulation time is 0 s, and the surface of the liquid does not present particles impurities. As discussed in Section 1.2.2.2, the liquid surface does not have grain boundaries or defects that can trigger the nucleation of graphene. With a low initial pressure of methane, therefore, the concentration of carbon ad-atoms on the copper was not high, and the nucleation events were rare. Furthermore, it was proven that the carbon atoms on the surface of the liquid preferentially stick to the few flakes formed, rather than form a new nuclei[53]. In the growth presented in Figure 4.4.a, for example, just three flakes were grown in 10 minutes in a $\sim 1 \text{ cm}^2$ surface.

Figure 4.4.a shows the evolution of the flake shape with time. When the nuclei of graphene are formed, the shape was round because, as discussed in Section 1.2.1, the formation energy for the zig-zag edge and the armchair edge are similar, and the nuclei tend to minimize his surface-volume ratio. The growth mechanism described in that Section, however, favors the disappearing of the armchair edge. The carbon atoms attached on the side of the flake, in fact, can diffuse on the border of the latter. It turns out that the energy of the attachment on an armchair edge is lower than on the zig-zag one, and during the growth, the first one is slowly consumed[25]. Edges of the same kind are at $2n \cdot 30^\circ$ (with n real number); the predominance of one edge with respect to the other makes the crystal hexagonal.

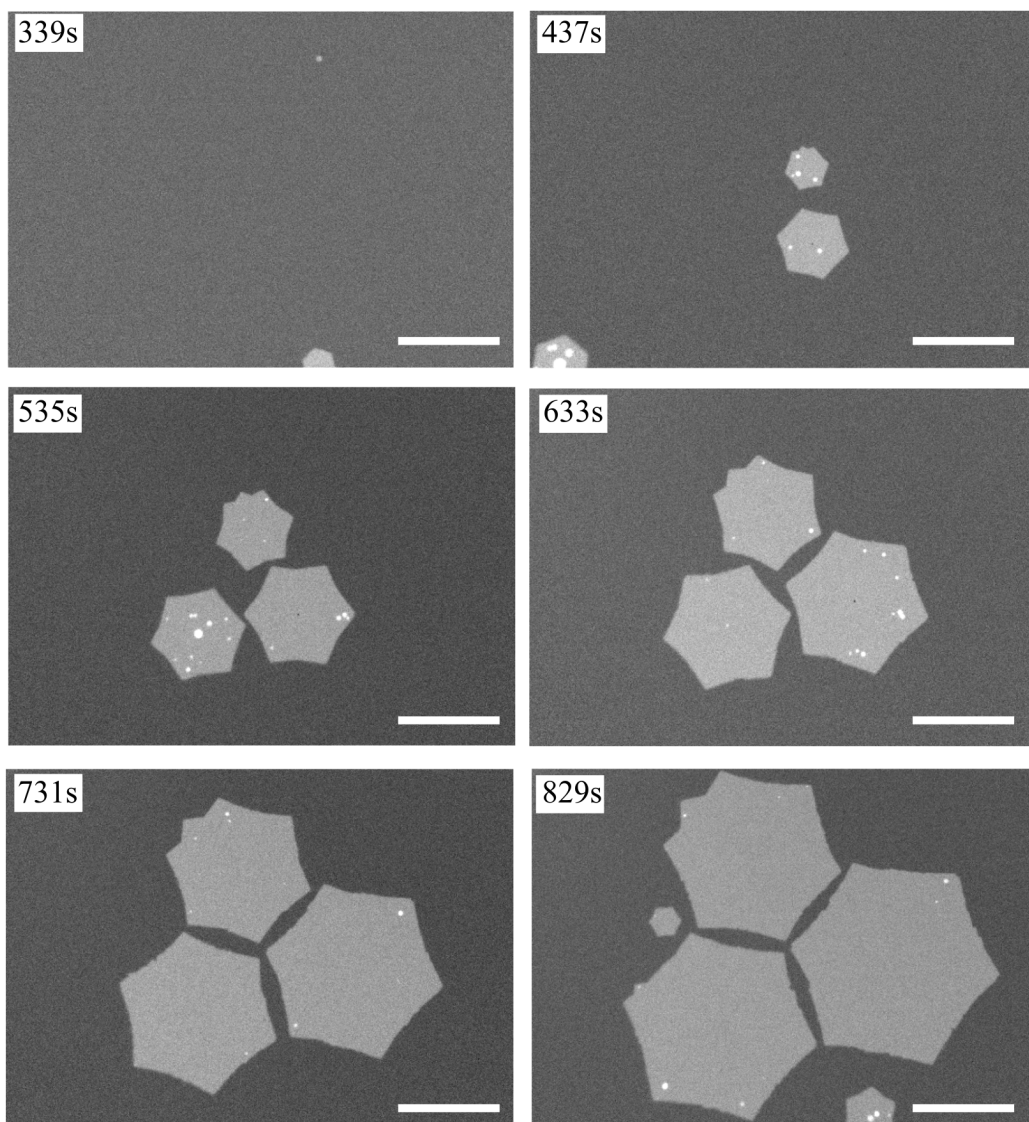


Figure 4.3: Optical microscope images. The frame of the movie recorded during the growth of graphene without accumulation time. The scale bar is 1 mm and the time 0 correspond to the opening of the CH_4 gas.

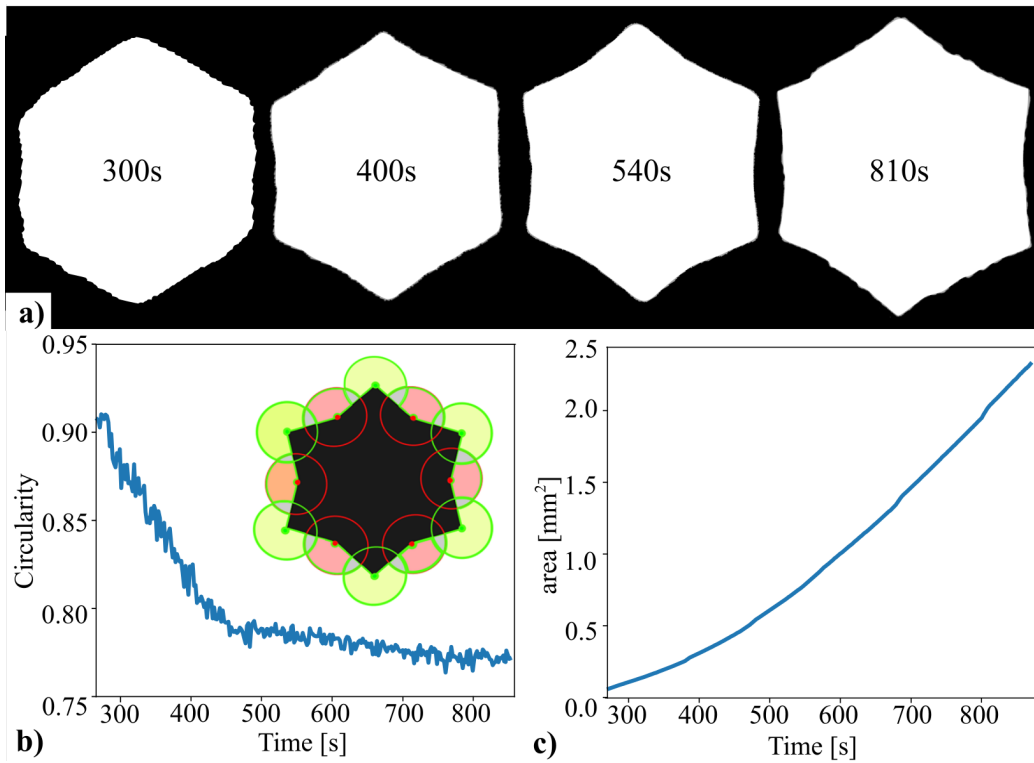


Figure 4.4: a) The shape of the flake of graphene with the time. The graphene hexagon evolves from having convex corners to concave ones. Above 810s, the side of the graphene is rough. b) The evolution of the circularity with time. In the inset, the carbon atoms on the corners of the polygon (green points) face a wider external area with respect to the one in the center of the side (red points). c) Evolution of the area of the flakes with the time

In order to estimate of the shape of the flake at a given time, the circularity parameter is defined as:

$$4\pi \frac{Area}{Perimeter^2} \quad (4.1)$$

The closer to 1 is the circularity, the closer to a circle the shape is; the value of circularity for a hexagon is 0.907. The value of circularity with the time is shown in Figure 4.4.b. The increasing of the flake size with time is shown in Figure 4.4.c.

During the firsts minutes of the growth (300s in this case), the flake showed a hexagonal shape with rounded convex sides. The majority of the armchair edges, probably, were not entirely consumed yet. At 400 seconds, the flake has a hexagonal shape, the carbon atoms attached on the side had enough time to diffuse on the edges and to find the most energetic suitable place (armchair) to occupy. With the increase of the size, the graphene flake modified its shape and decreased its circularity.

At 540 seconds, the corners of the flakes were elongated, and the sides were concave. This particular shape can be explained in this way: as discussed in Section 1.2.1, the concentration of carbon ad-atom coming from the copper is higher on the corners of the hexagon with respect to the sides. From a geometric point of view, in fact, the corners face a wider copper surface with respect to the side and therefore received more carbon feedstock (see Figure 4.4.b inset). The concentration gradient of the carbon atoms was simulated by Vlassiuk *et al.* that confirmed this behaviour[36]. If the diffusion distance is smaller than a critical value, the carbon atoms coming from the corners have time to diffuse to the most energetic favorable site of the flake (usually the centers of the sides). When the crystal is too big, however, the path of the C atoms towards these sites is too long; they do not have enough time to diffuse, that another C atom fixes the position on the previous one. The more convex the flake is, the wider area the corners face with respect to the side, in a self-sustaining process.

The final shape presented here is shown at ~ 810 seconds; the flake presents jagged sides. When the sizes of the flakes are orders of magnitude higher than the depletion region of carbon ad-atoms, the shape of the flakes becomes rough with small lobes adorning the side [105]. This shape is called dendritic-skeletal[106], and it was also reported in other works on solid[107, 108] and liquid[27] catalysts.

The largest crystal grown was 2.3 ± 0.1 mm in size (see Figure 4.4.a), with a speed of growth of ~ 0.003 mm²/s and a nucleation density of 16 cm⁻².

Above this size, the crystal started to interact with the graphene grown from the edge of the liquid copper surface, and the layer was closed. The very slow growth rate was due to the fact that the partial pressure of CH_4 was set to a low value. Increasing it during the growth may induce new nucleation, and therefore more grain boundaries in the final result.

Etching the graphene grown in these conditions required time (~ 30 min), and it did not show signs of grain boundaries, attesting to the quality of the material.

4.2.2 Medium nucleation density & auto-alignment

For a medium nucleation density, the methane needed to be "pulsed" for a short time (usually 30s in our system). As shown in Figure 4.5.a, the flakes nucleated randomly on the surface of the liquid Cu. After a small increase in size, the crystals attracted each other and collectively moved towards the center of the liquid puddle. The distance among them decreased during the first seconds of the growth to finally stabilize at $\sim 20 - 40 \mu\text{m}$, the flakes then increased their size keeping a constant gap.

Figure 4.6.a shows a medium nucleation density growth with a higher magnification. This Figure nicely shows that the flakes were self-aligned in a common direction; the Fourier transform of the image (Figure 4.6.b) highlights the six-fold symmetry of the system. The videos suggest that the alignment was caused by a competition between a long-distance attraction force and a short distance repulsion one. The theoretical explanation of this interaction was given by our collaborators of the Technische Universität München (Germany). They claimed that the capillary interactions are the cause of the attraction, while the electrostatic forces were the cause of the repulsion. As described in Section 1.3.2, the particles on a fluid interface can have an irregular contact line with the liquid, and the respective capillary forces can be rationalized as multi-pole charges. Danov *et al* derived the equation for the difference of the capillary interaction energy between two particles[79]:

$$\Delta W(L) = -2\pi\gamma Q_1 Q_2 K_0(l_c L) \quad (4.2)$$

where L is the distance between the center of the two particles, γ is the surface tension, Q_1 and Q_2 are the capillary charges of the two particles, K_0 is the modified Bessel function, and l_c is the capillary length. The capillary charge for a three-phase contact angle for spherical particle was derived in

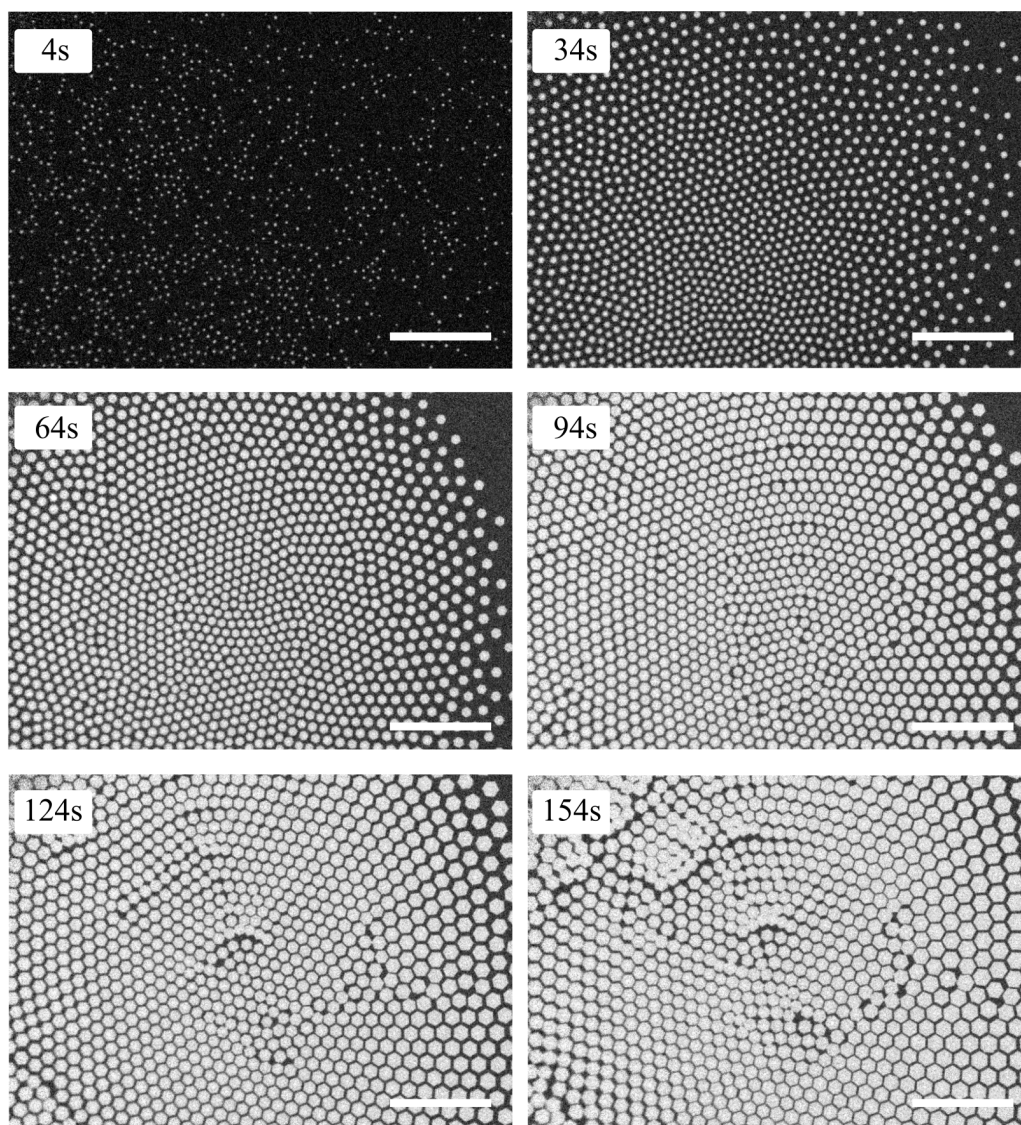


Figure 4.5: Optical microscope images. The frame of the movie was recorded during the growth of graphene with 30s accumulation time. The graphene randomly nucleates on the surface of the liquid copper. After a few seconds, the flakes tend to aggregate. When the gap between the flake is at $\sim 40 \mu\text{m}$, the flake stop to get closer, and they auto-align; this phenomenon is due to attractive capillary interactions and repulsive electrostatic forces. The scale bar is 1 mm and the time 0 correspond to the opening of the CH_4 gas.

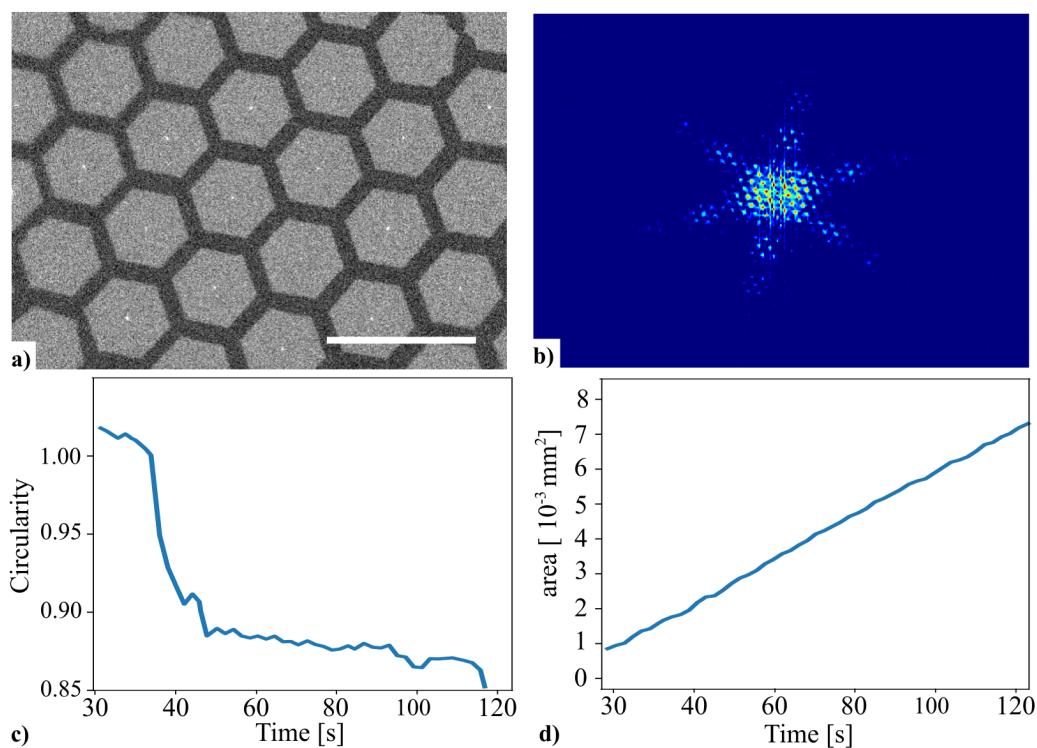


Figure 4.6: a) Frame of a movie recorded with the optical microscope, the scale bar is $150 \mu\text{m}$. The flakes of graphene are perfectly aligned. b) the Fourier transform of the image a), it is possible to notice the six-fold symmetry of the graphene pattern. c) Circularity of the graphene decreases with time until a constant value closer to the theoretical one of the hexagon (0.907). d) Average area of the flakes with time. The time 0 correspond to the opening of the CH_4 gas.

Ref[79], and it requires the estimation of the value of interface energy between the graphene and the vapour and the graphene and the copper. These two variables were retrieved with the molecular dynamics (MD) simulation.

The short distance repulsion is caused by electrostatic forces. Graphene and copper have, in fact, two different Fermi levels; as soon as they are in contact, a charge transfer occurs (calculated to 0.0445 ± 0.0001 electrons per C atom). The dipole moment between the metallic surface and the image charge in the conductor was calculated with the MD simulation. They estimated that the two forces were in equilibrium at $\sim 102 \pm 14 \mu\text{m}$ in qualitative agreement with the gap between the flakes measured experimentally. They related the difference with the observed gap to the simplicity of the model employed.

As the growth progressed, the symmetry of the system eventually broke, and the flakes started to collide and merge. There were two reasons for the loss of symmetry in the super-lattice: the first one was related to defects like dislocations, different shape or size of the flake. The second reason was due to the limited size of the sample surface: when the flakes fill all the copper surface, the ordered flakes started to merge with the graphene grown on the border of the liquid from the impurities. This leads to a loss of the arrangement, and the flakes started to collide.

The circularity of the flakes decreased for the first seconds until it reached ~ 0.9 , closer to the theoretical value of a hexagon, and it remained constant, as shown in Figure 4.6.c. The shape analysis of the flake revealed that the area increased linearly with time (see Figure 4.6.d).

The average flake size was $(9 \pm 4) \cdot 10^3 \text{ nm}^2$, the speed of growth is $550 \mu\text{m}^2/\text{s}$. The nucleation density was 12290 cm^{-2} .

The etching started from the borders of the joined flakes. This was due to the fact that the grain boundaries between the flakes could not be removed. Cho *et al.* suggested to increase the partial pressure of methane after the growth to reduce the grain boundaries, but also in this case, the etching had similar behavior [74].

The medium nucleation density growth can be useful if aligned graphene flakes are needed on the surface of a substrate or if a fast growth is needed. Even if the growth of the single flake is slower than the low nucleation growth, the high number of flakes can quickly cover a wide surface.

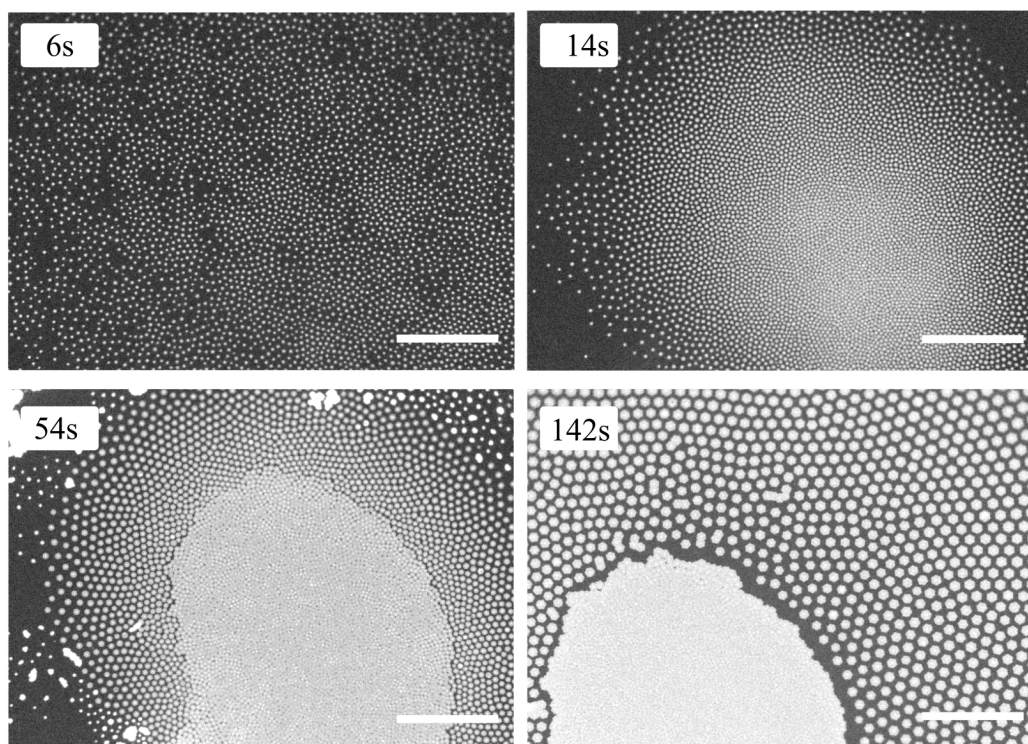


Figure 4.7: Optical microscope images. The frame of the movie recorded during the growth of graphene with 60s accumulation time. The high number of graphene flakes coalesces in single polycrystalline graphene in 54 s. The scale bar is 500 μm and the time 0 correspond to the opening of the CH_4 gas.

4.2.3 High nucleation density

The nucleation density can be substantially increased by increasing the accumulation time of the CH_4 gas in the line. Figure 4.7 shows a growth with an accumulation time of 60 s. Six seconds after the release of the methane, 18.76 mm^2 of the copper surface accessible with the microscope was covered by more than 10^5 small flakes. The nucleation density was 550000 cm^{-2} . After 14 seconds, the flakes aggregated on the center of the liquid, and they merged. The carbon clusters did not have enough time to grow before sticking with the neighbor one, and many grain boundaries were formed. The coalescence was extremely rapid, of the order of seconds, and a poly-crystalline millimeter size graphene was produced. The flakes, that did not merge at the first seconds, surround the bigger graphene and did not merge anymore. The etching was very fast, and it revealed the many defects of the flake. The high nucleation density growth can be used if a fast growth is needed, and the quality of the result is not of extreme importance.

4.2.4 Real time control of the growth

The *in situ* monitoring opens the possibility of modifying the parameters of the partial pressure of the CH_4 during the growth in the most suitable moment. The symmetry of the self-aligned flakes, for example, can be increased with alternating growths and etching cycles. As discussed in Section 4.2.2, the symmetry of the self-alignment can be disturbed by flakes of different sizes. In this case, the etching removes the smallest flakes and leaves fragments of the bigger ones. When the CH_4 flow is restored, the remaining flakes can regrow again. Figure 4.8.A-E shows the growth with etching cycles. The symmetry of the system is shown with the Fourier transform of the image in Figure 4.8.A4.8.F-J. The first frame shows a grain boundary in the superlattice order of the flake, underlined with a white dotted line of the Figure 4.8.A. The Fourier transform in the juxtaposition of two six-fold symmetry, rotated of 34° , as shown in the Figure 4.8.F. When the etching starts, the flakes reduce the volume, and they become rounded; no symmetry can be found. In the second growth, the flakes have a wide difference in size. Therefore the surface was partially etched and re-growth for a third time. This time the flake are well oriented in a single direction. The Fourier transform show a six-fold symmetry.

The monitoring can also be applied in order to reduce the number of flakes

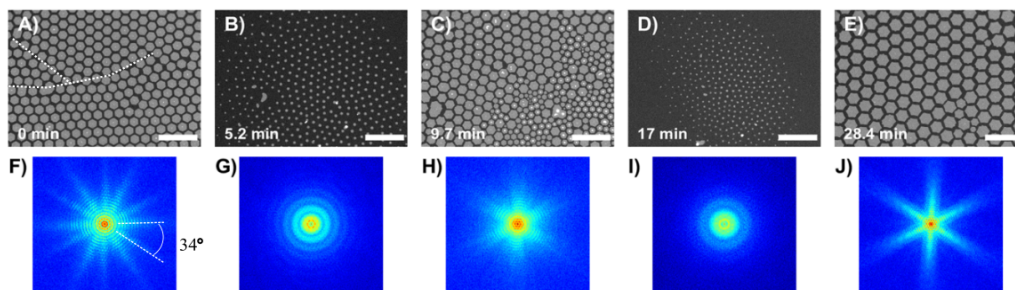


Figure 4.8: In this Figure, the etching and regrowth increase the symmetry of the self-aligned flakes. During the cycle, the Ar and H₂ flow was kept constant at 200 sccm and 20 sccm, respectively. The pressure was constant at 200 mbar, while the partial pressure of methane was varied. a) the first growth is started, b) the methane flow significantly decreased and the system was etched, c) The methane flow was increased, and the growth led a bimodal size distribution d) second etching, e) second growth, the graphene flakes organized in a hexagonal network. f) g) h) i) j) are the Fourier transform of the images shown upwards, and they help to visualize the symmetry of the graphene. The scale bar is 500 μm

on the copper surface. For not pulsed growth, a small number of flakes can nucleate at different times. Because the growth speed is the same for all of them, the firsts one nucleated are bigger than the other one. This difference in size can be used to reduce the number of flakes. If the partial pressure of methane is reduced, in fact, the graphene starts to be etched. The etching can be continued until the smallest flakes disappear entirely, and, at this point, the methane can be re-introduced to resume the growth.

In both experiments described, monitoring the surface was crucial to know when to decrease or increase the partial pressure of methane, and if the result of the procedure meets the expectation. The etching and growth cannot be set *a priori* but, it must be tuned for each experiment. The RMOM is, in this sense, a necessary tool for growing graphene on liquid copper.

4.3 Particles impurity

On the liquid copper, the impurity particles floating were a cause of undesired high nucleation. The copper film always contains particles; when the copper

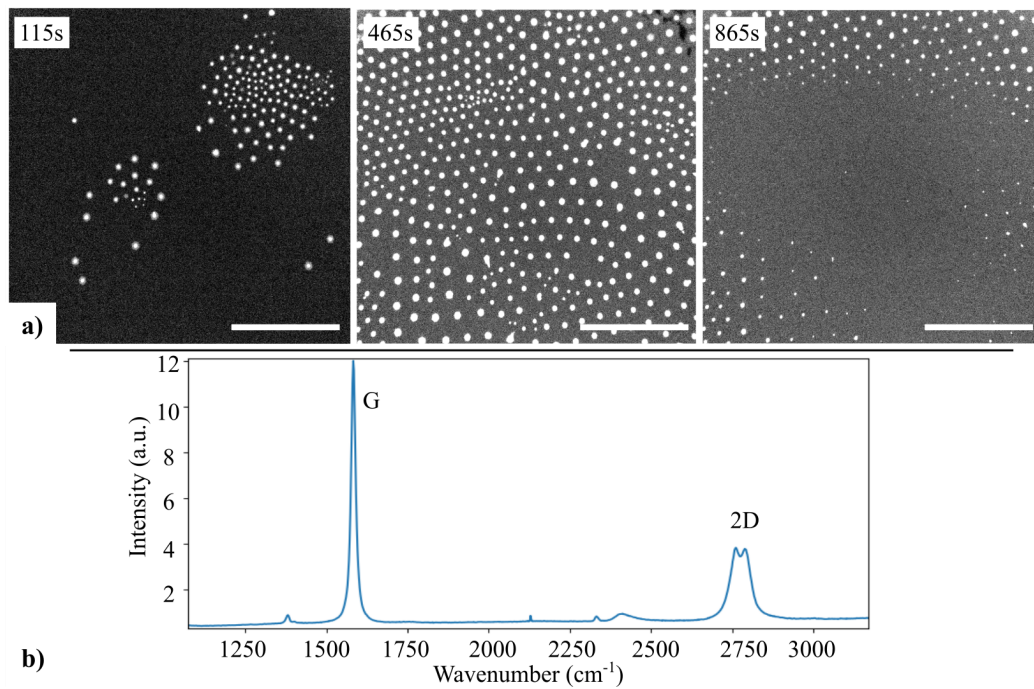


Figure 4.9: a) The growth of graphene from the impurity particles of the copper. The flakes present a white spot in the middle; when the layer of graphene is closed, the white spot remain for a few minutes and then they disappear. b) The *ex situ* Raman spectra on the center of the bright spot. The G band's presence confirms the presence of the carbon, the low intensity of the 2D band with respect to G is a proof that the white spots are 3D layer. The scale-bar is 1mm.

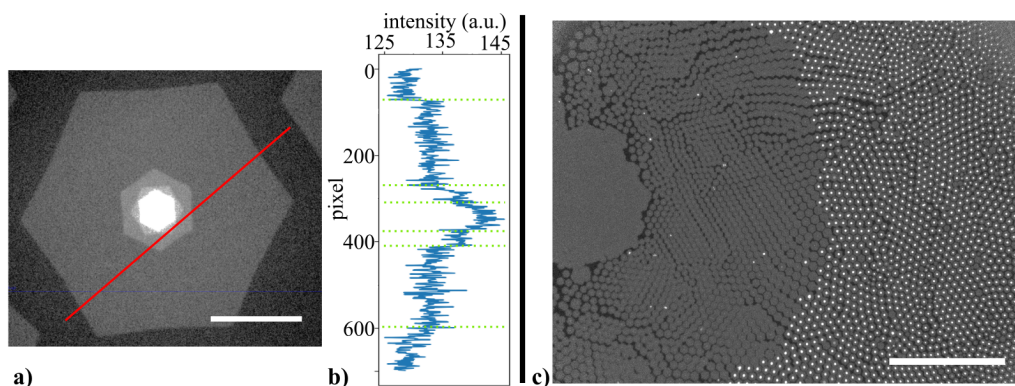


Figure 4.10: a) Zoom on a flake with a multi-carbon structure in the center, the scale bar is $200 \mu\text{m}$. The projection of the intensity on the CCD camera was made along the red line, and the result is shown in b). c) In this growth, the flakes of the left were grown on the center of the Cu puddle that did not contain impurity particles; the graphene did not show the white spots on the center. On the right, however, the flakes were grown on the side, and then they drifted towards the center due to capillary forces. In this image, it was possible to appreciate the shape of the flakes nucleated for different causes. The scale-bar is 1 mm.

melted, the particles went with the front of the melting towards the side, due to the Marangoni effect[109]. The Marangoni effect is the mass transfer along the surface of two fluids due to a gradient in the surface tension. It was proven that the particles on the surface of the catalyst could induce nucleation[110]. Figure 4.9.a shows a growth where particles triggered nucleation. In the growth presented, the liquid copper was not etched in H_2 atmosphere for the same time as the previous growth described above, and white particles were floating on the surface. Once the methane was flown, the flakes started to nucleate; in the center of the flakes, it was possible to observe brighter spots. The flakes aggregated on the liquid and cover the surface. Once they merged, the brighter spots slowly disappeared. The *ex situ* Raman spectra shown in Figure 4.9.b was acquired on the spots, and it proved that they were multi-layer graphene.

In Figure 4.10.a, it is shown a magnification of the center of the flakes. As can be noticed, the center was formed by few hexagons rotated of 30° with respect to each other. The intensity recorded by the microscope scales linearly with the number of layers of the graphene as discussed in Section 2.5;

Figure 4.10.b shows the intensity acquired by the Basler CCD on the red line of the previous image. Figure 4.10.c shows a growth in which flakes grown in the center of the sample do not have the white particle in the middle, while the one on the side they have. In this case, it was recorded that the central flakes without white spots were growing in the center of the puddle, while the other one they were nucleation from the side of the copper (full of impurities), and later drifted to the center.

In literature, there are two models to explain the growth of multi-layer graphene triggered by impurities: the wedding cake model and the inverse wedding cake model[111].

In both models, the impurity particles rise above the surface of the metal and lower the nucleation energy. In the wedding cake model, the C ad-atoms on the surface of the catalyst can diffuse on the surface of the graphene after overcoming an energetic barrier[112, 113]. When they reach the impurity, they nucleate and form a second layer. In the inverse wedding cake, the second layer is growing under the first one. The carbon feedstock is provided by atoms that diffuse into the metal[114, 115] and partially through the impurity itself[116, 111]. Even though no experiments were done to prove one model at the expense of another, previous authors working on liquid metals explain the formation of the multi-layer graphene by the diffusion of carbon under the first catalyst atoms, as discussed in Section 1.2.2.2. Although in these cases the formation for the multi-layer was not triggered by impurities, the inverse wedding cake model may be the most probable scenario.

In both cases, the first layer grows faster, and it locally covers the metal surface, blocking its catalytic ability. If the flake is small, the carbon ad-atoms can diffuse from the surface of the metal to the second layer. When the flake is bigger, fewer atoms can reach the second layer that starts to be etched. This effect can be noticed in Figure 4.9.a: at the beginning, the flakes were small, and the central white dots were present. As soon as they attached together, a layer rapidly covered the liquid surface. The carbon atom supply decreased, and the multi-layers disappeared. The graphene grown in this way could be easily etched in the center, meaning that the impurities created defects on the 2D material.

Interesting is the behavior of the particles during the re-solidification of copper. If the surface did not present graphene, the particles follow the front of solidification until all the surface was wholly solidified; usually, they all gathered in the center of the Cu puddle. If the graphene was present, the particles moved until they collided to the border of the flake that blocked

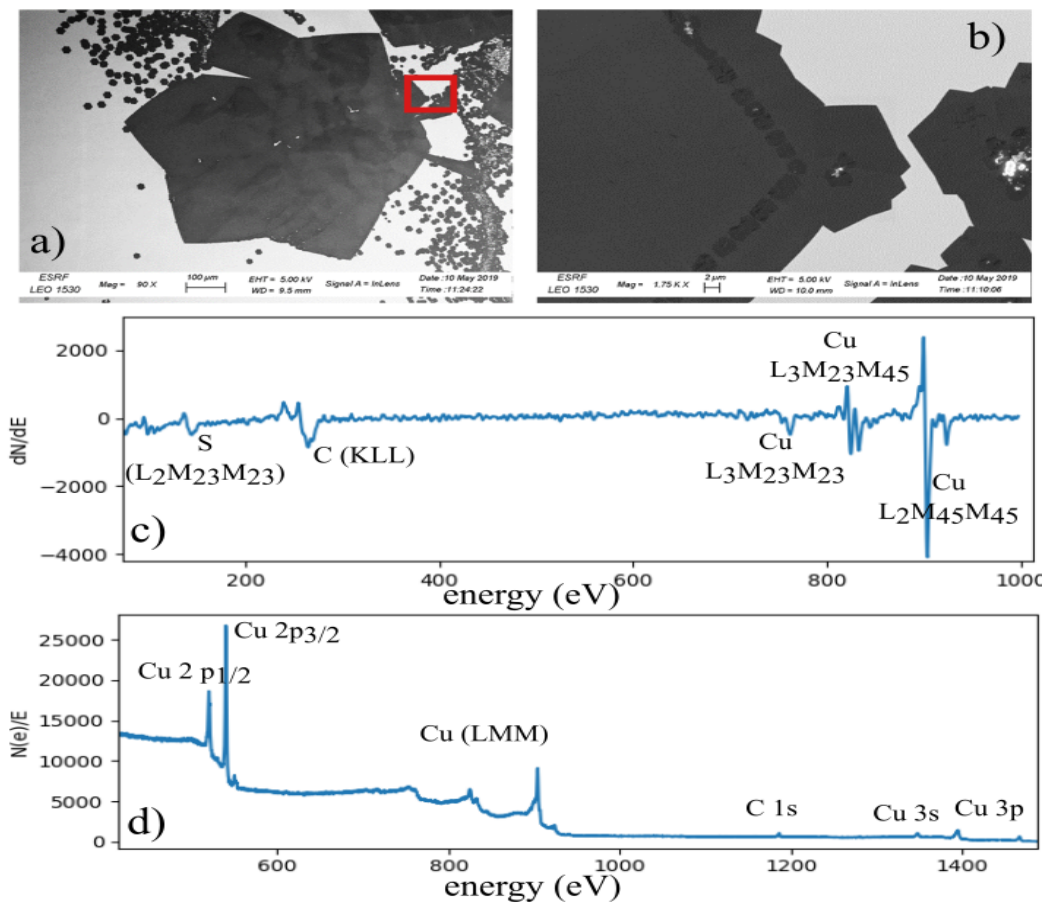


Figure 4.11: a) SEM image of the surface of the resolidified copper with flakes previously grown on the liquid phase. The zoom on the red rectangle is shown in b). The accelerating voltage was 5 keV, working distance 9.5 mm. The resolidified copper with the graphene was inserted in a UHV set up and degassed at 250°C. Then a Auger and a XPS spectra were acquired. They are shown in c) and d).

them, as also reported by another study[111]. Figure 4.11.a shows a SEM image of the surface of Cu after the growth. During cooling, the CH_4 flow was never stopped in order to avoid etching the graphene with H_2 . It is possible to notice that small hexagonal flakes surround the big flake (grown on the liquid). Those small flakes were nucleated from the impurity particles drifted to the center during cooling. As can be seen, they either present a visible white spot or multi-layer graphene in the center, symptomatic of nucleation from defects[116, 111]. Also, the white particles surrounding the flake acted as nucleation points, as can be seen in Figure 4.11.b. The new small graphene flakes attached around the big one, and they form grain boundaries.

The drifting of the impurity particles towards the center can be limited if the layer of graphene covers all the surfaces. In order to prove this statement, *ex situ* characterization was done with XPS and Auger spectroscopy on the Cu surface entirely covered by graphene. The sample was solidified and moved in the UHV chamber and degassed at 250°C . The Auger and the XPS spectra are shown in Figure 4.11.c and 4.11.d, respectively. From the Auger spectra, it was possible to notice (in addition to the Cu and C) an S peak. In the XPS data, no trace of S was detected. The Auger was more sensitive to the element of the surface with respect to the XPS, meaning that the S atoms were present in small quantities only on the surface. The purity of the melted copper under the graphene was very high, and no further contaminations were detected.

Removing these particles is of utmost importance for the reproducibility of the process and the production of defect-free graphene. In order to remove these particles, the liquid copper is etched for 2 hours or more under 10 sccm of H_2 and 100 sccm of Ar. The advantage of using the optical microscope is that the quality of the growth can be recognized a few minutes after the injection of the precursor. If undesired pollutants are still present after the annealing, the growth can be stopped, and the etching restarted.

4.4 Assessing the quality of the graphene layer grown

To confirm the quality of the produced graphene, *ex situ* Raman measurements were done. Some graphene flakes were transferred on Si wafer and

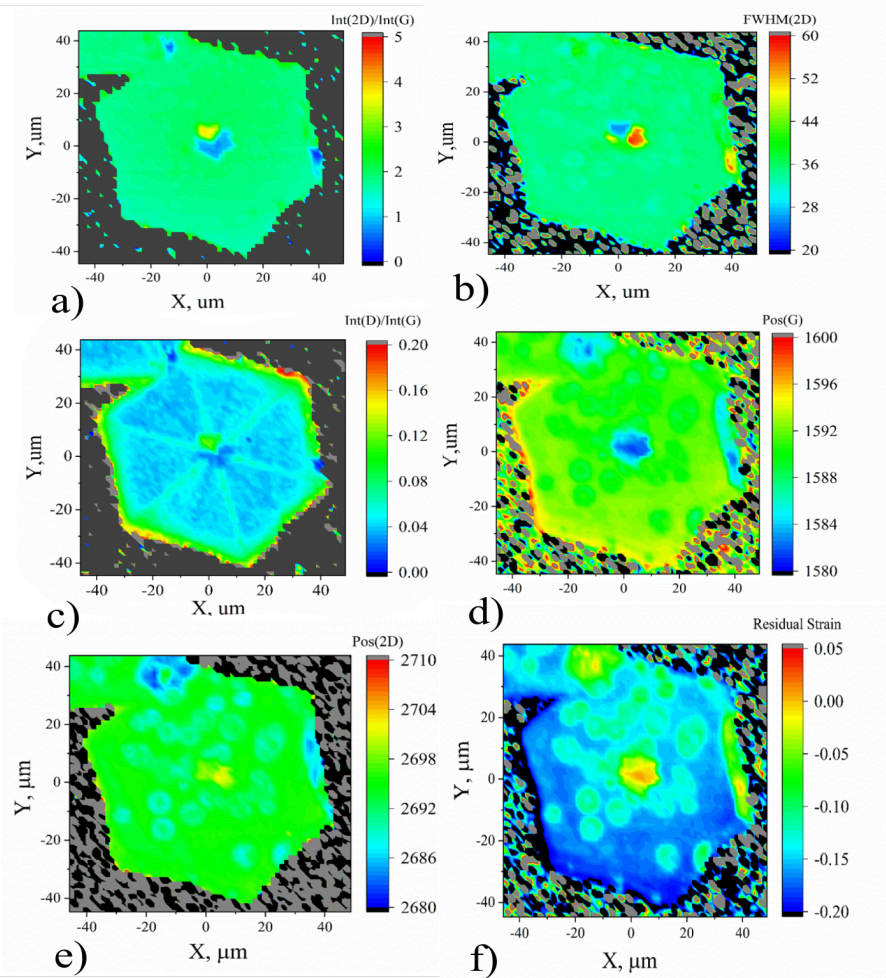


Figure 4.12: The maps shown are respectively: a) $\text{Int}(2\text{D})/\text{Int}(G)$, b) $\text{FWHM}(2\text{D})$, c) $\text{Int}(D)/\text{Int}(G)$, d) $\text{Pos}(G)$, e) $\text{Pos}(2\text{D})$, f) residual strain. The Figures were gently provided by the University of Patras.

analyzed with a $\lambda = 514$ nm Raman by our collaborators of the University of Patras; the results are shown in Figure 4.12.

The confirmation of the bi-dimensionality of the flakes is given by the map of the $\text{Int}(2\text{D})/\text{Int}(\text{G})$ and the $\text{FWHM}(2\text{D})$. In the first case, the plot shows a uniform value of 2 interrupted only in the center. The second map shows a value of FWHM of 32 cm^{-1} , very close to the theoretical one of 30 cm^{-1} for mono-layer graphene. The ratio of $\text{Int}(\text{D})/\text{Int}(\text{G})$ gives information on the density of defects on the material. In the data presented, the ratio is meager (~ 0.05). The graphene had, therefore, good quality. The 2D maps of the position of the 2D and the G band shows the chemical uniformity of the flake.

The last map shows the strain on the flake that is mostly negative. Although the expansion coefficient of the free-standing graphene is negative, the graphene is situated on the surface of the Cu that has a positive expansion coefficient. The Van der Waals interaction between the flake and the Cu makes the graphene compress during cooling. This compression, however, is not intense in absolute value, the graphene is relaxed on the Cu.

To conclude, the graphene growth is mono-layer and with a low defect density, confirming the high quality of the product produced.

4.5 Conclusion

In this chapter, the advantages of the use of liquid copper catalysts were exposed. The nucleation density was easily controlled, changing the partial pressure at the beginning of the growth, and three different growth possibilities were described. The size and the quality of the flakes produced were considerably high, making the liquid metal attractive catalysts for graphene production. The RMOM powerfully highlighted the potentialities of the liquid metal. The *in situ* monitoring of the growth gave high flexibility and control; the growth could be restarted if impurity particles were still present. Etching, and re-growth cycles could increase the symmetry of the system or could decrease the nucleation density. The period of etching and re-growth vary from growth to growth, and it could be determined only thanks to the RMOM. In conclusion, a simple and effective graphene production method was exposed, and RMOM proved to be a fundamental characterization method.

Chapter 5

Analysing XRR data from a bent surface with a 2D detector

5.1 Introduction

X-ray reflectivity (XRR) is an established technique that allows measuring the out-of-plane density profile. A sample is illuminated with a beam at a grazing angle α ; the detector (placed at an angle $\beta = \alpha$) records the intensity. At the end of the measurement, a curve describing the decay of R with q_z is achieved. In a classic XRR measurement, the surface of the sample is flat because the reflected intensity can be uniquely associated to the angle set in the diffractometer.

In order to better understand the importance of a flat surface in XRR, let us divide the beam in a bunch of infinitesimal rays, as shown in Figure 5.1.a. Each rays impinges on the surface with the same incident angle $\alpha_l = \alpha$ and reflect with the same angle $\beta = \alpha_l$. In this ideal case, the beam is not spreading and the intensity recorded on the detector is the sum of the intensity of lines having the same incident angle. Therefore, it is possible to associate the total intensity of each detector image to a single angle.

The flatness of the surface, however, is a condition that cannot always be satisfied. Usually, when the sample is a small quantity of liquid, it has a convex shape. In this case, every infinitesimal ray impinges on a region of the surface that has a different incident angle, and at small angle, some of them do not touch the sample (see Figure 5.1.b). The incident angle of the single x-ray element will be $\alpha_l = \alpha + \Delta\alpha$, with $\Delta\alpha$ the local increment of the

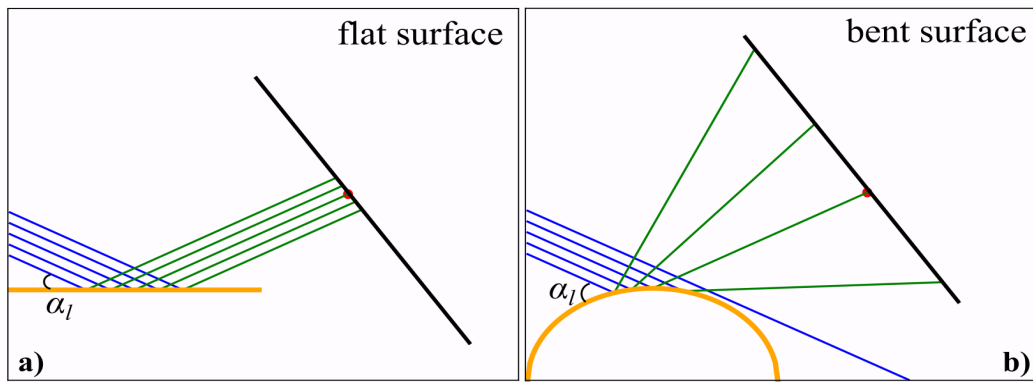


Figure 5.1: The effect of the reflection from a bent surface can be easily understood dividing the beam into many lines (blue lines) and checking the behavior of the reflection (green lines). a) The incoming lines are reflected from a flat surface: α_i (the local incident angle) is the same for all the lines, and the reflected beam has the same size as the incident beam. b) The incident lines are reflected from a convex surface, the α_i is different for all the lines and the reflection spreads in spread in the angular fan. At a small angle, a part of the beam does not touch the surface, therefore it is not reflected.

angle due to the curvature effect. Every pixel of the detector, therefore, will record an intensity coming from a different α_l . Besides, this fan of angles makes the beam spreading. In this case, the total intensity recorded by the detector cannot be associated with a unique angle, and a more advanced analysis must be done.

One of the first approaches to face this problem was done by P.S.Pershan *and co.* [117, 118, 119]. The reflected beam was scanned in the vertical direction with a point detector, and the data obtained were fitted with a Gaussian. Using a model that takes into account the contribution of the absolute intensity and the effect of the curvature, they could decouple these two factors. This method, however, requires that the vertical profile of the reflected beam is symmetric (Gaussian), but this is not always the case.

The study of XRR on a spherical cap sample was done in 1994[120]. In this article, the astigmatic aberration on the incoming ray was modeled, and the absolute intensity of the reflected beam was corrected. Both of the works described above, however, do not take advantage of the capability of the new generation 2D detectors that are now commonly used at synchrotrons.

Twenty years later, W.H.Briscoe *et al.* applied XRR on cylindrical shape objects using a 2D detector[121]. In this case, the axis of the cylinder was in the same plane with the incident beam, and the position of the reflected ray was calculated. It has been proved that, under the conditions used in the experiment, the deviation of the reflection due to the curvature was not significant. Früh *and co.* worked on the same geometry of the sample; however, with their condition, the beam was spreading significantly[122]. In their case, the signal of the reflectivity scan was integrated into a small ROI (region of interest) in the center of the arched shape reflection. They compared this data with the ones of a flat sample that showed the same results.

In a more recent paper, a method to retrieve the reflectivity of a curved liquid drop was described[123]. In this procedure, the drop was scanned vertically through the sub-micron size beam. The shape of a liquid puddle was analytically calculated[124, 104], and so the local incident angle due to the curvature was known. Despite the advantage of using a parallel beam, the model, however, is reliable only if the shape of the puddle is known, and with a very small beam, which is not so always possible to achieve.

As we discussed, the problem of the bent surface is an old issue. The methods described in the literature can be applied in two cases: if the curvature is in the plane perpendicular to the direct beam (like the cylinder),

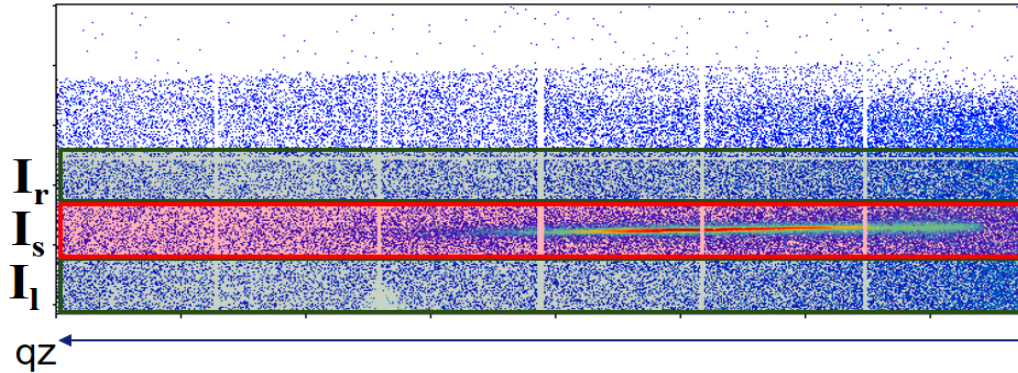


Figure 5.2: The Figure shows one detector image of the reflected beam in an XRR experiment. The detector area is divided into three regions of interest; I_s on the reflection signal and the other two (I_r and I_l) on the side of the latter. The values inside the ROIs are integrated, and the intensity of the reflected beam is calculated with the Equation 5.1

or parallel. In the last case, in particular, the experiment need to be done with complex requisite, not always easily achievable. A simple method that allows the extraction of the XRR curve with a micrometer beam size and a standard $\theta - 2\theta$ geometry, however, is still missing.

In this work, a method of extraction of the XRR from bent surfaces has been developed. The main idea is that each pixel of the 2D detector acts like a point detector situated at a specific angle that can be calculated. Even if the beam spreads due to the curvature of the sample, each pixel of the images of the scan can be associated with an effective value of the momentum transfer q_z . Then all the pixels of the images with the same momentum transfer q_z can be averaged for the statistics increase; in this way, the signal can be reconstructed. This approach has some similarities with the concept adopted in the BINocular program[125], and it is described in detail in Section 5.3.

5.2 ROI integration

One of the most common methods to extract the XRR curves is the integration of the scattering intensity on a region of interest (ROI). In this method, three rectangular areas are defined, as shown in Figure 5.2, one

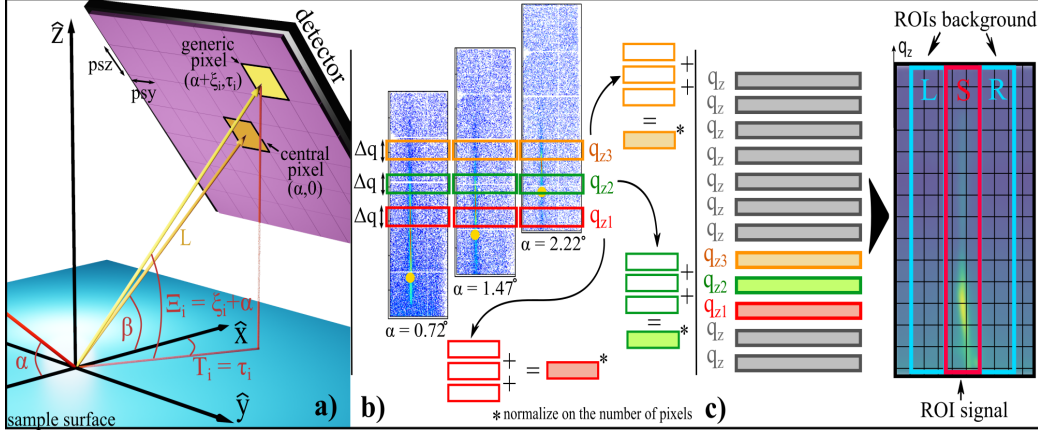


Figure 5.3: a) a point in the spherical coordinate $(\alpha + \xi_i, \tau_i)$ is associated with every pixel of every image of the scan and converted in reciprocal space. b) After selecting an interval of q_z , the program looks for a pixel that sits in that position. All the pixels in the same interval of q_z are then averaged. The orange points in the images represent the central pixel position c) The specular reflected signal is reconstructed and integrated with ROIs.

surrounds the specular reflected signal, and the other two on the side record the background contribution. The intensity recorded by the pixels inside the rectangles is summed. The resulting value of the reflected intensity is given by:

$$I_{ref} = I_s - \frac{I_l + I_r}{2} \quad (5.1)$$

where I_s , I_l and I_r are the intensity of the signal, left and right ROI respectively.

In order to obtain the intensity of the direct beam I_0 , the beam is shined directly on the detector with an appropriate known attenuation factor. The intensity of the ROI that surrounds the direct beam is integrated, and the result is I_0 .

5.3 Principles of the signal reconstruction method

The main idea behind this method is that every pixel acts as a single point detector. For each average incident angle, the area detector measures all the

reflected beam spread by the sample. The position of each pixel can be calculated and associated with a position in \vec{q} -space, where \vec{q} is the momentum transfer vector ($\vec{q} = \vec{k}_f - \vec{k}_i$) and reconstruct the signal, as shown in Figure 5.3. In order to do that, the procedure consists of four steps:

1. associating a value of q_z to every pixel
2. obtaining the reflectivity value for each pixel
3. averaging the intensities of pixels in the same range of q_z and reconstruct the diffraction signal
4. analyze the reconstruct signal and obtain the XRR curve

Each step is described in detail below, and the validity of the procedure is tested with simulated data. The results show that the XRR curve can be perfectly reconstructed, and, for this reason, this method is used in Chapter 6 on the experimental data.

5.3.1 Associating a value of q_z to every pixel

The first step of the reconstruction method consists of associating a q_z value to every pixel. Figure 5.3.a shows the geometry of the problem: the center of the $\hat{x}, \hat{y}, \hat{z}$ coordinate system is in the apex of the sphere (not represented in the Figure), the detector is placed at a distance L from the origin of the coordinate system. A generic pixel can be uniquely defined on the detector plane using two angular coordinate, Ξ and T , representing the angle between the \hat{x}, \hat{y} plane and the \hat{x}, \hat{z} plane respectively. The detector is bound to move only in Ξ of angle β that is known and set in the diffractometer, and it is equal to the angle that the incident beam forms with the sample plane α . If the detector is at $\beta = 0$, the center reference pixel is the one intercepting the \hat{x} axis, and it is situated at a distance L from the origin. Any angular position of each pixel can be then calculated as:

$$\xi_i = \arctan\left(\frac{i \cdot psz}{L}\right), \quad \tau_j = \arctan\left(\frac{j \cdot psy}{L}\right) \quad (5.2)$$

where ξ_i and τ_i are the angle Ξ and T of the pixels at $\alpha = 0$, and psz and psy the pixel size in vertical and horizontal position. i and j are the pixel number respect to the central beam in vertical and horizontal position

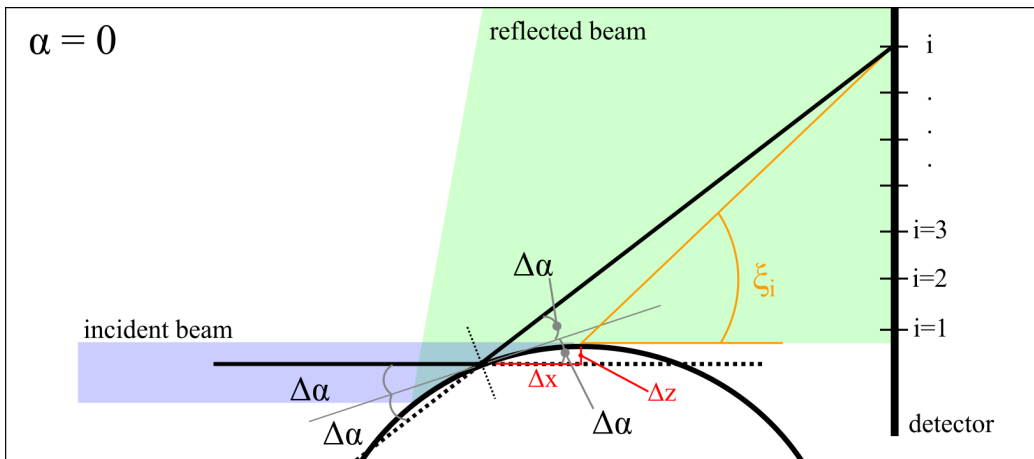


Figure 5.4: The incident beam at $\alpha = 0$ (blue area) impinges on the top of the circle. The spreading of the reflected beam (green area) is only due to the curvature of the circle. The black line is a portion of the beam that, after the reflection from the sample of $\Delta\alpha$, intercept the pixel i . The angular coordinate of i is ξ_i , while Δx and Δz are the distance between the incident point and the apex of the beam in the horizontal and the vertical direction, respectively.

respect to the central pixel. When $\alpha \neq 0$, the angular coordinates on the pixels are $\Xi_i = \xi_i + \alpha$ and $T_j = \tau_i$.

The next step is to find the relationship between Ξ_i and T_j with $\alpha_l = \alpha + \Delta\alpha$; in other words, to find the local incident angle from the pixel position. After interacting with the sample, the beam diverges in the sagittal and coronal plane. Let us start to consider the sagittal divergence in the the $\hat{x}\hat{z}$ plane at $\alpha = 0$, as shown in Figure 5.4. In this case, the spreading of the beam on the detector is only due to the curvature of the sample. The local incident angle can be calculated from the pixel position using the formula:

$$\Delta\alpha = \frac{1}{2} \arctan\left(\frac{i \cdot psz + \Delta z}{L + \Delta x}\right) \approx \frac{1}{2} \arctan\left(\frac{i \cdot psz}{L}\right) = \xi_i/2 \quad (5.3)$$

where Δz and Δx are the distances of the incident point on the circle with respect to the apex of the circle in the vertical and horizontal direction. Usually, Δz and Δx are much smaller compared to $i \cdot psz$ and L , and they can be neglected.

In the coronal plane, however, the spreading of the beam is much lower. Briscoe *and co.* derived the formula of the deviation of the beam on the detector for a cylindrical shape sample. The formula is:

$$\Delta Y = 2L \sin \alpha \sin \phi \cos \phi \quad (5.4)$$

where ΔY is the deviation of the beam on the detector in the horizontal direction due to the curvature respect to the reflection coming from a flat surface, $\phi = \arcsin(W_j/2R_d)$, W_j is the beam size in the vertical direction and R_d is the radius of the sample. With $\alpha = 5^\circ$, $L = 1$ m, $W_j = 0.05$ mm and $R_d = 200$ mm (common experimental condition in this thesis work), ΔY is $20 \mu\text{m}$. The pixel size of a Medipix detector is $55 \mu\text{m}$, therefore the coronal divergence is hardly notable.

From the pixels at angle $T \neq 0$, therefore, the signal is not present, and they do not provide information on α_l . The pixels at $T \neq 0$ however detect the background information and they are useful in the last step of Section 5.3.5. For this reason, it is possible to neglect T and consider that all the pixels in the same vertical line have the same $\Delta\alpha$ as the ones at $T = 0$. From these considerations, it is then easy to calculate the scattering vector from the vertical pixels line position with the formula:

$$q_{zi} = \frac{4\pi}{\lambda} \sin(\alpha + \Delta\alpha) = \frac{4\pi}{\lambda} \sin(\alpha + \xi_i/2) \quad (5.5)$$

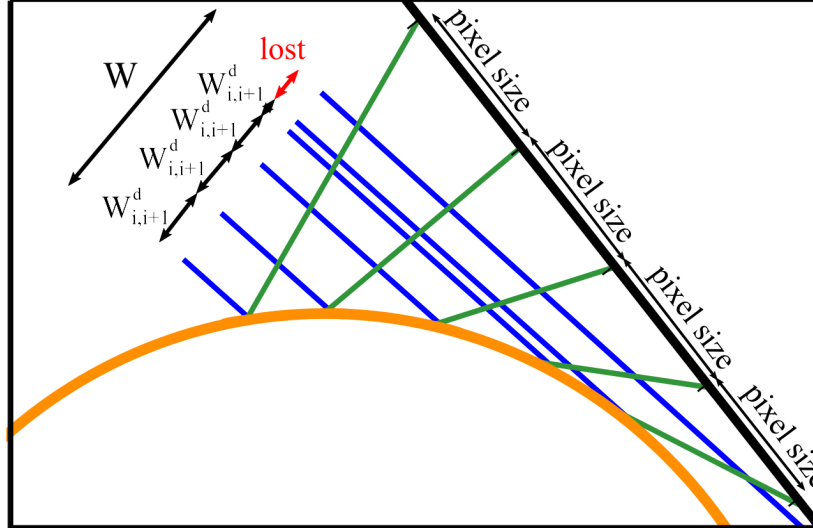


Figure 5.5: The incident beam with size W is ideally divided in smaller beams, each of them, after the reflection, shine exactly on a single pixel. The size of the beam element is $W_{i,i+1}^d$.

Two interesting considerations can be made from this discussion; the first one is that it is possible to calculate q_{zi} without knowing the radius of the sample. The second one is that it is not needed to calculate the position of each pixel, but only of the horizontal one at $T = 0$ and then work with vertical stripes of pixels (from now on called \vec{P}_i), making the computational cost lighter. Indeed it is enough to calculate once Ξ_i for each image and to proceed with the future calculations considering the pixel lines as tensor rather than every single pixel as a scalar. \vec{P}_i , therefore, contains the values of the intensity recorded by each pixel of the row, and its length is therefore j .

5.3.2 Obtaining the reflectivity values in each pixel

The second step of the reconstruction method consists of calculating the reflectivity value of each pixel of the detector. Following the Formula 2.22, the reflectivity for each pixel can be calculated as:

$$R_{i,j} = \frac{I_{i,j}}{I_{0i,j}} \quad (5.6)$$

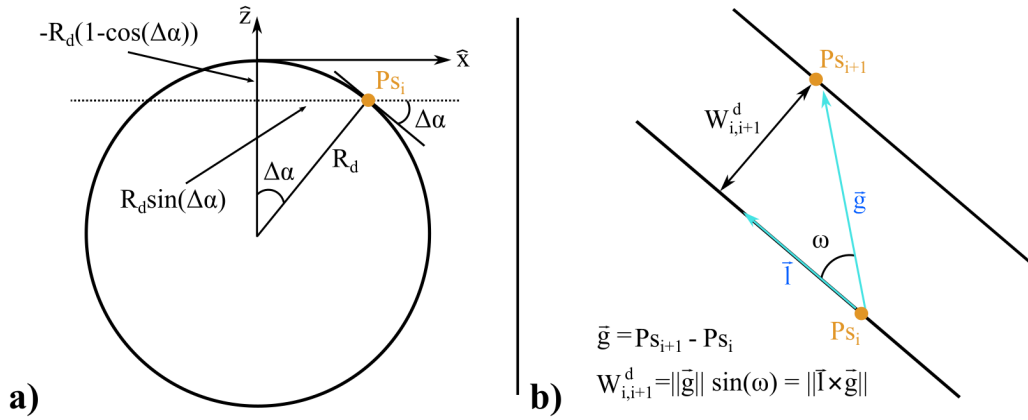


Figure 5.6: a) The coordinates of P_{s_i} can be found solving a simple geometrical problem b) The distance $W_{i,i+1}^d$ between two parallel lines passing through the points P_{s_i} and $P_{s_{i+1}}$ is the cross product between the direction of the lines and the difference between the coordinate of the points.

where $I_{0i,j}$ and $I_{i,j}$ are respectively the intensity of the direct beam and the intensity of the reflected beam on the pixel position i, j . While $I_{i,j}$ is measured by the pixels sensors, $I_{0i,j}$ must be calculated. Following the same simplification discussed in Section 5.3.1, the problem can be solved only on the $\hat{x}\hat{z}$ plane, discarding the j^{th} pixels contribution.

Let us imagine dividing the incident beam into smaller beams; each of them, once it reflects on the surface of the sample, shines entirely and only on one single pixel of the detector, as shown in Figure 5.5. The size of the beam element are called $W_{i,i+1}^d$. $W_{i,i+1}^d$ depends on the position of the pixel in the detector, e.g. for the pixels in the lower part of the detector, the $W_{i,i+1}^d$ is lower with respect to the pixels in the upper part. At low angles, it is possible that a part of the beam is lost; obviously the sum of all the $W_{i,i+1}^d$, and the size of the lost beam must be equal to the beam size W .

The direct beam intensity on the pixel is a fraction of the total incident beam intensity I_0 , and it can be calculated as:

$$I_{0i} = I_0 \frac{W_{i,i+1}^d}{W} \quad (5.7)$$

The problem now is to calculate $W_{i,i+1}^d$. Let us start to calculate the relative coordinate of the point that the incident beam with the circular sample

$Ps_i = (x_i, z_i)$ from $\Delta\alpha$. From Figure 5.6.a it is suddenly evident that:

$$z_i = -R_d(1 - \cos(\Delta\alpha)) = -R_d(1 - \cos(\Delta\xi_i/2)) \quad (5.8a)$$

$$x_i = R_d \sin(\Delta\alpha) = R_d \sin(\xi_i/2) \quad (5.8b)$$

If we define the unit vector corresponding to the direction of the direct beam as $\vec{l} = (\cos \alpha, -\sin \alpha)$, the problem is then reduced to find the distance between two parallel lines with direction \vec{l} passing through $P_{s_{i+1}}$ and P_{s_i} , as shown in Figure 5.6.b. It is possible to demonstrate that the distance is:

$$W_{i,i+1}^d = \|\vec{l} \times \vec{g}\| \quad (5.9)$$

with $\vec{g} = Ps_{i+1} - Ps_i$.

From this discussion, it is important to underline the fact that the curvature of the sample must be known. There are many techniques that allow measuring the curvature of a drop (e.g. optical reflectometry, interference contrast microscopy, grid technique exc.[104]). At some experimental conditions, e.g. high temperature or controlled pressure environment, these techniques cannot be applied.

In an XRR measurement, the spreading of the reflected beam depends on the radius of the sample, and it can be used to calculate its curvature. In the next section, the derivation of the curvature of the sample from the divergence of the reflected beam is described.

5.3.3 Obtaining the radius of the sample from the reflection profile

The length of the vertical spreading of the reflected beam on the detector depends on the curvature of the sample. It is, therefore, possible, from the images of the XRR scan, to derive the radius of the sample.

Let us assume that the sample has a circular shape and that the beam impinges entirely on the sample, as shown in Figure 5.7. The extremes of the incident beam intersect the circle (with radius R_d and center in C) at points A and B . The angle \widehat{ACB} is 2δ and can be obtained with the formula:

$$\delta = \arcsin\left(\frac{f/2}{R_d}\right) \quad (5.10)$$

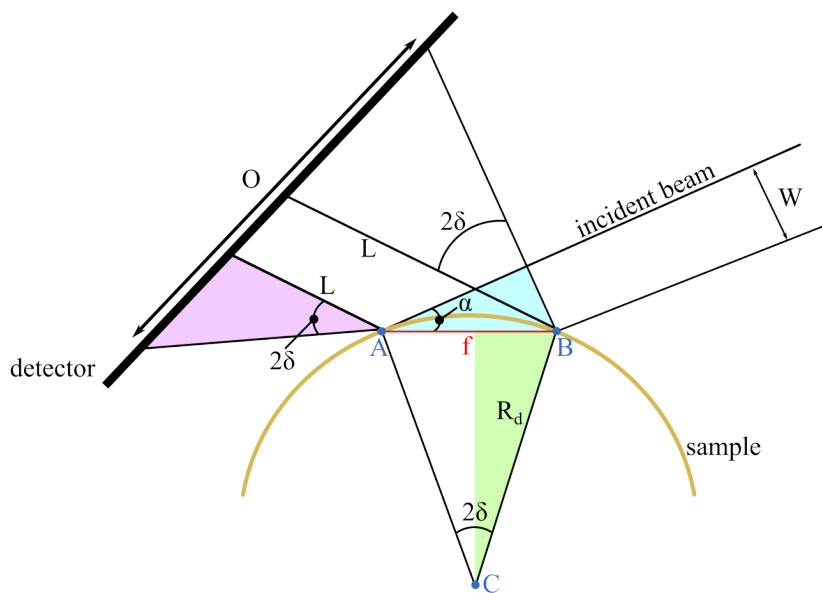


Figure 5.7: The length of the spread O depends on the radius of the sample. If the beam impinges completely on the surface of the circle, the radius can be calculated from O . In Section 5.3.3, the calculation of the radius from the spreading is shown. The three formulas to derive the R_d are trigonometric considerations on the triangle colored in the figure.

where f is the distance between A and B . f can be calculated as:

$$f = \frac{W}{\sin(\alpha)} \quad (5.11)$$

The distance between the extreme of the reflected beam on the detector is called O and it is:

$$O = 2L \tan(2\delta) + W \approx 2L \tan(2\delta) \quad (5.12)$$

Usually, the spread of the beam is much larger than the beamsize, and the latter can be neglected. Joining the equations above, the radius of the beam can be derived as:

$$R_d = \frac{W}{2M \sin \alpha} \quad (5.13)$$

where $M = \sin\left(\frac{1}{2} \arctan\left(\frac{O-W}{2L}\right)\right)$. From the detector images of the XRR measurements it is therefore possible to measure O and calculate R_d .

5.3.4 Averaging the intensities of pixels in the same range of q_z and reconstructing the diffraction signal

In Section 5.3.1, we assign a q_z coordinate each \vec{P}_i , and in the Section 5.3.2 we convert the intensity values of the images to reflectivity values. If the detector length in the vertical direction is longer than the step of the scan (condition very often verified), many images intercept the same q_z . The purpose of this step is to find in all the images the pixels in the same interval of q_z , and to average them.

The objective of the algorithm is shown in Figure 5.3.b, once an interval of Δq_z is provided, the program starts to look in all the images in order to find which \vec{P}_i are in Δq_z . The choice of the Δq_z can be associated with the choice of the voxel size in the BINocular program[125]. Then, all the rows of pixels \vec{P}_i , both coming from the same image as well as from different images, are summed and divided by the number of \vec{P}_i following the formula:

$$\frac{1}{P_{max} - P_{min}} \sum_{P_{min}}^{P_{max}} \vec{P}_i \quad (5.14)$$

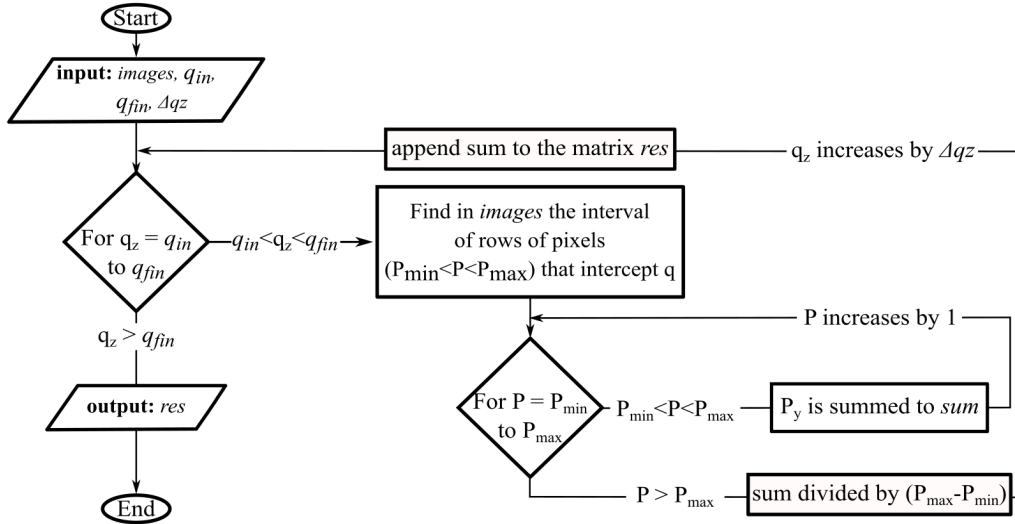


Figure 5.8: Flowdiagram of the program that searches from the reflectivity values of pixel in the same Δq_z , and it average them.

where P_{max} and P_{min} are respectively the number of the highest and the lowest pixel row in the Δq_z interval.

The flowdiagram of the script is shown in Figure 5.8; the program needs the images of the scan ($images$), the initial and final q_z of the scan respect to the central pixel (q_{in}, q_{fin}), and the step of Δq_z in which the q_{in}, q_{fin} are discretized. When the program starts, a loop begins. In every step of the cycle, the program looks for the \vec{P}_i that are in the q_z considered. Then a variable $sum = 0$ is defined, and another loop (internal to the previous one) runs from the lowest P_{min} to P_{max} . In each step of the second loop, the vector P_i in position P is summed to sum . When the second loop is terminated, the variable sum is normalized by $P_{max} - P_{min}$ and the first can proceed to the new step. Before that the next step of the first loop proceeds, sum is appended to res and Δq_z is added to q_{in} .

res is the output of the program, and it is a 2D matrix in which every row is the average values of the pixel respect to specific q_z .

5.3.5 Analyzing the reconstructed signal and obtaining the XRR curve

The 2D matrix obtained from the previous step (*res*) is the reconstructed signal of the 00*l* rod, and it has $i \times j$ size with $i = (q_{in} - q_{fin})/\Delta q_z$ and j equal to the number of pixels of the detector in the horizontal direction.

In order to obtain the XRR curve from the 2D matrix, three ROIs are selected (in Figure 5.3.c). One ROI surrounds the signal (*S*), the other two (*L* and *R*) record the background values, and they are located on the side of *S*. All the ROIs have the same size. All the values inside the ROIs at the same q_z are summed, and the background is subtracted from the signal following this formula:

$$R(q_z) = R_S - \left(\frac{R_L + R_R}{2} \right) \quad (5.15)$$

where R_S is the integrated value inside the ROI of the signal, and R_L and R_R are the values integrated with the sides ROIs. Once the final values of the intensities are retrieved, the values of $R(q_z)$ can be associated with a q_z .

5.4 Simulating the experiment

The experiment was simulated in order to test the reliability of the reconstruction method. The simulation, in fact, allows to have complete control on the parameters (e.g. curvature of the sample, distance sample detector exc.) and to change them easily.

The experiment is simulated using an approach similar to the direct ray tracing. The center of the axis (\hat{x}, \hat{z}) is set on the apex of the sample, \hat{z} is the ordinate and \hat{x} is the abscissa. Figure 5.9 shows the vectors involved in the simulation. The direct beam is simulated as a bunch of lines b_n sharing the same direction \vec{l} . The distance between a line b_n and the neighbor one b_{n+1} is s , and it depends on the number of lines N used to form the beam. The sum of all s is, in fact, equal to the beamsize W : $s \cdot N = W$. The equation of the line of the direct beam is, therefore:

$$b_n = \vec{l} + t\vec{d} = \begin{pmatrix} s_n \cos(\frac{\pi}{2} - \alpha) \\ s_n \sin(\frac{\pi}{2} - \alpha) \end{pmatrix} + t \begin{pmatrix} \cos(\alpha) \\ -\sin(\alpha) \end{pmatrix} \quad (5.16)$$

where t is the variable of the equation line, and $s_n = (s \cdot n) - W/2$.

The lines b_n intercept the sample, and they are reflected. In the simulation,

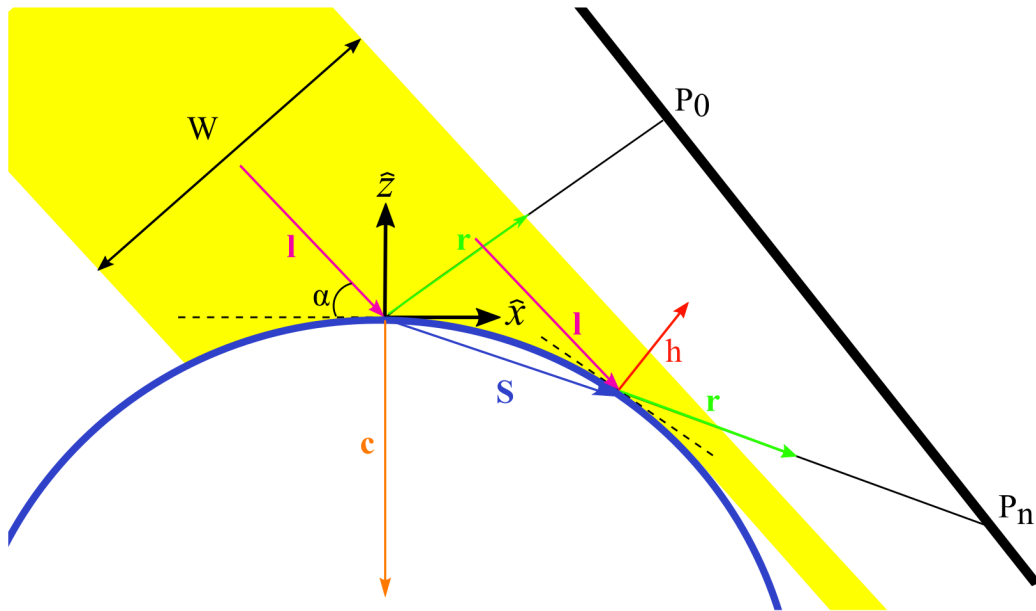


Figure 5.9: The vectors used in this model are exposed. The apex of the circle is the origin of the coordinate system, vector \vec{c} points to the circle center, vector \vec{S} points on the circle points, and \vec{h} is normal to the surface at this point. \vec{l} is the direction of the incoming ray (yellow rectangle) that is formed by a number of infinitesimal lines. The lines are then reflected, and \vec{r} is the direction of the reflection. The reflected line intersects the detector in P_n .

the sample surface is a circle of equation $\| \vec{x} - \vec{c} \|^2 = R_d^2$, where \vec{c} is the vector of the center of the sphere. The interception point between the lines and the point of the circle \vec{S} are calculated substituting:

$$t = -(\vec{a} \cdot \vec{d}) - \sqrt{(\vec{a} - \vec{d})^2 - (\vec{a}^2 - R_d^2)} \quad (5.17)$$

to 5.16. In Equation 5.17, $\vec{a} = \vec{l} - \vec{c}$.

The direction of the reflected beam can be obtained from the equation: $\vec{r} = \vec{l} - 2(\vec{h} \cdot \vec{l})\vec{h}$ where \vec{h} is the vector normal to the sphere in the point \vec{S} and it is calculated as: $\vec{h} = (\vec{S} - \vec{c})/R_d$. The equation of the reflected beam is therefore: $\vec{r} + v\vec{S}$.

The reflected beam then intercepts the detector, represented in the simulation with a line. The equation of the detector line is:

$$D = \begin{pmatrix} L \cos(\alpha) \\ L \sin(\alpha) \end{pmatrix} + w \begin{pmatrix} \cos(\frac{\pi}{2} - \alpha) \\ -\sin(\frac{\pi}{2} - \alpha) \end{pmatrix} \quad (5.18)$$

where L is the distance between the detector line and the center of the axis. The detector rotates around the origin of $\beta = \alpha$. The intercepting points between the reflected line and D are called P_n .

The detector is made by pixels, in order to simulate them, two transformations (rotation of β and translation) are applied in order to move \hat{x}, \hat{z} into the central pixel.

$$TrR_t \begin{pmatrix} \hat{x} \\ \hat{z} \end{pmatrix} = \begin{pmatrix} 0 & L \cos(\alpha) \\ 0 & L \sin(\alpha) \end{pmatrix} \begin{pmatrix} \cos(\alpha) & -\sin(\alpha) \\ \sin(\alpha) & \cos(\alpha) \end{pmatrix} \begin{pmatrix} \hat{x} \\ \hat{z} \end{pmatrix} = \begin{pmatrix} \tilde{x} \\ \tilde{z} \end{pmatrix} \quad (5.19)$$

These transformations are applied to P_n : $TrR_t P_n = \tilde{P}_n$. The advantage of the transformations is that the analysis can proceed using one coordinate instead of two because in new coordinates $\tilde{x} = 0$. The pixel number i that the reflected ray hits is, therefore:

$$i = \left\lfloor \frac{\tilde{P}_n}{psz} \right\rfloor \quad (5.20)$$

where psz is the pixel size and $\lfloor \rfloor$ are the symbols of rounding down.

The last step is to derive the reflectivity value for each ray and to sum those hitting the same pixel i . For each line, the reflectivity ($R(\alpha_l)$) was calculated

using the Fresnel equation described in Section 2.29 for copper. The local incident angle α_l is calculated in this way:

$$\alpha_l = \frac{\pi}{2} + \arccos(\vec{h} \cdot \vec{l}) \quad (5.21)$$

The final intensity value for each pixel is therefore:

$$I_i = \sum R_{i,n}(\alpha_l) \quad (5.22)$$

where $R_{i,n}(\alpha_l)$ is the reflectivity value of the line n that intercepts the pixel i .

5.5 Results and discussion

The validity and limitations of the ROI method and the reconstruction method were tested with simulated data. The simulation was done using the parameter values used in real experiments:

- Sample-detector distance 1 m
- pixels size 55 μm
- beam size 50 μm

The first attempt to extract the XRR from the simulation data was made using the ROI method. Figure 5.10.a shows the results of the reflectivity curves obtained with different sample radius. The reflectivity curves show a strong deviation with respect to the data obtained on the flat surface at lower q_z . The curves, as a matter of fact, have a plateau at lower values with respect to the plateau of the flat surface, but it is extended above the q_c . After this aberration, the curves of the bent surface approach the flat surface one. The nature of the error is related to the fact that the beam does not touch the entire sample at a small angle. In Figure 5.10.a, the simulated data, with $R_d = 200$ mm, are displayed in a 2D plot pixel vs q_z (the color scale represents the reflectivity). Already from the data, it is evident that, at small q_z , the signal is not symmetric. When only a section of the beam impinges on the surface, a part of the reflection is lost; the fan of angles that the beam experiences due to the curvature of the sample starts from value 0 to a higher one. The α_l lower than the q_c produces an intense reflection

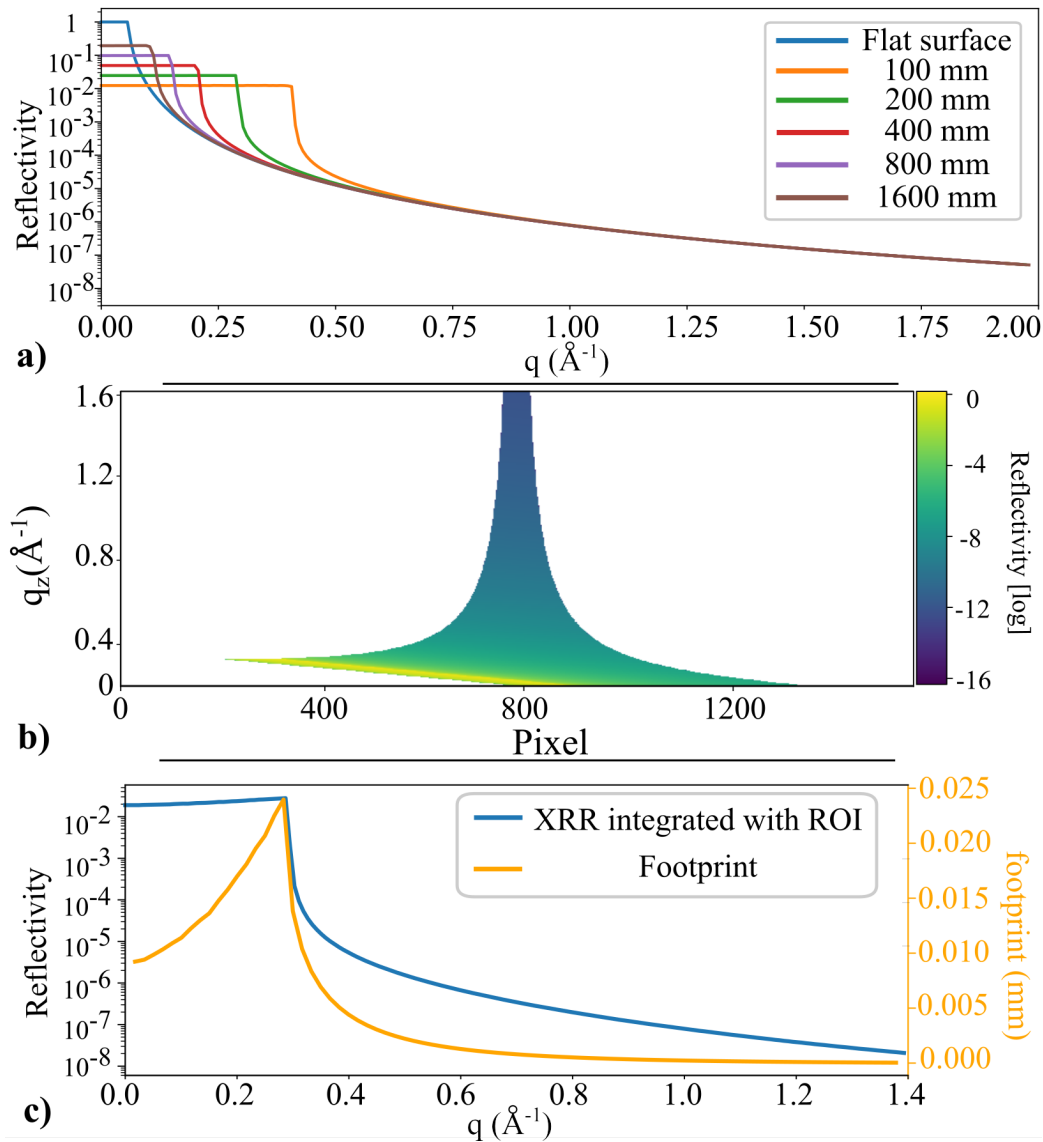


Figure 5.10: a) results of a simulation of reflectivity on copper with different radius of curvature. The data shows a plateau region at higher q_z and a lower intensity respect to the theoretical one, then it quickly decrease to reach the theoretical values. b) 2D plot pixel vs q_z of the simulated data with $R_d = 200$ mm. The color ramp represent the reflectivity values in log scale. c) The end of the plateau region is along with the peak of footprint and depend on $\frac{W}{2R}$ (see Formula 5.23).

(pixels colored in yellow in Figure 5.10.b) that continues until all the beam is on the sample.

5.10.b shows the length of the beam footprint and the x-ray reflectivity data. The footprint length increases with the increasing of q_z until it reaches a maximum, then it quickly decreases, approaching asymptotically the beam size. In order to understand this trend, it is useful to ideally divide the beam into two equal parts parallel to \vec{l} , from the center of the beam. At $\alpha = 0$, only the lower part of the beam touches the surface, the upper part is lost. With the increase of the angle, a bigger part of the upper beam starts to intercept the sample. For this reason, the beam size increases. When the whole upper part touches the sample, there is a maximum in the footprint length. It can be demonstrated that in Equation 5.8a, Δz is also equal to the portion of the upper beam that touches the sample. The maximum of the footprint can be therefore found substituting $W/2$ to Δz , the result is:

$$\alpha_{limit} = \arccos \left(1 - \frac{W}{2R} \right) \quad (5.23)$$

Above α_{limit} , the footprint becomes smaller, reaching asymptotically the beamsize.

When the upper part of the beam does not touch the sample completely, the fan of the local incident angle goes from 0 to higher values. The intensity contribution coming from the low α_l is much more important than the one at higher because, as discussed in Section 2.2, the reflectivity scales with q_z^4 . The contribution coming from the low local angle covers the one at a high angle. This is the reason for a constant plateau in the ROI method, the fact that the intensity of the plateau indirectly proportional to the radius of the sample is because, at low R, the spreading of the beam is higher and a lower portion of α_l is at low values respect to high R. The end of the plateau coincides with α_{limit} , then the spreading of the beam becomes smaller, and the values are similar to the one of the flat surface.

The method described in Section 5.3 however does not present this limitations. The results of the method applied to the simulated data with different radius are perfectly matching the results of the flat surface, as shown in Figure 5.11. In order to test the flexibility of the method, the results were also tested with different pixel sizes, different sample detector distance, and different beam sizes, and the reconstructed signal always matches with the flat surface one.

If the spreading of the beam is larger than the detector, a portion of the re-

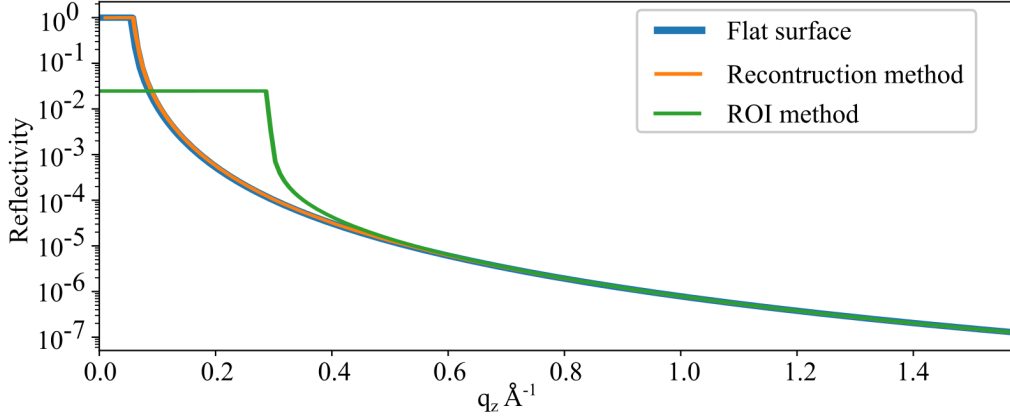


Figure 5.11: Differences between the XRR curves of the data showed in Figure 5.10.b extracted with the ROI method and with the reconstruction method.

flected beam is lost. This is a serious issue for a surface with high curvature, and it might make the analysis of the data impossible. The reconstruction method can also extract the reflectivity plot in these circumstances as shown in Figure 5.12.a. If the step of the scan is sufficiently small, in fact, the values of the pixel intensity at q_z , cut in one image, are detected in the next ones. The information on the reflectivity, therefore, is not lost.

The misalignment factors are another problem that can affect the measurements. The alignment of the beam of the apex of the sample surface is a complex and difficult procedure, and it is described in Section 6.1. If the alignment is not perfect, the center of the beam is not impinging on the apex of the sphere. If the center of the beam is intersecting the sphere at $\hat{x} > 0$, the entire beam will intersect the sphere at $\alpha > \alpha_{limit}$, *vice versa* if the center of the beam touches the sample at $\hat{x} < 0$, the $\alpha < \alpha_{limit}$. The data were, consequently, simulated with a positive and a negative shift of the center of the beam, as shown in Figure 5.12.b and 5.12.c. Also in this case, the XRR curves obtained with the reconstructed signal method are matching the one of the flat surfaces.

Finally, the incident beam from the synchrotron does not have a uniform intensity, but its intensity follows the Gaussian distribution. The effect of a Gaussian beam with $FWHM = W/2$ is shown in Figure 5.12.d. Without any correction factors, the extracted curve is approaching the one of the flat surfaces with high accuracy.

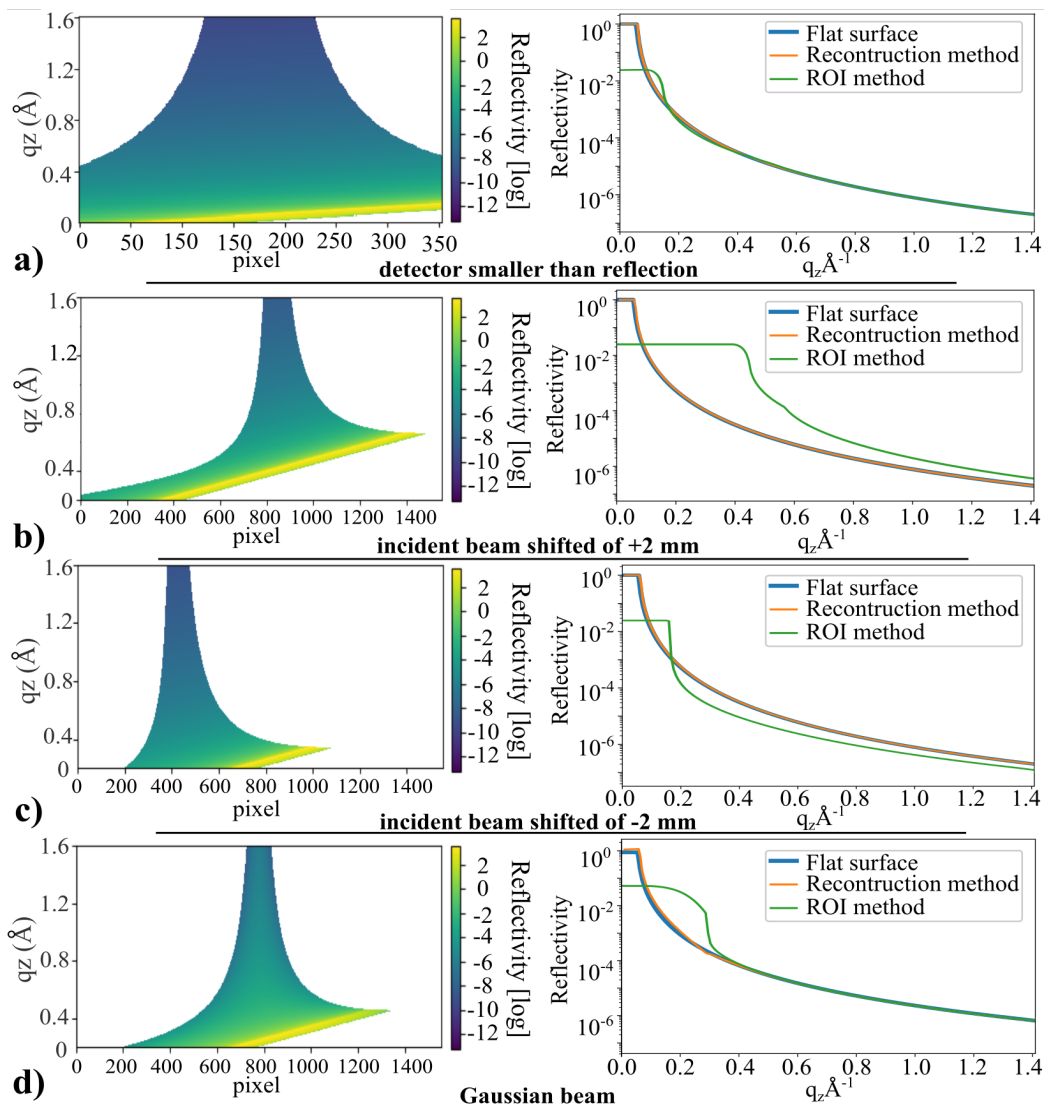


Figure 5.12: Data simulated with a smaller detector with respect to the length of the spreading of the beam. Data simulated with a positive b) and a negative c) shift of the beam with respect to the apex of the circle of 2 mm. d) data simulated with a Gaussian beam. The reconstruction method can retrieve the reflectivity curves for each of these cases.

5.6 Conclusions

The analysis of XRR data is well established when sample surfaces are flat. If the sample is convex, the beam is spreading, and the incident angle cannot unequivocally be defined. The classical procedure to extract the reflectivity value from the images relies on ROIs, in which the intensity values are integrated. In this work, it is demonstrated that this method provides aberrations at low angles for bent surfaces, and a new approach was proposed. In the method described, a value of reflectivity and q_z is calculated for each pixel of the detector image, then all the reflectivity in the same q_z are averaged. To test the reliability of this method, the experiment was simulated, and, using different parameters, the reconstructed XRR curve always match one of the flat surfaces. Surprisingly, the method is not strongly affected by beam misalignment or by a partial loss of data due to a reflection bigger than the detector size. This approach was, therefore, used to analyze the experimental results in Chapter 6.

Chapter 6

In situ X-ray study on LMCat

6.1 Introduction

The goal of the LMCat project is to characterize the growth of graphene on liquid metals *in situ*. The radiation mode optical microscope described in Chapter 4 gives interesting information about the system at the microscopic scale. The x-ray scattering techniques are, in this sense, essential because they provide complementary information at the atomic scale. The stress of the film, as well as the number of layers forming the crystal, are critical information for a complete characterization of the growth process. The x-ray techniques can provide this information *in situ* inside the controlled environment of the reactor.

The experiments were done in four different synchrotrons: ESRF (Grenoble, France), SOLEIL (Paris, France), DIAMOND (Didcot, UK), and PETRA III (Hamburg, Germany) and at different beamlines. The results of the experiments are in agreement, attesting to the correct reproducibility of the measurements.

The techniques used are x-ray reflectivity (XRR) and grazing incident x-ray diffraction (GIXD). The reflectivity measurements are needed to measure the out-of-plane density profile and so to have information on the number of layers and the roughness of the graphene produced. GIXD is useful to get the lattice parameter of the graphene crystals and to detect the average transversal fluctuations of the membrane. From this study, it is possible to assert that the graphene produced is a monolayer, that its roughness is low, and that the flatness is high.

6.2 Alignment of the x-ray beam on a convex surface

The alignment of the sample is a crucial point for the success of the measurement, and it is the same for both techniques. The alignment on the sample must guarantee that the beam impinges on the top of the convex surface. Assuming that the axes of the alignment are on the apex of the sample surface: the incident beam is on the $\hat{x} - \hat{z}$ plane, and the \hat{y} -axis is orthogonal to it. Once the reactor is set on the diffractometer, it must be possible to shift the sample in \hat{x} , \hat{y} , and \hat{z} -direction, and to rotate it around those axes. For this reason, the alignment procedure described below, needs to be done on a multi-motorized stage. The alignment procedure consists of three steps, and the direct beam must be parallel to the plane of alignment. The steps are:

1. **alignment in z:** Once the reactor is set, the beam can be totally covered by the sample, or the beam can be far above it, and directly shine on the detector. The first step of the alignment consists of adjusting the vertical position respect to the beam. To do that, a “ \hat{z} -scan” must be done. In the \hat{z} -scan, the reactor is first shifted down, and then it is progressively translated upwards. At every motion step, the intensity value of the beam is recorded. When the sample is below the beam, the intensity has maximum values; when it covers it, the intensity drop to 0. The classical shape of the \hat{z} -scan is an error function, as shown in Figure 6.1.a. The sample position is set on the flex point; in this way, the majority of the beam covers the sample.
2. **scans in x and y:** In order to find the apex of the sample, two stages were applied, one after the other. The first stage takes advantage of the fact that the sample holder is a cylindrical symmetric disc, and the apex of the drop is roughly in the middle. The sample is translated on \hat{y} (direction perpendicular to the beam) by a distance higher than the radius of the object. Then a scan is performed on \hat{y} , at every step of the scan, the sample was shifted, and the intensity of the beam was recorded. When the beam is on the side of the sample, the beam does not impinge on the object, and the intensity is high; when the beam touches it, it is partially covered, and the intensity drops. The shape of the intensity recorded is shown in Figure 6.1.b. At the end of the scan, the sample is moved to the center of the minimum position (the

center of the disk). Then the sample is rotated of 90° on the \hat{z} axis, and the same procedure is done on the \hat{x} axis.

The sample, however, can have a complex shape, and the apex of the copper drop could not be in the center of the disk. Another stage of alignment on \hat{x} and \hat{y} is needed to precisely find the higher point of the droplet. The sample is rotated again of 90° on the \hat{z} axis in order to come back to the initial configuration (\hat{y} orthogonal to the direct beam plane). Then the incident angle α , and the angle of the detector γ , are both set to 0.8° . If the beam is not on the apex, the reflected beam came as a tilted line, as shown in Figure 6.1.c. The sample is moved on \hat{y} until the reflected beam is perpendicular to the surface plane. Then the sample is rotated 90° on the \hat{z} axis, and the procedure is done on the \hat{x} axis.

- 3. scanning the tilt in x and y:** To align the tilts, α must be at 0° and \hat{y} is orthogonal to the incident beam plane (initial configuration). The sample is rotated around the \hat{y} axis, and the intensity of the beam is recorded. When the sample is highly tilted, the beam is attenuated, and the intensity on the detector is lower; *vice versa*, when the sample is leveled to the beam, a bigger part of the beam can pass. The shape of the scan is the convolution of the beam shape with the shape of the sample, and it is shown in Figure 6.1.d. At the end of the scan, the sample must be tilted on the position corresponding to the peak of the scan. After the \hat{y} tilt is aligned, the sample is rotated of 90° respect to \hat{z} , and the same procedure is done on the \hat{x} axis.

6.3 Grazing incident x-ray diffraction

The GIXD measurements were done at different synchrotrons, with different fluxes and beam sizes; however, the approaches to detect the 2D RODs were the same in all the experiments. The grazing incident angle was set at $\sim 80\%$ of the critical angle for total external reflection of the Cu, and the sample detector distance was ~ 1 m (the exact position depended on the beamline). The surface of the sample was always monitored in real-time with the optical microscope. For this reason, the number of the flakes and the percentage of coverage of the Cu surface were known. In order to diffract, the graphene crystals must be perfectly aligned with the beam. The main problem with

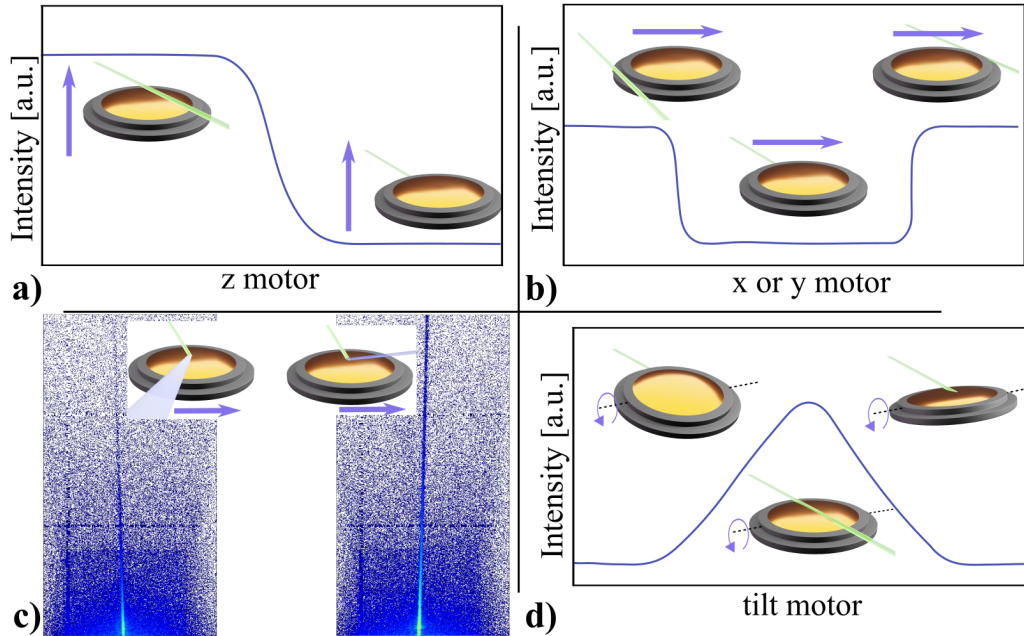


Figure 6.1: The steps for the alignment of the sample are shown in these images; the plots represent the intensity of the beam on the detector, the insets are the graphical representation of the position of the ray with respect to the sample. The purple arrows represent the direction of the movement of the sample. a) The first step is the vertical translation scan; it is done to find the sample position with respect to the beam. The sample is then moved to a position corresponding to a value of the the flex. b) The sample is slid perpendicularly to the beam. If the sample does not touch the beam, the intensity is higher; if *vice versa*, it intersects the beam, the intensity decreases, as shown in the figure. The sample is then moved to the center of the minimum (\sim center of the surface). c) The incident angle is set to 0.8° , and the sample is shifted perpendicularly to the beam. If the beam is not in the center of the droplet, the reflected beam is tilted, as shown in the figure. This measurement is done to precisely set the position in \hat{x} and \hat{y} . d) The sample is rotated around the axis perpendicular to the beam. When the sample is tilted, the intensity of the beam is low, however then the sample is leveled, a maximum of intensity is found.

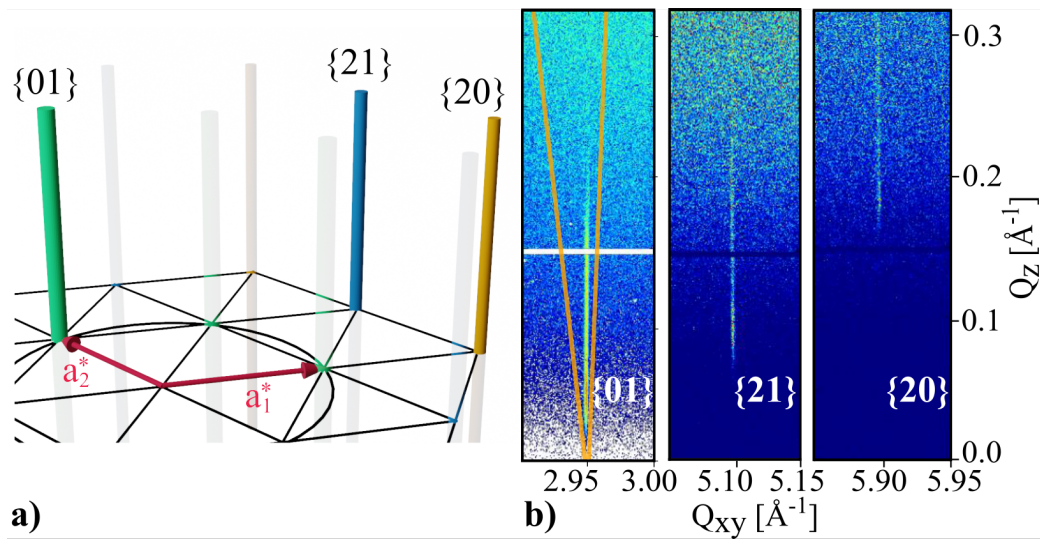


Figure 6.2: a) Graphical representation of the reciprocal space of graphene. The 2D RODs $\{01\}$, $\{21\}$ and $\{20\}$ are displayed with a green, blue and yellow cylinders respectively. b) The detector images of the three 2D ROD families. The orange lines on the $\{01\}$ 2D RODs are the FWHM of the Bragg rod of the free-standing graphene reported in literature[126].

crystals floating on the liquid is that they move and rotate, and the achievement of the stationary Bragg condition is not as easy as on a solid. Two strategies were used to detect the Bragg rods: the first one takes advantage of the rotations of the flakes in the initial stage of the growth. The detector is moved where the diffracted beam of a given graphene reflection is expected to be, and it starts to acquire one image per second with no time gap between images. In the meantime, the sample is shined with the x-rays and, when rotating flakes are oriented following to the Bragg condition for an atomic plane, the diffraction signal hits the detector. The second way was done after the complete coverage of the surface. When the layer is closed, the film can move a little, but, mostly, it is anchored by its sides. Also, in this case, the detector is put in the q_{xy} in which the diffraction is supposed to be; however, now, the reactor itself is rotated around the azimuthal axis.

The reciprocal space lattice of graphene was described in Section 1.1.1 and it is shown in Figure 6.2.a. The 2D ROD of the graphene crystal, detected for the first time on the liquid copper, are of the $\{10\}$, $\{21\}$ and $\{20\}$ families. Figure 6.2.b shows the streaks correspond to the intersection of the Ewald's sphere with the rods of graphene. The streaks in Figure were obtained at ID10 beamline at ESRF, with a monochromatic beam of 22 keV, a beamsize of $13 \times 250 \mu\text{m}^2$ VxH and a Maxipix CdTe detector with pixels size of $55 \mu\text{m}$. The lattice parameter found was $2.4601 \pm 0.0005 \text{ \AA}$ at 1370K. The lattice parameter of graphene at room temperature is 2.46 \AA [94], suggesting a negligible expansion coefficient at these conditions.

From the increase of the FWHM of the RODs with q_z , it is possible to have information on the average rippling of the layer[126, 127, 128]. Already from Figure 6.2.b it is possible to notice that the 2D RODs remain quite sharp even at high q_z , the evolution of the FWHM of the rods reported from Meyer *et al.* for a free-standing graphene is illustrated for comparison on the 2D ROD $\{01\}$ of the Figure 6.2.b[126]. The ripples of the free-standing graphene spontaneously appear due to thermal fluctuations[129], however the substrate can strongly reduce their amplitude[130, 131]. The value of roughness of the graphene on liquid copper was measured with XRR and discussed in Section 6.4.

An accurate analysis of the 2D RODs behavior with q_z , was performed on the data obtained at P08 beamline of Petra III; the photon energy and the photon flux were respectively 18 keV and $2.8 \cdot 10^{12}$ ph/s. The beamsize was $40 \times 200 \mu\text{m}$, and a Medipix3-based detector (lambda) was used.

The measurements were done on a closed layer. In order to detect the 2D

ROD broadening at high q_z , the detector was placed at $q_{xy} = 2.9491\text{\AA}^{-1}$, and the sample was rotated around its azimuthal plane with steps of 0.01° . Once the rod was found, the rotation was stopped and restarted with smaller steps (0.004°) around the previous position. In this way, the Ewald's sphere intercepted the 2D ROD at different heights for different azimuthal rotations. Figure 6.3.a shows the images of streak of the same rod at different positions of the azimuthal rotation. The streaks were analyzed dividing the detector images in perpendicular stripes of $330\ \mu\text{m}$ thickness (6 pixels), then the intensity was summed column by column. The resulting projected intensity was fitted with a Gaussian function. The FWHM of the Gaussian functions as well as the position of the maximum are shown in Figure 6.3.b, and 6.3.c respectively. From the FWHM of the 2D RODs, the structurally-coherent domain of the crystal was calculated as $2\ \mu\text{m}$.

6.4 X-ray reflectivity

The XRR measurements were done at P08 beamline in Petra III, I07 in Diamond, and at Sirius beamlines in SOLEIL. The first two beamlines featured a set of double crystals deflectors (DCD): the incident beam was deviated downwards by the DCD, and the reflection was recorded moving the detector at an angle $\beta = \alpha$. In Sirius, where the DCD was not present, the beam was parallel to the surface plane of the sample, and the reactor itself was tilted around the axis perpendicular to the beam. This is possible because the thickness of the liquid film is $\sim 70\ \mu\text{m}$ (lower than the capillary length of Cu $4.09\ \text{mm}$), and the puddle is confined in the rough part of the sample holder (see Section 3.2.2). The liquid is, therefore, not affected by gravity. This means that, if the sample is tilted, the liquid does not change its shape. The detector was set to β two times higher than the tilting angle, in a $\theta - 2\theta$ configuration. The flux, beamsize, photon energy, and detector used in each beamline are listed in Section 3.3.3. The characterization was done on the bare liquid copper and on the graphene on the liquid copper after complete coverage of the surface.

The shape of the apex of a drop can be well approximated by a sphere[132, 133]. The XRR curves can be, therefore, extracted with the procedure described in Chapter 5, and the data were fitted with the REFL1D program[134]. The REFL1D program requires: the XRR data, an initial slab

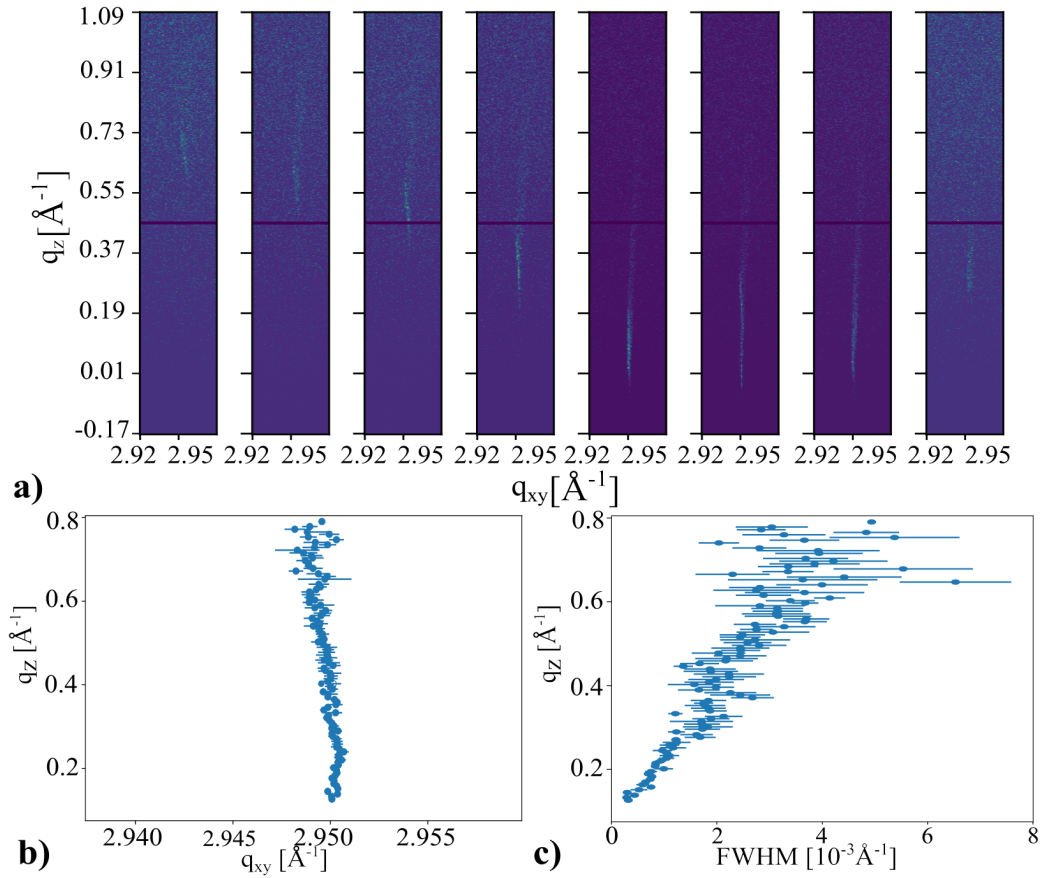


Figure 6.3: The region of 2D ROD that can be detected is the one intersecting the Ewald sphere. The azimuthal rotation of the sample corresponds to a relative movement of the diffraction rod with respect to the Ewald sphere. For this reason, the different azimuthal rotation of the sample corresponds to different parts of 2D ROD detected at different q_z . In order to measure the 2D ROD at high q_z , therefore, the sample was rotated on the z-axis by very small steps. a) The $\{01\}$ 2D ROD on the Lambda detector of the PO8 beamline at PETRA III. The images differ from the next ones because the sample was rotated by 0.002° between two images. The images were divided into perpendicular slices and projected; the profile was fitted with a Gaussian function. b) The q_{xy} position of the peak of the Gaussian function respect to q_z c) The full-width half maximum of the Gaussian function respect to q_z .

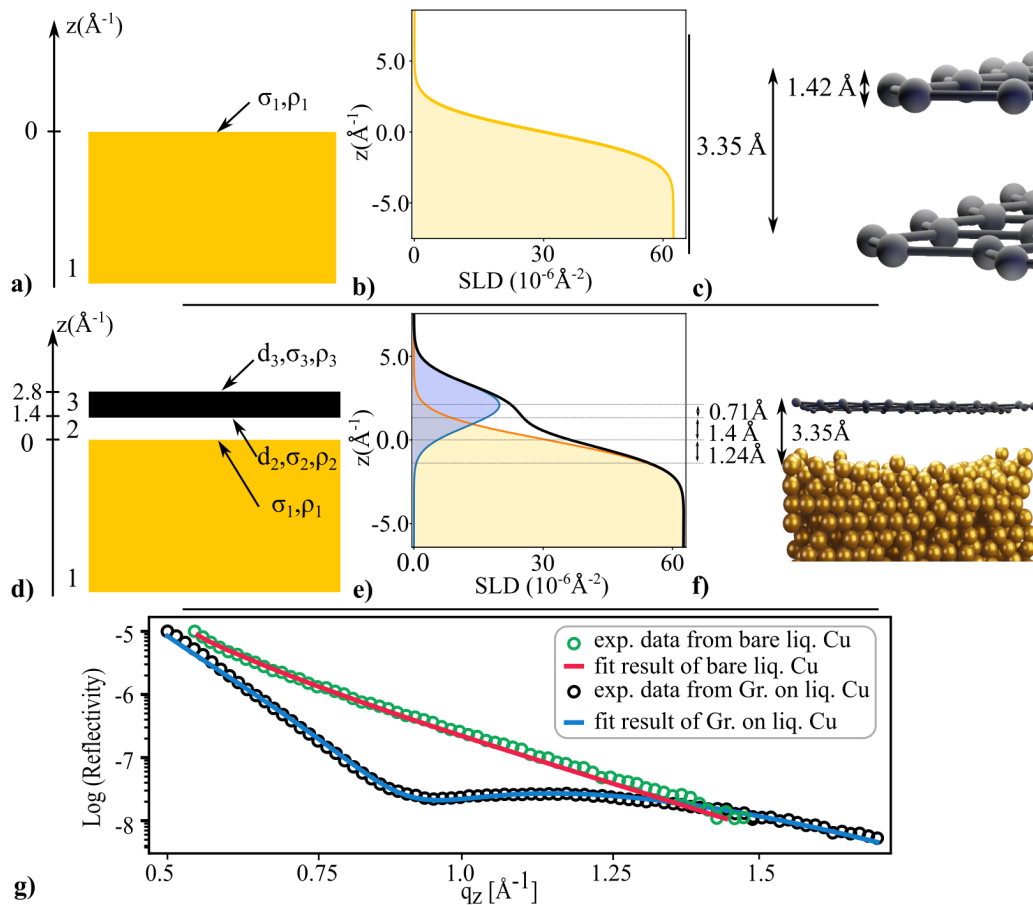


Figure 6.4: a) Slab model of the electron density profile of the liquid copper b) Electron density profile of the copper, result of the fit of the XRR data c) The distance between two carbon layers in graphite is 3.35\AA , while the diameter of the carbon atom is 1.42\AA . d) Slab model of the electron density profile of the liquid copper and the graphene. e) Electron density profile of the graphene on copper, result of the fit of the XRR data f) graphical representation of the separation gap between graphene and the copper. g) The XRR curves of graphene on liquid copper and of bare graphene.

model of the density profile of the sample, and the range of the values of the fitting parameters of the model. The interfaces between two layers of the model are simulated as an error function, as described in Section 2.2.2. The algorithm in the program recursively modifies the free parameters of the density profile, and, from the new one, it creates a simulated XRR curve. Using a least squares regression approach, the simulated data was calculated until they match the experimental one. The scattering length density (SLD) in the out-of-plane direction is the output of the program. In all the simulation described below, the scaling factor (in Formula 2.32) was let free to vary on a wide range.

The first results described are the ones of the bare liquid copper. The model adopted presents only the copper slab, as shown in Figure 6.4.a. In order to fit the data, the density of the liquid Cu was fixed to 7.99 g/cm^3 [135], while the roughness of the Cu σ_1 was varied between 0 and 5 Å. The results for the different beamlines are shown below:

Beamline	Cu roughness
P08	1.4 ± 0.3
I07	1.4 ± 0.2
Sirius	1.60 ± 0.3

Table 6.1: The table shows the results from the fitting of the XRR curves of liquid copper.

The average value is $1.5 \pm 0.2 \text{ Å}$ and the SLD profile is shown in Figure 6.4.b. This result may be surprising because the roughness caused by the capillary waves and calculated in Section 1.3.1 at $T=1400\text{K}$ is 2.53 Å . This discrepancy can be explained with the following discussion: the Formula 1.9 requires the short and the long-wavelength cut-off (q_{max} and q_{min} respectively). The short wavelength cut-off depends on the atomic radius; the long-wavelength cut-off is normally set to the capillary wave cut-off. O.Shpyrko *et al.* however proved that the instrumental resolution in the reciprocal space Δq_y^{res} determines the experimental q_{min} [136]. In order to take into account the resolution effect, the Δq_y^{res} must substitute the q_{min} in Formula 1.9. The resolution is given by the pixel size, therefore, following the modified formula, the results of the Cu roughness is 1.64 Å and 1.72 Å for P08, and I07 and Sirius respectively, in agreement with the fit.

The XRR measurements of graphene on the top of the liquid copper was

done when the layer of graphene was covering the surface of the copper completely. The advancement of the growth was checked with the optical microscope, and the XRR characterization was started minutes after the graphene covered completely the area that the OM could observe, to confirm that the growth was finished.

The model used to fit the XRR data uses three slabs: the first one is the liquid copper, the second one is the separation gap, and the last one is the layer of carbon atoms, as shown in Figure 6.4.d. In order to fit the data, four parameters of the model were fixed, and three were fitted. The fixed parameters were the density of the liquid copper (7.99 g/cm³[135]), the density of the separation gap (0 g/cm³), and the density of the carbon layer. The density of the carbon layer, in particular, was derived from the graphite one (2.24 g/cm³[137]). The graphite structure can be thought of as a stack of graphite sheet one on top of the other; the distance between the center of the atoms layers is 3.35 Å[138], while the carbon atom diameter is 1.42 Å[139], as shown in Figure 6.4.c. The lower volume of the single carbon atom layer with respect to the graphite one must be taken into account for the calculation of its density. The density is, therefore:

$$\frac{3.35[\text{Å}]}{1.42[\text{Å}]} \cdot 2.24[\text{g/cm}^3] = 5.36[\text{g/cm}^3] \quad (6.1)$$

The three fitted parameters were: the roughness of copper σ_1 , the thickness of the separation gap d_2 and the roughness of the interface layer and the carbon layer, (σ_2 and σ_3) respectively; the last two variables were constrained to have the same value. The slab model is shown in Figure 6.2, while the results of the fit for the different synchrotrons are shown in Table 6.2.

Beamline	Cu roughness	C roughness	Separation gap
P08	1.2 ± 0.1	1.2 ± 0.1	1.4 ± 0.2
I07	1.3 ± 0.2	1.3 ± 0.1	1.5 ± 0.2
Sirius	1.3 ± 0.2	1.2 ± 0.2	1.4 ± 0.3

Table 6.2: The table shows the results from the fitting of the XRR curves of graphene on liquid copper.

The density profile resulting from the fit is shown in Figure 6.2.e. The roughness of graphene is a few orders of magnitude lower than the found

in literature and grown on solid[140, 141, 142]. Furthermore, the roughness of graphene is similar to the one of copper, suggesting that the graphene is conformal to the majority of the capillary wave spectrum of the liquid copper[143, 144].

From the slab model adopted, it is possible to derive the van der Waals distance between the graphene and the liquid copper. The van der Waals distance is the distance between the center of the atoms of two contiguous layers. The slab model does not give this value directly, but it must be interpreted. As shown in Figure 6.4.e the distance between the center of the carbon atom and the flex point of the position of the C-gap interface is 0.71, the thickness of the separation gap is 1.4 Å, to find the center of the Cu atom, we need to add σ_1 . The van der Waals distance is therefore 3.35 Å, as shown in Figure 6.2.f; the XRR data for both copper and copper-graphene and the fitting values are shown in Figure 6.2.g. The van der Waals distance of solid Cu(111) and graphene found in literature was theoretically predicted as calculated as ~ 3.3 Å[145, 146, 147, 148, 149] and experimentally measured as ~ 3.34 Å[150]. The fact that the van der Waals distance of the liquid copper is comparable to the one of solid copper is probably due to the fact that their binding energy is similar.

The position of the copper atoms, for the calculation of the separation gap, could be obtained more precisely using the surface layering model[75]. This model is used to describe the atomic layers that are formed on the surface of a liquid. The out-of-plane density profile of each layer is a Gaussian function around an idealized point $z = -jd$, with j the layer number from the interface, and d the spacing between layers. The variance of each Gaussian function increases linearly with j . The SLD of the liquid is the sum of the density profile of each layer. The advantage of the surface layering model is that the average position of the first layer of liquid atoms ($j = 1$) can be easily calculated. The problem is that it is significant if the surface layering peak is detected, and on copper, it is above 3 \AA^{-1} , far from the measurement range. In future works, it will be tried to increase the range of the XRR scan and to use this model.

6.5 Conclusion

The graphene grown on liquid copper was studied for the first time *in situ* with the x-ray scattering techniques. The lattice parameter of the graphene was measured with high precision ($2.4601 \pm 0.0005 \text{ \AA}$), and it is remarkably similar to the one of graphene at room temperature found in literature.

The XRR allow to conclude that the graphene is mono-layer on average, also confirmed with the GIXD study of the rods in q_z , that do not present oscillation caused by an out-of-plane order. The 2D RODs, in particular, do not widen significantly with the increasing of q_z , meaning that the graphene present a lower roughness respect to the free-standing one[126]. The low roughness of the graphene is measured with the XRR and it is 1.23 \AA on average. The distance between the copper and the graphene atoms is 3.35 \AA , comparable to the one of solid copper.

Chapter 7

Conclusions

The liquid metals have the perfect surface to grow graphene with the CVD techniques. The smoothness and uniformity of the film guarantee low nucleation points; the non-crystalline position of the atoms of the liquid avoids that the material grow with preferential orientations. The papers that can be found in the literature, the characterizations were done after the re-solidification of the liquid surface.

The project of this thesis work aimed to measure the growth of graphene on liquid copper *in situ*, using a prototype of a reactor that allows x-ray scattering techniques and optical microscopy.

The optical microscope was an extremely useful tool that gives a lot of information about the dynamics of the growth, the shape of the flake, the number of impurity particles, etc. Having feedback of the surface status helped to tune the partial pressure of the gases to create a graphene flake of > 2 mm. The low nucleation points can be easily increased by pulsing the partial pressure of methane.

Another fascinating phenomenon that was observed with the optical microscope was the self-alignment of the flakes, results of long-distance attraction forces due to capillary waves and low distance repulsion due to electrostatics.

The x-ray scattering techniques were never used to measure graphene on liquid copper. One of the major issues found was the concave shape of the sample surface for the XRR measurements. The classic ROI method for data extraction gives aberrations that were studied in detail with simulated data. A new method for the data extraction was created and presented, and it allows to measure XRR of bent surface in a $\theta - 2\theta$ configuration.

From the XRR measurements, the graphene roughness was measured at 1.23 Å, while the van der Waals distance was 3.35 Å. With the GIXD measurements, the graphene diffraction rods were detected. The lattice parameter of the graphene was found at 2.4601 Å, the spreading of the rods is limited in q_z , symptomatic of a low roughness of the material.

Bibliography

- [1] Edward L Wolf. *Graphene: a new paradigm in condensed matter and device physics*. OUP Oxford, 2013.
- [2] Matthew J Allen, Vincent C Tung, and Richard B Kaner. “Honeycomb carbon: a review of graphene”. In: *Chemical reviews* 110.1 (2010), pp. 132–145.
- [3] Charles Kittel, Paul McEuen, and Paul McEuen. *Introduction to solid state physics*. Vol. 8. Wiley New York, 1996.
- [4] Christian Schäonenberger. “Bandstructure of graphene and carbon nanotubes: An exercise in condensed matter physics”. In: *Lectures and exercises Nanoelectronics group of the University of Basel* (2000).
- [5] Kirill I Bolotin et al. “Ultrahigh electron mobility in suspended graphene”. In: *Solid state communications* 146.9-10 (2008), pp. 351–355.
- [6] Roberto Muñoz and Cristina Gómez-Aleixandre. “Review of CVD synthesis of graphene”. In: *Chemical Vapor Deposition* 19.10-11-12 (2013), pp. 297–322.
- [7] Cecilia Mattevi, Hokwon Kim, and Manish Chhowalla. “A review of chemical vapour deposition of graphene on copper”. In: *Journal of Materials Chemistry* 21.10 (2011), pp. 3324–3334.
- [8] H Tetlow et al. “Growth of epitaxial graphene: Theory and experiment”. In: *Physics reports* 542.3 (2014), pp. 195–295.
- [9] Congqin Miao et al. “Chemical Vapor Deposition of Graphene”. In: *Physics and Applications of Graphene*. Ed. by Sergey Mikhailov. Rijeka: IntechOpen, 2011. Chap. 3.
- [10] Matthias Batzill. “The surface science of graphene: Metal interfaces, CVD synthesis, nanoribbons, chemical modifications, and defects”. In: *Surface Science Reports* 67.3-4 (2012), pp. 83–115.

- [11] Maria Losurdo et al. “Graphene CVD growth on copper and nickel: role of hydrogen in kinetics and structure”. In: *Physical Chemistry Chemical Physics* 13.46 (2011), pp. 20836–20843.
- [12] Grzegorz Gajewski and Chun-Wei Pao. “Ab initio calculations of the reaction pathways for methane decomposition over the Cu (111) surface”. In: *The Journal of chemical physics* 135.6 (2011), p. 064707.
- [13] Meicheng Li, Yingfeng Li, and Joseph Michel Mbengue. “DFT Investigations on the CVD Growth of Graphene”. In: *Surface Energy* (2015), p. 153.
- [14] Wenhua Zhang et al. “First-principles thermodynamics of graphene growth on Cu surfaces”. In: *The Journal of Physical Chemistry C* 115.36 (2011), pp. 17782–17787.
- [15] HoKwon Kim et al. “Modeling of the self-limited growth in catalytic chemical vapor deposition of graphene”. In: *New Journal of Physics* 15.5 (2013), p. 053012.
- [16] Kemal Celebi et al. “Evolutionary kinetics of graphene formation on copper”. In: *Nano letters* 13.3 (2013), pp. 967–974.
- [17] Yi Zhang et al. “Comparison of graphene growth on single-crystalline and polycrystalline Ni by chemical vapor deposition”. In: *The Journal of Physical Chemistry Letters* 1.20 (2010), pp. 3101–3107.
- [18] Xiuyun Zhang, Hui Li, and Feng Ding. “Self-Assembly of Carbon Atoms on Transition Metal Surfaces—Chemical Vapor Deposition Growth Mechanism of Graphene”. In: *Advanced Materials* 26.31 (2014), pp. 5488–5495.
- [19] Ramki Kalyanaraman. “Nucleation energetics during homogeneous solidification in elemental metallic liquids”. In: *Journal of Applied Physics* 104.3 (2008), p. 033506.
- [20] Johann Coraux et al. “Growth of graphene on Ir (111)”. In: *New Journal of Physics* 11.2 (2009), p. 023006.
- [21] Junfeng Gao et al. “Graphene nucleation on transition metal surface: structure transformation and role of the metal step edge”. In: *Journal of the American Chemical Society* 133.13 (2011), pp. 5009–5015.

- [22] Priyadarshini Ghosh et al. “Insights on defect-mediated heterogeneous nucleation of graphene on copper”. In: *The Journal of Physical Chemistry C* 119.5 (2015), pp. 2513–2522.
- [23] Bin Wang et al. “Effect of Cu substrate roughness on growth of graphene domains at atmospheric pressure”. In: *Materials Letters* 131 (2014), pp. 138–140.
- [24] Zhu-Jun Wang et al. “Stacking sequence and interlayer coupling in few-layer graphene revealed by in situ imaging”. In: *Nature communications* 7.1 (2016), pp. 1–12.
- [25] Chee Kwan Gan and David J Srolovitz. “First-principles study of graphene edge properties and flake shapes”. In: *Physical Review B* 81.12 (2010), p. 125445.
- [26] Zhengtang Luo et al. “Growth mechanism of hexagonal-shape graphene flakes with zigzag edges”. In: *Acs Nano* 5.11 (2011), pp. 9154–9160.
- [27] Bin Wu et al. “Self-organized graphene crystal patterns”. In: *NPG Asia Materials* 5.2 (2013), e36–e36.
- [28] Jichen Dong, Leining Zhang, and Feng Ding. “Kinetics of graphene and 2D materials growth”. In: *Advanced Materials* 31.9 (2019), p. 1801583.
- [29] Teng Ma et al. “Edge-controlled growth and kinetics of single-crystal graphene domains by chemical vapor deposition”. In: *Proceedings of the National Academy of Sciences* 110.51 (2013), pp. 20386–20391.
- [30] Wang Guo et al. “Rapid chemical vapor deposition of graphene on liquid copper”. In: *Synthetic Metals* 216 (2016), pp. 93–97.
- [31] Zhihong Zhang et al. “The way towards ultrafast growth of single-crystal graphene on copper”. In: *Advanced Science* 4.9 (2017), p. 1700087.
- [32] Shu Nie et al. “Origin of the mosaicity in graphene grown on Cu (111)”. In: *Physical Review B* 84.15 (2011), p. 155425.
- [33] Elena Loginova et al. “Evidence for graphene growth by C cluster attachment”. In: *New Journal of Physics* 10.9 (2008), p. 093026.
- [34] HoKwon Kim et al. “Activation energy paths for graphene nucleation and growth on Cu”. In: *ACS nano* 6.4 (2012), pp. 3614–3623.
- [35] Wei Guo et al. “Governing rule for dynamic formation of grain boundaries in grown graphene”. In: *ACS nano* 9.6 (2015), pp. 5792–5798.

- [36] Ivan Vlassiouk et al. “Graphene nucleation density on copper: fundamental role of background pressure”. In: *The Journal of Physical Chemistry C* 117.37 (2013), pp. 18919–18926.
- [37] Dechao Geng et al. “Controlled Growth of Single-Crystal Twelve-Pointed Graphene Grains on a Liquid Cu Surface”. In: *Advanced Materials* 26.37 (2014), pp. 6423–6429.
- [38] Esteban Meca et al. “Epitaxial graphene growth and shape dynamics on copper: phase-field modeling and experiments”. In: *Nano letters* 13.11 (2013), pp. 5692–5697.
- [39] Carlo M Orofeo et al. “Influence of Cu metal on the domain structure and carrier mobility in single-layer graphene”. In: *Carbon* 50.6 (2012), pp. 2189–2196.
- [40] Lifang Tan et al. “Design of catalytic substrates for uniform graphene films: from solid-metal to liquid-metal”. In: *Nanoscale* 7.20 (2015), pp. 9105–9121.
- [41] Jun-ichi Fujita et al. “Graphitization at interface between amorphous carbon and liquid gallium for fabricating large area graphene sheets”. In: *Journal of Vacuum Science & Technology B: Microelectronics and Nanometer Structures Processing, Measurement, and Phenomena* 27.6 (2009), pp. 3063–3066.
- [42] Jun-ichi Fujita et al. “Fabrication of large-area graphene using liquid gallium and its electrical properties”. In: *Japanese Journal of Applied Physics* 49.6S (2010), 06GC01.
- [43] Shaahin Amini et al. “Growth of large-area graphene films from metal-carbon melts”. In: *Journal of Applied Physics* 108.9 (2010), p. 094321.
- [44] Michael V Lee et al. “Controllable gallium melt-assisted interfacial graphene growth on silicon carbide”. In: *Diamond and related materials* 24 (2012), pp. 34–38.
- [45] Dechao Geng et al. “Uniform hexagonal graphene flakes and films grown on liquid copper surface”. In: *Proceedings of the National Academy of Sciences* 109.21 (2012), pp. 7992–7996.
- [46] Guqiao Ding et al. “Chemical vapor deposition of graphene on liquid metal catalysts”. In: *Carbon* 53 (2013), pp. 321–326.

- [47] A Mukanova et al. “CVD graphene growth on a surface of liquid gallium”. In: *Materials Today: Proceedings* 4.3 (2017), pp. 4548–4554.
- [48] Jun-ichi Fujita et al. “Near room temperature chemical vapor deposition of graphene with diluted methane and molten gallium catalyst”. In: *Scientific reports* 7.1 (2017), pp. 1–10.
- [49] Jiao Wang et al. “High-mobility graphene on liquid p-block elements by ultra-low-loss CVD growth”. In: *Scientific reports* 3 (2013), p. 2670.
- [50] Y Kasai et al. “Mass sensing using a virtual cantilever virtually coupled with a real cantilever”. In: *Applied Physics Letters* 115.6 (2019), p. 063103.
- [51] Ye Fan et al. “Crack-free growth and transfer of continuous monolayer graphene grown on melted copper”. In: *Chemistry of Materials* 26.17 (2014), pp. 4984–4991.
- [52] Chitengfei Zhang et al. “Growth of umbrella-like millimeter-scale single-crystalline graphene on liquid copper”. In: *Carbon* 150 (2019), pp. 356–362.
- [53] Shuting Zheng et al. “Insight into the rapid growth of graphene single crystals on liquid metal via chemical vapor deposition”. In: *Science China Materials* 62.8 (2019), pp. 1087–1095.
- [54] Jinxin Liu and Lei Fu. “Controllable growth of graphene on liquid surfaces”. In: *Advanced Materials* 31.9 (2019), p. 1800690.
- [55] Mengqi Zeng et al. “Liquid metal: an innovative solution to uniform graphene films”. In: *Chemistry of Materials* 26.12 (2014), pp. 3637–3643.
- [56] Chitengfei Zhang et al. “Synthesis of large size uniform single-crystalline trilayer graphene on premelting copper”. In: *Carbon* 122 (2017), pp. 352–360.
- [57] Dechao Geng et al. “Self-Aligned Single-Crystal Graphene Grains”. In: *Advanced Functional Materials* 24.12 (2014), pp. 1664–1670.
- [58] Mie Andersen, Juan Santiago Cingolani, and Karsten Reuter. “Ab initio thermodynamics of hydrocarbons relevant to graphene growth at solid and liquid Cu surfaces”. In: *The Journal of Physical Chemistry C* 123.36 (2019), pp. 22299–22310.

- [59] Hai-Bei Li et al. “Graphene nucleation on a surface-molten copper catalyst: quantum chemical molecular dynamics simulations”. In: *Chemical Science* 5.9 (2014), pp. 3493–3500.
- [60] P Kula et al. “High Strength Metallurgical Graphene—Mechanisms of Growth and Properties”. In: *Archives of Metallurgy and Materials* 60.4 (2015), pp. 2535–2542.
- [61] Jiao Wang et al. “Uniform graphene on liquid metal by chemical vapour deposition at reduced temperature”. In: *Carbon* 96 (2016), pp. 799–804.
- [62] Yi Zhang et al. “Anisotropic hydrogen etching of chemical vapor deposited graphene”. In: *ACS nano* 6.1 (2012), pp. 126–132.
- [63] Xinran Wang and Hongjie Dai. “Etching and narrowing of graphene from the edges”. In: *Nature chemistry* 2.8 (2010), pp. 661–665.
- [64] Rong Yang et al. “An anisotropic etching effect in the graphene basal plane”. In: *Advanced materials* 22.36 (2010), pp. 4014–4019.
- [65] Dechao Geng et al. “Fractal etching of graphene”. In: *Journal of the American Chemical Society* 135.17 (2013), pp. 6431–6434.
- [66] Dechao Geng et al. “Direct Top-Down Fabrication of Large-Area Graphene Arrays by an In Situ Etching Method”. In: *Advanced Materials* 27.28 (2015), pp. 4195–4199.
- [67] Yimin A Wu et al. “Large single crystals of graphene on melted copper using chemical vapor deposition”. In: *ACS nano* 6.6 (2012), pp. 5010–5017.
- [68] Mengqi Zeng et al. “Isotropic growth of graphene toward smoothing stitching”. In: *ACS nano* 10.7 (2016), pp. 7189–7196.
- [69] Mengqi Zeng et al. “Self-assembly of graphene single crystals with uniform size and orientation: the first 2D super-ordered structure”. In: *Journal of the American Chemical Society* 138.25 (2016), pp. 7812–7815.
- [70] Mengqi Zeng et al. “Self-assembly of metal oxide nanoparticles in liquid metal toward nucleation control for graphene single-crystal arrays”. In: *Chem* 4.3 (2018), pp. 626–636.
- [71] Xudong Xue et al. “Gas-flow-driven aligned growth of graphene on liquid copper”. In: *Chemistry of Materials* 31.4 (2019), pp. 1231–1236.

- [72] Juan Santiago Cingolani et al. “Interface between graphene and liquid Cu from molecular dynamics simulations”. In: *The Journal of Chemical Physics* 153.7 (2020), p. 074702.
- [73] Dominika Kuten et al. “Quasi-Monocrystalline Graphene Crystallization on Liquid Copper Matrix”. In: *Materials* 13.11 (2020), p. 2606.
- [74] Seong-Yong Cho et al. “Self-assembly and continuous growth of hexagonal graphene flakes on liquid Cu”. In: *Nanoscale* 7.30 (2015), pp. 12820–12827.
- [75] Peter S Pershan and Mark Schlossman. *Liquid surfaces and interfaces: synchrotron x-ray methods*. Cambridge University Press, 2012.
- [76] BM Ocko et al. “X-ray reflectivity study of thermal capillary waves on liquid surfaces”. In: *Physical review letters* 72.2 (1994), p. 242.
- [77] Lorenzo Botto et al. “Capillary interactions between anisotropic particles”. In: *Soft Matter* 8.39 (2012), pp. 9957–9971.
- [78] Roland Clift, John R Grace, and Martin E Weber. *Bubbles, drops, and particles*. Courier Corporation, 2005.
- [79] Krassimir D Danov et al. “Interactions between particles with an undulated contact line at a fluid interface: Capillary multipoles of arbitrary order”. In: *Journal of colloid and interface science* 287.1 (2005), pp. 121–134.
- [80] Krassimir D Danov and Peter A Kralchevsky. “Capillary forces between particles at a liquid interface: General theoretical approach and interactions between capillary multipoles”. In: *Advances in colloid and interface science* 154.1-2 (2010), pp. 91–103.
- [81] Jens Als-Nielsen and Des McMorrow. *Elements of modern X-ray physics*. John Wiley & Sons, 2011.
- [82] Carmelo Giacovazzo et al. *Fundamentals of crystallography*. Vol. 7. Oxford University Press Oxford, 2002.
- [83] Robert Feidenhans'l. “Surface structure determination by X-ray diffraction”. In: *Surface Science Reports* 10.3 (1989), pp. 105–188.
- [84] Elias Vlieg, JF van der Veen, and IK Robinson. “X-ray diffraction from surfaces and interfaces”. In: *Evolution of thin-film and surface microstructure*. 1991.

- [85] IK Robinson and DJ Tweet. “Surface X-ray diffraction”. In: *Reports on Progress in Physics* 55.5 (1992), p. 599.
- [86] Jean Daillant and Alain Gibaud. *X-ray and neutron reflectivity: principles and applications*. Vol. 770. Springer, 2008.
- [87] Philip Willmott. *An introduction to synchrotron radiation: techniques and applications*. John Wiley & Sons, 2019.
- [88] David Attwood and Anne Sakdinawat. *X-rays and extreme ultraviolet radiation: principles and applications*. Cambridge university press, 2017.
- [89] John R.. Ferraro, Kazuo Nakamoto, and Chris W.. Brown. *Introductory Raman Spectroscopy*. Academic press, 1994.
- [90] LM Malard et al. “Raman spectroscopy in graphene”. In: *Physics reports* 473.5-6 (2009), pp. 51–87.
- [91] Yassine El Mendili et al. “Raman Open Database: first interconnected Raman–X-ray diffraction open-access resource for material identification”. In: *Journal of Applied Crystallography* 52.3 (2019), pp. 618–625.
- [92] Jiang-Bin Wu et al. “Raman spectroscopy of graphene-based materials and its applications in related devices”. In: *Chemical Society Reviews* 47.5 (2018), pp. 1822–1873.
- [93] Ado Jorio et al. *Raman spectroscopy in graphene related systems*. John Wiley & Sons, 2011.
- [94] Daniel Casimir et al. “Raman Spectroscopy of Graphene, Graphite and Graphene Nanoplatelets”. In: *2D Materials*. IntechOpen, 2019.
- [95] Tomo-o Terasawa and Koichiro Saiki. “Radiation-mode optical microscopy on the growth of graphene”. In: *Nature communications* 6.1 (2015), pp. 1–6.
- [96] Kazuhiro Nagata, Toshihiro Nagane, and Masahiro Susa. “Measurement of normal spectral emissivity of liquid copper”. In: *ISIJ international* 37.4 (1997), pp. 399–403.
- [97] LA Falkovsky. “Optical properties of graphene”. In: *Journal of Physics: conference series*. Vol. 129. 1. IOP Publishing. 2008, p. 012004.

- [98] Takahiro Matsumoto et al. “Perfect blackbody radiation from a graphene nanostructure with application to high-temperature spectral emissivity measurements”. In: *Optics express* 21.25 (2013), pp. 30964–30974.
- [99] Edward P Randviir, Dale AC Brownson, and Craig E Banks. “A decade of graphene research: production, applications and outlook”. In: *Materials Today* 17.9 (2014), pp. 426–432.
- [100] Taeshik Yoon et al. “Direct measurement of adhesion energy of monolayer graphene as-grown on copper and its application to renewable transfer process”. In: *Nano letters* 12.3 (2012), pp. 1448–1452.
- [101] RA Munson. “Surface energies of liquid metal interfaces with carbon”. In: *Carbon* 5.5 (1967), pp. 471–474.
- [102] Gwan-Hyoung Lee et al. “High-strength chemical-vapor-deposited graphene and grain boundaries”. In: *science* 340.6136 (2013), pp. 1073–1076.
- [103] Mehdi Saedi et al. “Development of a reactor for the in situ monitoring of 2D materials growth on liquid metal catalysts, using synchrotron x-ray scattering, Raman spectroscopy, and optical microscopy”. In: *Review of Scientific Instruments* 91.1 (2020), p. 013907.
- [104] Pierre-Gilles De Gennes, Françoise Brochard-Wyart, and David Quéré. *Capillarity and wetting phenomena: drops, bubbles, pearls, waves*. Springer Science & Business Media, 2013.
- [105] Jianing Zhuang et al. “Morphology Evolution of Graphene during Chemical Vapor Deposition Growth: A Phase-Field Theory Simulation”. In: *The Journal of Physical Chemistry C* 123.15 (2019), pp. 9902–9908.
- [106] Thomas Michely and Joachim Krug. *Islands, mounds and atoms*. Vol. 42. Springer Science & Business Media, 2012.
- [107] Xiao Chen et al. “Chemical vapor deposition growth of 5 mm hexagonal single-crystal graphene from ethanol”. In: *Carbon* 94 (2015), pp. 810–815.
- [108] Xuesong Li et al. “Large-area graphene single crystals grown by low-pressure chemical vapor deposition of methane on copper”. In: *Journal of the American Chemical Society* 133.9 (2011), pp. 2816–2819.
- [109] Manuel G Velarde, Radyadour Kh Zeytounian, et al. *Interfacial phenomena and the Marangoni effect*. Springer, 2002.

- [110] Xiaoming Ge et al. “Effects of carbon-based impurities on graphene growth”. In: *Physical Chemistry Chemical Physics* 20.22 (2018), pp. 15419–15423.
- [111] Jun Li et al. “Impurity-induced formation of bilayered graphene on copper by chemical vapor deposition”. In: *Nano research* 9.9 (2016), pp. 2803–2810.
- [112] Jinyang Liu et al. “Controllable growth of the graphene from millimeter-sized monolayer to multilayer on Cu by chemical vapor deposition”. In: *Nanoscale research letters* 10.1 (2015), pp. 1–8.
- [113] Sibel Kasap et al. “Controlled growth of large area multilayer graphene on copper by chemical vapour deposition”. In: *Physical Chemistry Chemical Physics* 17.35 (2015), pp. 23081–23087.
- [114] Ping Wu et al. “Bilayer graphene growth via a penetration mechanism”. In: *The Journal of Physical Chemistry C* 118.12 (2014), pp. 6201–6206.
- [115] Shu Nie et al. “Growth from below: bilayer graphene on copper by chemical vapor deposition”. In: *New Journal of Physics* 14.9 (2012), p. 093028.
- [116] Haiming Zhao et al. “Growth and Raman spectra of single-crystal trilayer graphene with different stacking orientations”. In: *ACS nano* 8.10 (2014), pp. 10766–10773.
- [117] EH Kawamoto et al. “X-ray reflectivity study of the surface of liquid gallium”. In: *Physical Review B* 47.11 (1993), p. 6847.
- [118] MJ Regan et al. “Surface layering in liquid gallium: An X-ray reflectivity study”. In: *Physical review letters* 75.13 (1995), p. 2498.
- [119] MJ Regan et al. “X-ray reflectivity studies of liquid metal and alloy surfaces”. In: *Physical Review B* 55.23 (1997), p. 15874.
- [120] Françoise Bridou. “Curvature effect in grazing X-ray reflectometry”. In: *Journal de Physique III* 4.9 (1994), pp. 1513–1522.
- [121] Wuge H Briscoe et al. “Synchrotron XRR study of soft nanofilms at the mica–water interface”. In: *Soft Matter* 8.18 (2012), pp. 5055–5068.
- [122] Johannes Früh et al. “Reflectometry on curved interfaces”. In: *Physica B: Condensed Matter* 457 (2015), pp. 202–211.

- [123] Sven Festersen et al. “X-ray reflectivity from curved liquid interfaces”. In: *Journal of synchrotron radiation* 25.2 (2018), pp. 432–438.
- [124] Adamson AW Gast AP. *Physical chemistry of surface*. 1997.
- [125] Sander Roobol et al. “BINoculars: data reduction and analysis software for two-dimensional detectors in surface X-ray diffraction”. In: *Journal of applied crystallography* 48.4 (2015), pp. 1324–1329.
- [126] Jannik C Meyer et al. “The structure of suspended graphene sheets”. In: *Nature* 446.7131 (2007), pp. 60–63.
- [127] Jannik C Meyer et al. “On the roughness of single-and bi-layer graphene membranes”. In: *Solid State Communications* 143.1-2 (2007), pp. 101–109.
- [128] DA Kirilenko, AT Dideykin, and G Van Tendeloo. “Measuring the corrugation amplitude of suspended and supported graphene”. In: *Physical Review B* 84.23 (2011), p. 235417.
- [129] Annalisa Fasolino, JH Los, and Mikhail I Katsnelson. “Intrinsic ripples in graphene”. In: *Nature materials* 6.11 (2007), pp. 858–861.
- [130] Chun Hung Lui et al. “Ultraflat graphene”. In: *Nature* 462.7271 (2009), pp. 339–341.
- [131] Joachim Dahl Thomsen et al. “Suppression of intrinsic roughness in encapsulated graphene”. In: *Physical Review B* 96.1 (2017), p. 014101.
- [132] Aurélien F Stalder et al. “Low-bond axisymmetric drop shape analysis for surface tension and contact angle measurements of sessile drops”. In: *Colloids and Surfaces A: Physicochemical and Engineering Aspects* 364.1-3 (2010), pp. 72–81.
- [133] Joonsik Park et al. “Shape of a large drop on a rough hydrophobic surface”. In: *Physics of Fluids* 25.2 (2013), p. 022102.
- [134] Mathieu Doucet, RM Ferraz Leal, and Tanner C Hobson. “Web interface for reflectivity fitting”. In: *SoftwareX* 7 (2018), pp. 287–293.
- [135] JA Cahill and AD Kirshenbaum. “The density of liquid copper from its melting point (1356 K.) to 2500 K. and an estimate of its critical constants”. In: *The Journal of Physical Chemistry* 66.6 (1962), pp. 1080–1082.

- [136] Oleg Shpyrko et al. “X-ray study of the liquid potassium surface: Structure and capillary wave excitations”. In: *Physical Review B* 67.11 (2003), p. 115405.
- [137] AI Savvatimskiy. “Measurements of the melting point of graphite and the properties of liquid carbon (a review for 1963–2003)”. In: *Carbon* 43.6 (2005), pp. 1115–1142.
- [138] DDL Chung. “Review graphite”. In: *Journal of materials science* 37.8 (2002), pp. 1475–1489.
- [139] Linus Pauling. *The Nature of the Chemical Bond...* Vol. 260. Cornell university press Ithaca, NY, 1960.
- [140] Lili Fan et al. “Step driven competitive epitaxial and self-limited growth of graphene on copper surface”. In: *AIP Advances* 1.3 (2011), p. 032145.
- [141] Sultan Akhtar et al. “Few-Layers Graphene Film and Copper Surface Morphology for Improved Corrosion Protection of Copper”. In: *Journal of Materials Engineering and Performance* 28.9 (2019), pp. 5541–5550.
- [142] Robert M Jacobberger and Michael S Arnold. “Graphene growth dynamics on epitaxial copper thin films”. In: *Chemistry of Materials* 25.6 (2013), pp. 871–877.
- [143] Wei Gao and Rui Huang. “Effect of surface roughness on adhesion of graphene membranes”. In: *Journal of Physics D: Applied Physics* 44.45 (2011), p. 452001.
- [144] Liting Xiong and Yuanwen Gao. “Surface roughness and size effects on the morphology of graphene on a substrate”. In: *Physica E: Low-dimensional Systems and Nanostructures* 54 (2013), pp. 78–85.
- [145] Thomas Olsen et al. “Dispersive and covalent interactions between graphene and metal surfaces from the random phase approximation”. In: *Physical review letters* 107.15 (2011), p. 156401.
- [146] Petr Khomyakov et al. “Doping graphene with metal contacts”. In: (2008).
- [147] Mie Andersen, Liv Hornekær, and Bjørk Hammer. “Graphene on metal surfaces and its hydrogen adsorption: A meta-GGA functional study”. In: *Physical Review B* 86.8 (2012), p. 085405.

- [148] X Li et al. “Klimeš J. cv; Michaelides A”. In: *Influence of water on the electronic structure of metal-supported graphene: Insights from van der Waals density functional theory*. *Phys. Rev. B* 85.08542510.1103 (2012).
- [149] Zhiping Xu and Markus J Buehler. “Interface structure and mechanics between graphene and metal substrates: a first-principles study”. In: *Journal of Physics: Condensed Matter* 22.48 (2010), p. 485301.
- [150] Yuki Fukaya et al. “Spacing between graphene and metal substrates studied with total-reflection high-energy positron diffraction”. In: *Carbon* 103 (2016), pp. 1–4.